Challenge Journal of
STRUCTURAL MECHANICS

Vol.7 No.1 (2021)

Mindlin's theory buckling compressive strength dynamic analysis dynamic response earthquake finite element analysis finite element method mechanical properties operational modal analysis optimization pushover analysis railways reinforced concrete seismic analysis seismic design seismic isolation shallow foundations steel silo teaching-learning based optimization th[illegible]iate

TULPAR ACADEMIC PUBLISHING

ISSN 2149-8024

Challenge Journal of Structural Mechanics

E-mail: *cjsmec@challengejournal.com*

Web page: *cjsmec.challengejournal.com*

TULPAR Academic Publishing
www.tulparpublishing.com

Challenge Journal of Structural Mechanics

CONTENTS

Research Articles

TULPAR ACADEMIC PUBLISHING

Challenge Journal of Structural Mechanics

Research Article

Determination of the exact mode frequencies of multi-storey structures by state-space method and a comparison with mode superposition method

Ahmad Yamin Rasa [a,*], Mehmet Hamit Özyazıcıoğlu [a]

[a] *Department of Civil Engineering, Atatürk University, 25240 Erzurum, Turkey*

ABSTRACT

In this paper, a comparative research obtaining the time-consuming exact solution and approximate solution of linearly damped linear frame buildings has been carried out. State-space method and mode superposition method are respectively utilized to analyze the exact and approximate vibration solution of frame buildings. In mode superposition method, the proportional damping matrix of frame buildings has been constructed in two different schemes, such as modal combination of mass with stiffness matrices (Rayleigh) and disregarding the off-diagonal elements of non-classical damping (DOEA) matrix. Meanwhile, the damping matrix in state-space method is non-proportional and constructs in exact circumstance. By imposing different initial conditions on the system, it has been proved that the transient vibration is mostly greater than the steady-state vibration. These observations have individually been investigated to render the approximate response as close as possible to the exact response. The findings of current research indicate that the most suitable parameter which brings closer the approximate response to the exact response is DOEA approach. In addition, a MATLAB code, which solves the equation of exact and approximate method, is generated in this research.

ARTICLE INFO

Article history:
Received 13 July 2020
Revised 28 September 2020
Accepted 23 October 2020

Keywords:
Structural dynamics
State-space method
Mode superposition method
Transient vibration
Mode frequency

1. Introduction

In structural dynamics, mode superposition method is a general approach, which can analyze transient and steady-state response of structures under different dynamic loads. Modal frequencies and modal vectors of structure are generally calculated in un-damped situation. Based on the idea of Borino and Muscolin (1986), exact frequencies (damped frequencies) of structures will not differ much from un-damped frequencies. This idea is clearly explained with examples in this article. In this method, damping matrix could be generated either by linear combination of mass and stiffness matrix (proportional damping) or by neglecting the non-diagonal elements of non-proportional damping matrix, Felszeghy (1986), Wilson and Penzien (1972). This approximate method is generally implemented in three stages; 1) evaluating the modal frequencies and modal vectors of un-damped system, 2) creating the proportional damping matrix of the system and 3) combining the modal responses. The maximum responses (displacement, velocity, acceleration or internal forces) can be calculated either by Square Root of Sum of the Squares (SRSS) method or Complete Quadratic Combination (CQC) method. These methods are exist in Sinha and Igusa (1992), Wilson, Kiureghian and Bayo (1981) and Zhou, Yu and Liang (2004) articles.

In state-space method, which gives the exact response of dynamic systems, damping matrix constructs in exact situation and is always non-proportional. Mode frequencies and mod vectors of the system are always in complex conjugate form; and modal frequencies are damped frequencies, not same as mod superposition method. It would be better to predict the modal damping factors of

* *Corresponding author*. E-mail address: ahmadyamin.rasa19@ogr.atauni.edu.tr (A. Y. Rasa)
ISSN: 2149-8024 / DOI: https://doi.org/10.20528/cjsmec.2021.01.001

each mode form damped frequencies, Veletsos and Ventura (1986).

In this research, the difference between exact and approximate response of a vibrational structure has been investigated in detail. The most suitable type of proportional damping matrix, which gives the nearest response to the exact response, is determined. Proportional damping matrix is constructed in three types; (a) combining first and second modes of vibration (MSM-a), (b) combining first and last modes of vibration (MSM-b) and (c) combining first and third modes of vibration in five story frame building (MSM-c). Modal damping ratios of frame buildings are derived from exact damped frequencies of them. In practical analysis, damping ratio of the whole system is approximately given such 5% ratio (MSM-5%); the result of this condition is investigated in detail. One another type of damping matrix, which is simplified by disregarding the off-diagonal elements approach (DOEA), is also observed in this research paper. Harmonic forces are applied on different floors of three and five storey frame buildings. Dynamic responses of frame buildings are comparatively displayed using figures and tables. Maximum responses are calculated by square root of sum of the squares (SRSS) method, Sinha, Igusa (1992). Caughey damping is not utilized in this research which are based on Caughey (1960) and Caughey and O'Kelly (1965) articles.

2. Methods

2.1. Analytical formulation of mode superposition method

Consider a classical damped linear structure subjected to harmonic force $f(t)$. The equation of motion for this system, which structural displacements are relative to dynamic load, may be written as;

$$\mathbf{m}\underline{\ddot{u}} + \boldsymbol{c}\underline{\dot{u}} + \boldsymbol{k}\underline{u} = \underline{f}(t) \tag{1}$$

where, **m**, **c** and **k** respectively denotes mass matrix, damping matrix and stiffness matrix of structure-damper system. And $\underline{\ddot{u}}, \underline{\dot{u}}, \underline{u}, \underline{f}(t)$ respectively expresses acceleration vector, velocity vector, relative displacement vector and force vector. Each modal parameter of frame building, which is un-damped natural frequency ω_n and mode vibration $\underline{\emptyset}_n$, can be calculated by eigen-equation of,

$$-\omega_n^2 \boldsymbol{m}\underline{\emptyset}_n + \boldsymbol{k}\underline{\emptyset}_n = 0 \tag{2}$$

If it is assumed that the matrix of orthonormal modes $\emptyset$ associated with the un-damped system can be used as a transformation matrix to uncouple Eqs. (1), then a set of generalized co-ordinates q may be defined like $u(t) = \emptyset q(t)$. Therefore, generalized forces $F_n(t)$, masses M_n, stiffness constants K_n, damping constants C_n could be defined using transformation matrix $\emptyset$. Thus, the resulting equations are uncoupled if the damping matrix **c** is a linear combination of inertia matrix **m** and/or stiffness matrix **k.** Therefore, Eqs. (1) becomes like,

$$\boldsymbol{M}\underline{\ddot{q}} + \boldsymbol{C}\underline{\dot{q}} + \boldsymbol{K}\underline{q} = \underline{F}(t) \tag{3}$$

This equation consists of n uncoupled equations which may be solved by standard procedures. Thus, nth uncoupled equation of motion can written like,

$$M_n\ddot{q}_n + C_n\dot{q}_n + K_n q_n = F_n(t) \tag{4}$$

In which q_n is the generalized coordinate of the system. Modal damping ratio ζ_n which is belongs to the n'th mode can be calculated dividing Eq. (4) by M_n,

$$\ddot{q}_n + 2\zeta_n \omega_n \dot{q}_n + \omega^2{}_n q_n = \frac{F_n(t)}{M_n} \tag{5}$$

Thus, modal damping ratio of any mode can be calculated by equation;

$$\zeta_n = \frac{C_n}{2M_n\omega_n} \tag{6}$$

Total solution of Eq. (5) may be written as vector sum of two components (free vibration + forced vibration),

$$q_n(t) = e^{-\zeta_n\omega_n t}\left[q_n(0)cos(\omega d_n t) + \frac{\dot{q}(0)+\zeta_n\omega_n q(0)}{\omega d_n} sin(\omega d_n t)\right] + \frac{1}{M_n\omega d_n}\int_0^t F_n(\tau)\, e^{-\zeta_n\omega_n(t-\tau)} sin[\omega d_n\,(t-\tau)]d\,\tau \tag{7}$$

At the right hand side of Eq. (7), the first term is called free vibration (homogeneous solution) part and second term is called forced vibration (non-homogeneous) part. More details about free vibration of structural elements could be found in Avcar (2104) and Civalek and Avcar (2020) articles. In this equation $q_n(0)$, $\dot{q}_n(0)$ and $\omega d_n = \omega_n\sqrt{1-\zeta_n^2}$ are initial displacement, initial velocity and damped frequency of the nth mode, respectively. Thus, displacement response of the nth mode may be written as,

$$\underline{u}_n(t) = \underline{\emptyset}_n q_n(t) \tag{8}$$

Displacement responses may be calculated combining all vibrating modes,

$$\underline{u}(t) = \sum_{n=1}^{N} \underline{\emptyset}_n q_n(t) \tag{9}$$

2.2. Analytical formulation of state-space method

In this method Eq. (1) which is a second-order differential equation has been reduced to a first-order differential equation consisting 2xN equations, based on Veletsos and Ventura (1986) and Villaverde (2008) articles. Substituting $\underline{\ddot{u}}$ to $\underline{\dot{z}}$ and $\underline{\dot{u}}$ to $\underline{z}$ then put these relations to Eq. (1),

$$\underline{\dot{u}} = \underline{z}$$

$$\boldsymbol{m}\underline{\dot{z}} + \boldsymbol{c}\underline{z} + \boldsymbol{k}\underline{u} = \underline{f}(t) \tag{10}$$

Then, new variables (displacement and velocity vectors) can be summed into vector $\underline{Z}$,

$$\underline{Z} = \begin{bmatrix} \underline{u} \\ \underline{z} \end{bmatrix}_{2n\times 1} \tag{11}$$

After some mathematical operations on Eq. (10), Eq. (12) is obtained as,

$$\begin{bmatrix} \underline{\dot{u}} \\ \underline{\dot{z}} \end{bmatrix}_{2n\times 1} = \begin{bmatrix} \mathbf{0}_{n\times n} & \boldsymbol{I}_{n\times n} \\ -\boldsymbol{m}^{-1}\boldsymbol{k} & -\boldsymbol{m}^{-1}\boldsymbol{c} \end{bmatrix}_{2n\times 2n} \begin{bmatrix} \underline{u} \\ \underline{z} \end{bmatrix}_{2n\times 1} + \begin{bmatrix} \underline{0} \\ \boldsymbol{m}^{-1}\underline{f}(t) \end{bmatrix}_{2n\times 1} \tag{12}$$

Reduced form of Eq. (1), which is a first order differential equation, can be represented as a general form of,

$$\dot{\underline{Z}}(t) = \boldsymbol{A}\underline{Z} + \underline{P}(t) \tag{13}$$

In this equation, constant matrix **A**, dynamic force vector $\underline{P}(t)$ and initial condition vector $\underline{Z}(0)$ can be expressed as,

$$\boldsymbol{A} = \begin{bmatrix} \mathbf{0}_{n\times n} & \boldsymbol{I}_{n\times n} \\ -\boldsymbol{m}^{-1}\boldsymbol{k} & -\boldsymbol{m}^{-1}\boldsymbol{c} \end{bmatrix}_{2n\times 2n} \tag{14}$$

$$\underline{P}(t) = \begin{bmatrix} \underline{0} \\ \boldsymbol{m}^{-1}\underline{f}(t) \end{bmatrix}_{2n\times 1} \tag{15}$$

$$\underline{Z}(0) = \begin{bmatrix} \underline{u}(0)_{n\times 1} \\ \underline{\dot{u}}(0) \end{bmatrix} \tag{16}$$

The analytical solution of Eq. (13), which has homogeneous part and non-homogeneous part, is the same solution of Eq. (5).

2.2.1. Free vibration response

The dynamic force vector in Eq. (13) will be zero ($\underline{P}(t) = 0$) if the system vibrates freely. Thus, homogeneous form of Eq. (13) can be expressed as,

$$\dot{\underline{Z}}(t) = \boldsymbol{A}\underline{Z} \tag{17}$$

Solution of this equation may be written as,

$$\underline{Z}_h = \boldsymbol{e}^{\boldsymbol{A}t}\underline{c} \tag{18}$$

In this solution vector $\underline{c}$ can be determined by utilizing initial condition, so;

$$\underline{Z}(0) = \underline{c} \tag{19}$$

$$\underline{Z}_h = \boldsymbol{e}^{\boldsymbol{A}t}\underline{Z}(0) \tag{20}$$

Eq. (20) is the free vibration response of state-space Eq. (13).

2.2.2. Forced vibration response (general solution)

General solution of Eq. (13) can be found using variation of parameters. If homogeneous solution of Eq. (13) assumes as *K*, then the non-homogeneous solution of them can be written as;

$$\underline{Z}_p = \underline{V} \times \underline{K} \tag{21}$$

Parameter $\underline{V}$ can be calculated putting Eq. (21) in to Eq. (13). Therefore, the general solution of state-space Eq. (13) can be obtained like,

$$\underline{Z}(t) = \boldsymbol{e}^{\boldsymbol{A}t}\underline{Z}(0) + \boldsymbol{e}^{\boldsymbol{A}t}\int_0^t \boldsymbol{e}^{-\boldsymbol{A}\tau}\underline{Z}(0)\underline{P}(\tau)d\tau \tag{22}$$

or;

$$\underline{Z}(t) = \boldsymbol{e}^{\boldsymbol{A}t}\underline{Z}(0)\int_0^t \boldsymbol{e}^{\boldsymbol{A}(t-\tau)}\underline{Z}(0)\underline{P}(\tau)d\tau \tag{23}$$

In Eqs. (22) and (23), the first term at the right hand side denotes free vibration while the second term denotes forced vibration. Algebraic solution of Eq. (22) or (23) depends on the solution of $\boldsymbol{e}^{\boldsymbol{A}t}$. Therefore, utilizing the concepts of linear algebra, eigenvalues and eigenvectors of square matrix $\boldsymbol{A}$ can be calculated using eigen-equation bellow,

$$(\boldsymbol{A} - v_n\boldsymbol{I})\underline{x}_n = \underline{0}, \quad n = 1,2,3 \dots \tag{24}$$

In this equation, $\boldsymbol{I}, \underline{v}_n$ and $\underline{x}_n$ are respectively unite square matrix, *n*th complex eigenvalue and eigenvector of squared matrix $\boldsymbol{A}$. This equation gives a set of $2 \times N$ eigenvalues v_n and eigenvectors $\underline{x}_n$, N is the number of storeys. These eigen-solutions always exist like complex conjugate form bellow, Veletsos and Ventura (1986) and Villaverde (2008);

$$\left.\begin{matrix} v_n \\ \overline{v}_n \end{matrix}\right\} = -e_n \pm is_n, \quad n = 1,2,3 \dots \tag{25}$$

$$\left.\begin{matrix} \underline{x}_n \\ \overline{\underline{x}}_n \end{matrix}\right\} = -\underline{\varphi}_n \pm i\underline{\alpha}_n, \quad n = 1,2,3 \dots \tag{26}$$

In the relations above, complex conjugate eigenvalues and eigenvectors, which respectively represent frequencies and modes of vibration, has been marked a dash on it. Real part of complex eigenvalue e_n representing damping mechanism of *n*th mode must be negative and, complex part of eigenvalue, which represents damped frequency of *n*th mode, can give damping factor of that mode. Thus, damping ratio for each mode of vibration can be calculated by equation,

$$\zeta_n = \frac{e_n}{\sqrt{e_n^2 + s_n^2}}, \qquad n = 1,2,3 \dots \tag{27}$$

Based on Veletsos and Ventura (1986) article, there will be a unique damping ratio for any mode of vibration if Eq. (23) is utilized.

3. Results and Discussion

In this section, three and five storey frame buildings, which are taken from Rasa (2017), are selected as examples. The methods described above have been utilized in these examples and, the total responses are obtained by summation of free and forced vibration.

3.1. Example 1

For simplicity, only second floor responses are selected to compare the results here.

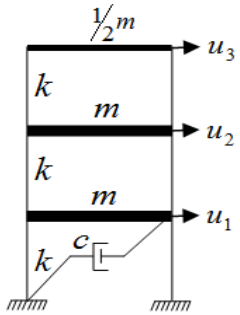

Fig. 1. Three storey structure with a damper at the bottom storey.

Initial displacement vector, initial velocity vector, dynamic force, inertia constant, stiffness constant and damping constant of the frame building (Fig. 1) has respectively been given as $\underline{u}(0) = \{0, 0, 0.1\}^T$m, $\underline{\dot{u}}(0) = \{0, 0.5, 0\}^T$m/sec, $f_1(t) = 0.1\sin(\pi t/0.3)$ kN, m=1 kg, k=1 kN/m and c=0.2 kNs/m. Therefore, mass matrix, damping matrix, stiffness matrix-and force vector, initial displacement vector and initial velocity vector of frame building can respectively be written as bellow;

$$\boldsymbol{m} = \begin{bmatrix} 1 & 0 & 0 \\ 0 & 1 & 0 \\ 0 & 0 & 0.5 \end{bmatrix} \quad \boldsymbol{c} = \begin{bmatrix} 0.2 & 0 & 0 \\ 0 & 0 & 0 \\ 0 & 0 & 0 \end{bmatrix}$$

$$\boldsymbol{k} = \begin{bmatrix} 2 & -1 & 0 \\ -1 & 2 & -1 \\ 0 & -1 & 1 \end{bmatrix} \quad \underline{f}(t) = \begin{bmatrix} f_1 \\ 0 \\ 0 \end{bmatrix}$$

$$\underline{u}(0) = \begin{bmatrix} 0 \\ 0 \\ 0.1 \end{bmatrix} \quad \underline{\dot{u}}(0) = \begin{bmatrix} 0 \\ 0.5 \\ 0 \end{bmatrix}$$

In Tables 1 and 2, complex mode frequencies and exact modal damping factors of frame building are respectively calculated by Eqs. (24) and (27). Creating proportional damping matrix of frame building needs a damping factor ζ, which is given approximately 5% and 0.033%. Taking the average of exact modal damping factors from Table 1 gives damping factor (0.033%).

Table 1. Exact mode frequencies and modal damping ratios of the frame building.

	1. Mode	2. Mode	3. Mode
ω_n	$-0.0163 \pm i1.9290$	$-0.0671 \pm i1.4126$	$-0.0167 \pm i0.5181$
ζ_n	0.0084	0.0474	0.0322

Table 2. Complex mode vectors of the frame building.

0.0340 – 0.1568i	0.0340 + 0.1568i	0.0195 + 0.4105i	0.0195 - 0.4105i	-0.3135 + 0.0188i	-0.3135 - 0.0188i
-0.0079 + 0.2813i	-0.0079 - 0.2813i	-0.0383 + 0.0000i	-0.0383 - 0.0000i	-0.5436 + 0.0054i	-0.5436 - 0.0054i
-0.0028 - 0.3269i	-0.0028 + 0.3269i	-0.0198 - 0.4032i	-0.0198 + 0.4032i	-0.6277 + 0.0000i	-0.6277 + 0.0000i
0.3019 + 0.0680i	0.3019 - 0.0680i	-0.5812 + 0.0000i	-0.5812 + 0.0000i	-0.0045 - 0.1628i	-0.0045 + 0.1628i
-0.5426 - 0.0198i	-0.5426 + 0.0198i	0.0025 - 0.0541i	0.0025 + 0.0541i	0.0063 - 0.2817i	0.0063 + 0.2817i
0.6306 + 0.0000i	0.6306 + 0.0000i	0.5709 - 0.0010i	0.5709 + 0.0010i	0.0105 - 0.3252i	0.0105 + 0.3252i

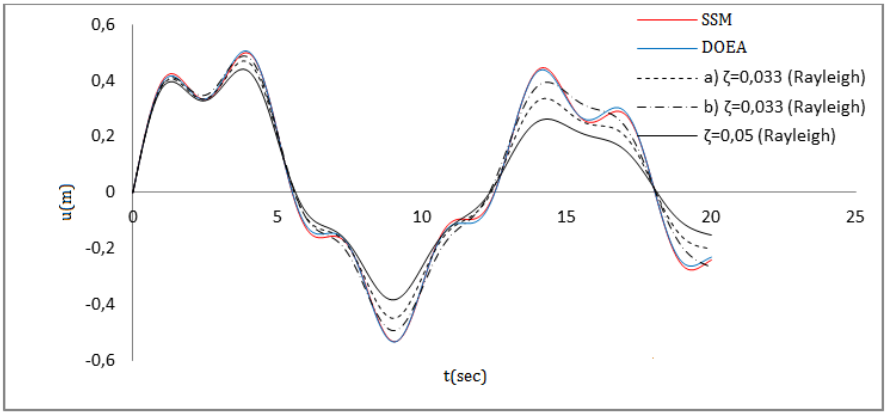

Fig. 2. Displacement response of second floor: (a) Rayleigh damping is created using first and second modes; (b) Rayleigh damping is created using first and third modes of vibration.

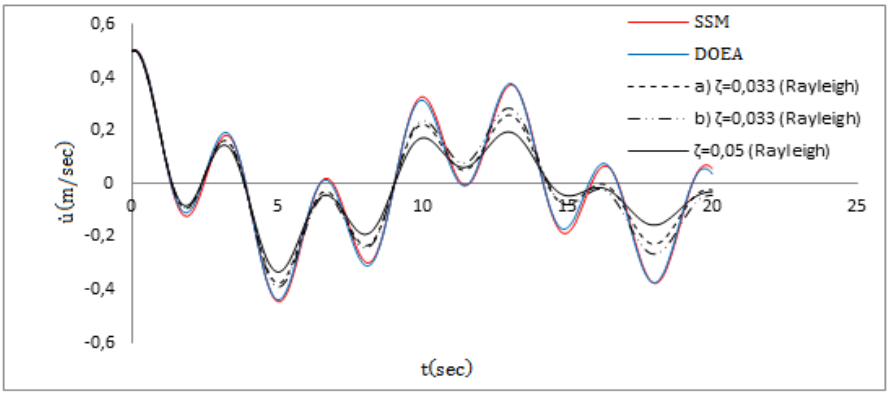

Fig. 3. Velocity response of second floor: (a) Rayleigh damping is created using first and second modes; (b) Rayleigh damping is created using first and third modes of vibration.

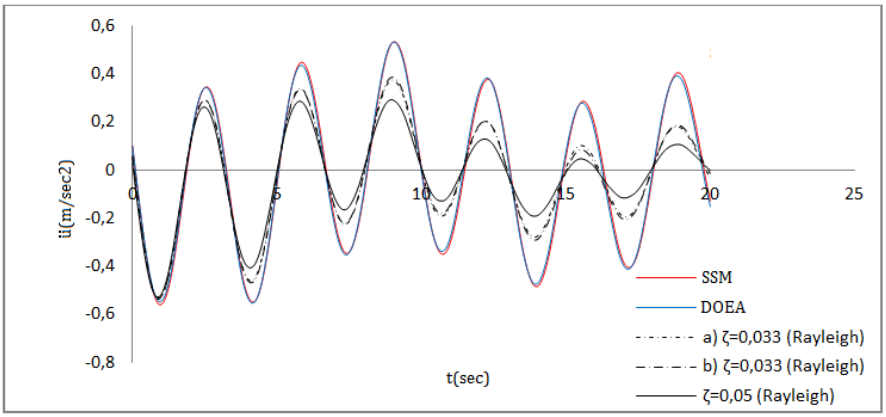

Fig. 4. Acceleration response of second floor:(a) Rayleigh damping is created using first and second modes; (b) Rayleigh damping is created using first and third modes of vibration.

According to Table 3, it is proved that DOEA method has a good agreement with SSM method. Among four approximate methods, the closest response to exact response is given by DOEA method. After DOEA method the closest response, which is in second order, is given by MSM-b method. Results of other two methods (MSM-a and MSM-5%) are not in good agreement with exact method. The maximum displacement response calculated by SSM and DOEA methods occur in 9.045 seconds, while by the other methods (MSM-a, MSM-b and MSM-5%) occur in 3.819 seconds. The displacement response in 3.819 seconds of exact method is seen to be 0.4983 meters.

Table 3. Maximum responses of the second floor.

Method	Time (sec)	Max. Dis. (m)	Time (sec)	Max. Vel. (m/sec)	Time (sec)	Max. Acce. (m/sec²)
SSM	9.045 (3.819)	0.5332 (0.4983)	0	0.5	1.005 (4.121)	0.5587 (0.5473)
DOEA	9.045	0.5341	0	0.5	4.121	0.5522
MSM-a	3.819	0.4710	0	0.5	0.9045	0.5367
MSM-b	3.819	0.4887	0	0.5	0.9045	0.5320
MSM-5%	3.819	0.4413	0	0.5	0.9045	0.5280

In second mode of vibration, the exact un-damped natural frequency and the exact modal damping ratio of the frame building, as seen in Table 4 are respectively 1.4141 and 0.0474. In contrast, the results 1.4142 and 0.0471 are respectively very close to that of the exact method. Thus, the closest response to the exact response was calculated by DOEA method. Modal damping ratios calculated by other methods (MSM-a, MSM-b and MSM-5%) are not in good agreement with SSM method. As seen in Figs. 1, 2 and 3 there is a very good agreement between time history responses of SSM method and DOEA method.

As seen in Table 5, the velocity and acceleration responses of DOEA method are very close to that of the exact method, only the displacement response of MSM-b method is very close to that of exact method. It is also

considered that the results of MSM-5% method has the most deviation among three methods (DOEA, MSM-a, MSM-b) with the rate of 11.14%. It can be concluded that DOEA method has very good agreement with SSM method at all.

Table 4. Modal damping ratios and mode frequencies of the second mode.

Method	ζ_2	ω_2	ωd_2
SSM	0.0474	1.4141	1.4126
DOEA	0.0471	1.4142	1.4126
MSM-a	0.0330	1.4142	1.4134
MSM-b	0.0286	1.4142	1.4136
MSM-5%	0.0500	1.4142	1.4124

Table 5. Maximum responses of the frame building.

Method	Max. Dis. (m)	Max. Vel. (m/sec)	Max. Accel. (m/sec²)
SSM	0.7486	0.5095	0.9638
DOEA	0.7495	0.5095	0.9624
MSM-a	0.7249	0.5081	0.8944
MSM-b	0.7487	0.5086	0.8936
MSM-5%	0.6975	0.5071	0.8564

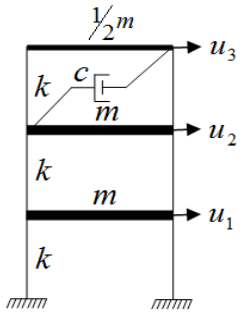

Fig.5. Three storey structure with a damper at the bottom storey.

$$\boldsymbol{c} = \begin{bmatrix} 0 & 0 & 0 \\ 0 & 0.2 & -0.2 \\ 0 & -0.2 & 0.2 \end{bmatrix}$$

Creating proportional damping matrix of frame building needs a damping factor ζ, which is given approximately 5% and 0.056%. Taking the average of exact modal damping factors from Table 6 gives damping factor (0.056%).

Table 6. Exact mode frequencies and modal damping ratios of the frame building.

	1. Mode	2. Mode	3. Mode
ω_n	$-0.2374 \pm i1.8824$	$-0.0614 \pm i1.4383$	$-0.0012 \pm i0.5178$
ζ_n	0.1251	0.0427	0.0023

3.2. Example 2

The following example, which has the same initial conditions, dynamic force, uniform storey stiffness, floor masses given in the Example 1, refers to three-storey structure shown in Fig. 5. The viscous damper has been moved on the top floor. All steps of analysis in previous example have been repeated and only responses of the second floor are discussed here.

According to Table 7, DOEA and MSM-b methods give the closest results to SSM method. It is proved again, that DOEA method is in the first order. While the maximum displacement response calculated by SSM and DOEA methods occurs in approximately 9 seconds, it occurs in 3.819 seconds with other approximate methods. The displacement response at 3.819 seconds of SSM method is seen to be 0.4819 m

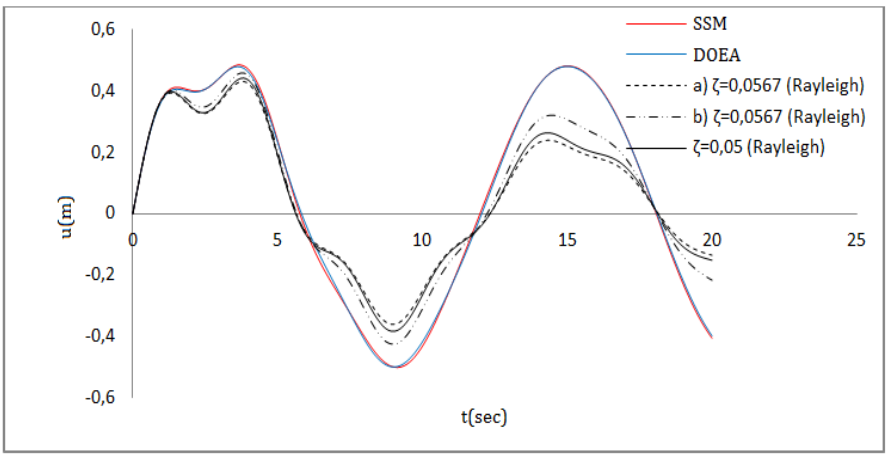

Fig. 6. Displacement response of second floor: (a) Rayleigh damping is created using first and second modes; (b) Rayleigh damping is created using first and third modes of vibration.

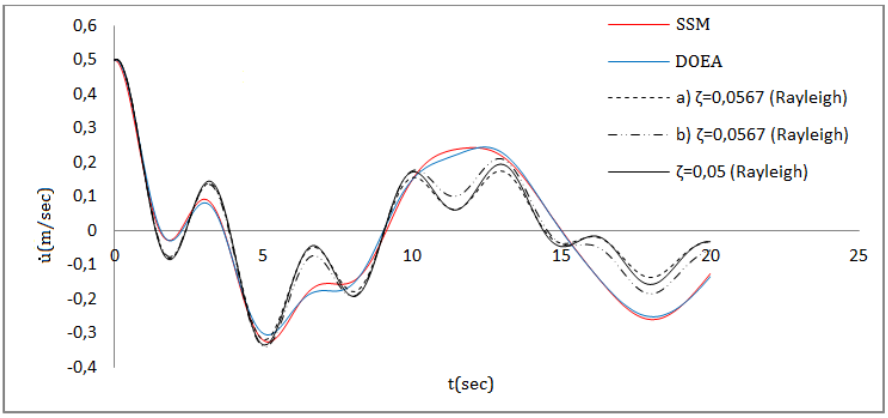

Fig. 7. Velocity response of second floor: (a) Rayleigh damping is created using first and second modes; (b) Rayleigh damping is created using first and third modes of vibration.

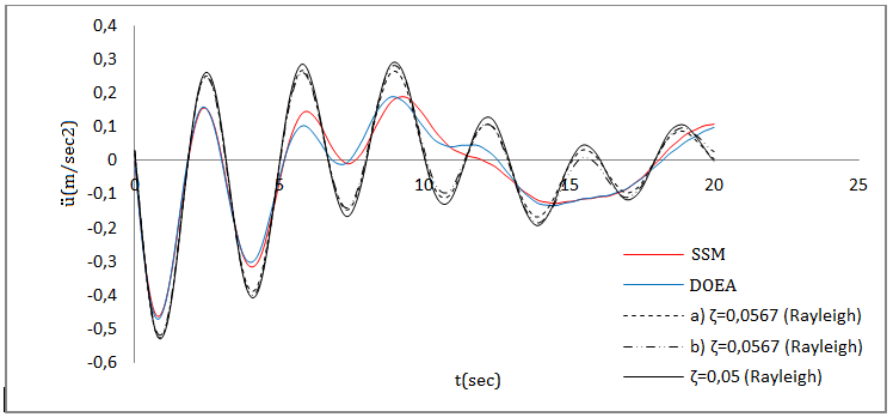

Fig. 8. Acceleration response of second floor: (a) Rayleigh damping is created using first and second modes; (b) Rayleigh damping is created using first and third modes of vibration.

Table 7. Maximum responses of the second floor.

Method	Time (sec)	Max. Dis. (m)	Time (sec)	Max. Vel. (m/sec)	Time (sec)	Max. Acce. (m/sec²)
SSM	9.146 (3.819)	0.5011 (0.4819)	0	0.5	0.804	0.4623
DOEA	9.045	0.4993	0	0.5	0.804	0.4703
MSM-a	3.819	0.4303	0	0.5	0.9045	0.5246
MSM-b	3.819	0.4581	0	0.5	0.9045	0.5169
MSM-5%	3.819	0.4413	0	0.5	0.804	0.5244

As seen in Table 8, the exact modal damping ratio and natural frequency of the second mode are respectively 0.0427 and 1.4396. Among four approximate methods, the closest results to the exact solution, which are calculated by DOEA method, were found to be 0.0471 and 1.4142. As seen in the time history response of second floor, the closest response has been given by the DOEA method.

From Table 9, it is seen that the closest result to the exact solution is obtained by the DOEA and MSM-b method. Therefore, among these approximate methods the maximum deviation was found to be 16.24% by MSM-5%. Natural frequencies and modal damping ratios of the three-storey frame building with dampers at different floors were calculated and compared with each other. Being small natural frequencies, the frame building with a damper at the first floor has been tested to be more rigid than that with a damper at the top floor. Therefore, it would be better to put the damper at the first floor. Furthermore, when replacing the damper of the frame building from bottom to top floor, the damping matrix and natural frequencies of them are respectively changed by SSM and DOEA methods, but by other three methods no change has been seen on natural frequencies and damping matrix.

Table 8. Modal damping ratios and mode frequencies of the second mode.

Method	ζ_2	ω_2	ωd_2
SSM	0.0427	1.4396	1.4383
DOEA	0.0471	1.4142	1.4126
MSM-a	0.0567	1.4142	1.4119
MSM-b	0.0491	1.4142	1.4125
MSM-5%	0.0500	1.4142	1.4124

Table 9. Maximum responses of the frame building.

Method	Max. Dis. (m)	Max. Vel. (m/sec)	Max. Accel. (m/sec²)
SSM	0.7823	0.5093	0.7367
DOEA	0.7826	0.5091	0.7347
MSM-a	0.6871	0.5067	0.8424
MSM-b	0.7254	0.5068	0.8408
MSM-5%	0.6975	0.5071	0.8564

3.3. Example 3

The following example refers to a five-storey structure, which has non-uniform storey stiffness, floor masses m_1 and m_2, and two viscous dampers in the first and second storey of the structure, shown in Fig. 9. Results are discussed in comparative tables. The comparative vibrational graphs of each storey exist in Rasa (2017).

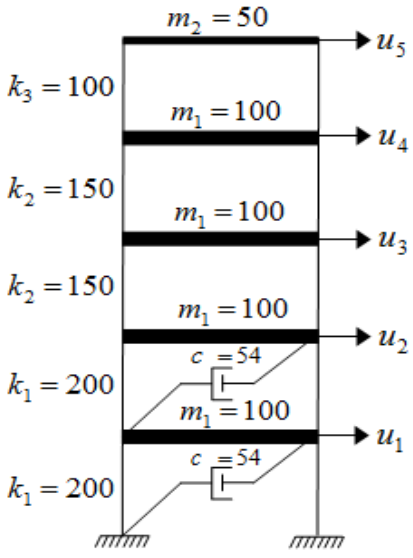

Fig. 9. Five-storey structure with two dampers at the first and second floors.

$$\boldsymbol{m} = \begin{bmatrix} 100 & 0 & 0 & 0 & 0 \\ 0 & 100 & 0 & 0 & 0 \\ 0 & 0 & 100 & 0 & 0 \\ 0 & 0 & 0 & 100 & 0 \\ 0 & 0 & 0 & 0 & 50 \end{bmatrix}$$

$$\boldsymbol{k} = \begin{bmatrix} 400 & -200 & 0 & 0 & 0 \\ -200 & 350 & -150 & 0 & 0 \\ 0 & -150 & 300 & -150 & 0 \\ 0 & 0 & -150 & 250 & -100 \\ 0 & 0 & 0 & -100 & 100 \end{bmatrix}$$

$$\boldsymbol{c} = \begin{bmatrix} 108 & -54 & 0 & 0 & 0 \\ -54 & 54 & 0 & 0 & 0 \\ 0 & 0 & 0 & 0 & 0 \\ 0 & 0 & 0 & 0 & 0 \\ 0 & 0 & 0 & 0 & 0 \end{bmatrix}$$

$$\underline{\boldsymbol{f}}(\boldsymbol{t}) = \begin{bmatrix} 10\sin\left(\frac{3}{2}t\right) \\ 0 \\ 0 \\ 0 \\ 0 \end{bmatrix} \quad \underline{\boldsymbol{u}}(\boldsymbol{0}) = \begin{bmatrix} 0 \\ 0 \\ 0 \\ 0 \\ 0.1 \end{bmatrix} \quad \underline{\dot{\boldsymbol{u}}}(\boldsymbol{0}) = \begin{bmatrix} 0.2 \\ 0 \\ 0 \\ 0 \\ 0 \end{bmatrix}$$

Mass matrix, damping matrix, and stiffness matrix of the structure, dynamic force and initial condition vector are given above. Comparative tables discussing the exact and approximate modal damping factors, damped frequencies and maximum responses of the system are given in detail. Creating proportional damping matrix of frame building needs a damping factor ζ, which is given approximately 5% and 0.081%. Taking the average of exact modal damping factors from Table 11 gives damping factor (0.081%).

Table 10. Exact and approximate mode frequencies of the building.

SSM	v_n	DOEA and MSM	ω_n
v_1	$-0.6391 \pm i2.2924$	ω_1	2.4915
v_2	$-0.0437 \pm i2.1911$	ω_2	2.1246
v_3	$-0.0528 \pm i1.6933$	ω_3	1.6756
v_4	$-0.0594 \pm i1.1384$	ω_4	1.1374
v_5	$-0.0149 \pm i0.4210$	ω_5	0.4205

As seen in Table 11, the closest result to the exact modal damping ratio of the building is given by DOEA method. The modal damping ratios obtained by other four approximate methods are smaller than that of exact method. Furthermore, a big difference between modal damping ratios has been seen in the fourth and fifth modes of vibration. In Table 12, the maximum responses calculated by DOEA method are very close to that of exact method as well. The most deviation among five approximate methods, which is calculated 38.51%, occurs in the MSM-a method.

Table 11. Exact and approximate modal damping ratios of the building.

Method	ζ_1	ζ_2	ζ_3	ζ_4	ζ_5
SSM	0.2686	0.0200	0.0312	0.0521	0.0353
DOEA	0.2133	0.0644	0.0403	0.0523	0.0354
MSM-a	0.0810	0.0810	0.0848	0.1016	0.2283
MSM-b	0.0810	0.0772	0.0752	0.0810	0.1598
MSM-c	0.0810	0.0795	0.0810	0.0935	0.2011
MSM-5%	0.0500	0.0500	0.0524	0.0627	0.1409

Table 12. Maximum responses of the frame building.

Method	Max. Dis. (m)	Max. Vel. (m/sec)	Max. Accel. (m/sec²)
SSM	0.3941	0.3409	0.6119
DOEA	0.2933	0.3597	0.4919
MSM-a	0.2423	0.2970	0.4304
MSM-b	0.2571	0.3131	0.4338
MSM-c	0.2480	0.3029	0.4312
MSM-5%	0.2754	0.3382	0.4764

3.4. Example 4

In this example the damper from second floor has been replaced on the fifth floor of the structure, and the same steps in Example 3 has been repeated here. The comparative vibrational graphs of each storey exist in Rasa (2017).

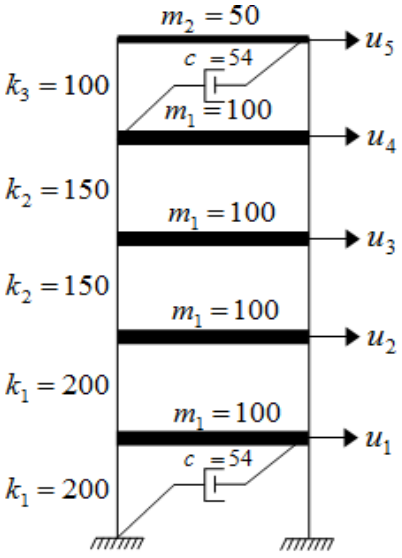

Fig. 10. Five-storey structure with two dampers at the first and fifth floors.

$$\boldsymbol{c} = \begin{bmatrix} 54 & 0 & 0 & 0 & 0 \\ 0 & 0 & 0 & 0 & 0 \\ 0 & 0 & 0 & 0 & 0 \\ 0 & 0 & 0 & 54 & -54 \\ 0 & 0 & 0 & -54 & 54 \end{bmatrix}$$

Table 13. Exact and approximate mode frequencies of the building.

SSM	v_n	DOEA and MSM	ω_n
v_1	$-0.1065 \pm i2.4574$	ω_1	2.4915
v_2	$-0.1653 \pm i1.9460$	ω_2	2.1246
v_3	$-0.6958 \pm i1.6449$	ω_3	1.6756
v_4	$-0.1033 \pm i1.1692$	ω_4	1.1374
v_5	$-0.0090 \pm i0.4212$	ω_5	0.4205

As seen in Table 14, the closest result to the exact modal damping ratios of the frame building is calculated by DOEA method. The modal damping ratios obtained by other five approximate methods (MSM-a, MSM-b, MSM-c, and MSM-5%) are seen to be larger than that of exact method. In approximate methods, fourth and fifth modal damping ratios are found to be larger than that of exact method. In Table 15, the maximum responses (0.2490 m, 0.294 m/sec and 0.4391m/sec2) which, are calculated by DOEA method, are close to that of exact method. Among these five approximate methods (DOEA, MSM-a, MSM-b, MSM-c, and MSM-5%), the most deviation occurs in MSM-a method with the rate of 15.13%. Due to the high rigidity and small natural frequencies of the frame building, the dampers could be placed in the first and fifth floors.

Table 14. Exact and approximate modal damping ratios of the building.

Method	ζ_1	ζ_2	ζ_3	ζ_4	ζ_5
SSM	0.0433	0.0846	0.3896	0.0880	0.0214
DOEA	0.0473	0.1889	0.2588	0.0216	0.1039
MSM-a	0.1253	0.1253	0.1312	0.1572	0.3531
MSM-b	0.1253	0.1194	0.1163	0.1253	0.2472
MSM-c	0.1253	0.1230	0.1253	0.1446	0.3112
MSM-5%	0.0500	0.0500	0.0524	0.0627	0.1409

Table 15. Maximum responses of the frame building.

Method	Max. Dis. (m)	Max. Vel. (m/sec)	Max. Accel. (m/sec²)
SSM	0.2553	0.3043	0.4785
DOEA	0.2490	0.2940	0.4391
MSM-a	0.2169	0.2665	0.4061
MSM-b	0.2304	0.2769	0.4080
MSM-c	0.2211	0.2694	0.4068
MSM-5%	0.2754	0.3382	0.4764

4. Conclusions

In this article, a comparative research has been conducted between the exact and approximate solution of structural vibration of multi storey buildings. The procedure has been implemented utilizing state-space method and mode superposition method, and illustrated by four examples. Considering the dynamical parameters and vibrations of frame buildings, the following results have been obtained:

- In approximate methods (DOEA, MSM-a, MSM-b, MSM-c, and MSM-5%), the maximum responses have generally occurred in the steady-state vibration part while in exact method (SSM) the maximum responses have occurred in the transient vibration part.
- Among five approximate methods (DOEA, MSM-a, MSM-b, MSM-c, MSM-5%), the closest response to the exact method was given by the Disregarding the Off-diagonal Elements Approach (DOEA).
- As it was noticed, the results obtained by mode superposition method were not very realistic when the damping ratio of the system was assumed an estimated value (such as 5%). The most deviation occurred in this case was 16.24%.
- In order to obtain better result with mode superposition method; It is recommended to use the average of damping factors, which are calculated by SSM method, as damping factor of frame building.
- It is recommended to use the first and last modes of vibrations when constructing the proportional damping matrix. The results obtained in this case are less accurate than DOEA method.

Damping mechanism of real structures is not a completely solved topic. Therefore, this research can be extended to detect the most suitable type of damping mechanism which can represent the real or near to the real behavior of structures.

In order to validate the results obtained by these methods, an experimental analysis of three and five storey frame buildings or a theoretical research utilizing other types of proportional/non-proportional damping matrix in the system, could be carried out as a future research problem. These observations could be emphasized applying earthquake loads on the system.

References

Avcar M (2104). Free vibration analysis of beams considering different geometric characteristics and boundary conditions. *International Journal of Mechanics and Applications*, 4(3), 94-100.

Borino G, Muscolin G (1986). Mode-Superposition methods in dynamic analysis of classically and non-classically damped linear systems. *Earthquake Engineering and Structural Dynamics*, 14, 705-717.

Caughey TK (1960). Classical normal modes in damped linear dynamic systems. *Journal of Applied Mechanics*, 27, 269-271.

Caughey TK, O'Kelly M (1965). Classical normal modes in damped linear dynamic system. *Journal of Applied Mechanics*, 32(3), 583-588.

Civalek O, Avcar M (2020). Free vibration and buckling analyses of CNT reinforced laminated non‐rectangular plates by discrete singular convolution method. *Engineering with Computers.*

Felszeghy SF (1993). On uncoupling and solving the equations of motion of vibrating linear discrete systems. *Transactions of the ASME*, 60(2), 456-462.

Rasa AY (2017). Çok Katlı Yapıların Geçici Titreşimlerinin Durum-Uzayı Yaklaşımı ile İncelenmesi ve Modların Birleştirilmesi Yöntemiyle bir Karşılaştırma. *M.Sc. thesis*, Atatürk University, Erzurum, Turkey. (in Turkish)

Sinha R, Igusa T (1992). CQC and SRSS methods for non-classically damped structures. *Earthquake Engineering and Structural Design,* 24, 615-619.

Veletsos AS, Ventura CE (1986). Modal analysis of nonclassically damped linear systems. *Earthquake Engineering and Structure Dynamics,* 14, 217-243.

Villaverde R (2008). A complex modal superposition method for the seismic analysis of structures with supplemental dampers. *The 14th World Conference on Earthquake Engineering*, 12-17, Beijing, China.

Wilson EL, Kiureghian A, Bayo EP (1981). A replacement for the SRSS method in seismic analysis. *Earthquake Engineering and Structural Dynamics*, 9, 187-192.

Wilson EL, Penzien J (1981). Evaluation of orthogonal damping matrices. *International Journal for Numerical Methods in Engineering,* 4, 5-10.

Zhou XY, Yu RF, Liang D (2004). The complex-complete-quadratic combination (CCQC) method for seismic responses of non-classically damped linear MDOF system. *13th World Conference on Earthquake Engineering Vancouver*, B.C., Canada, paper No. 848.

Challenge Journal of Structural Mechanics

Research Article

The effect of dome properties on design of axial symmetric reinforced concrete cylindrical walls

Aylin Ece Kayabekir [a,*]

[a] *Department of Civil Enginering, İstanbul University-Cerrahpaşa, 34320 İstanbul, Turkey*

ABSTRACT

The usage of computer software in civil engineering has expanded in last decades. Many general-purpose and special-purpose commercial programs perform a very important function, especially at the design stage. In this study, a computer program is introduced for the analysis and design of the axial symmetric cylindrical wall considering the dome effects. Analysis processes are carried out according to Flexibility theory with long wall assumption and during the reinforced concrete (RC) design of the wall, ACI 318-Building code requirements for structural concrete are considered. In numerical investigation, the effects of the dome properties (thickness and height) on the analysis and design of the wall are investigated by performing a totally 72 case analyzes. These cases include different support condition at bottom of the wall, wall heights, dome thicknesses and heights. According to analysis results, it is concluded that effects of dome thickness and heights on the wall on the wall are very limited.

ARTICLE INFO

Article history:
Received 26 August 2020
Revised 9 October 2020
Accepted 23 October 2020

Keywords:
Cylindrical wall
Dome effect
Flexibility theory
Reinforced concrete design
ACI 318

1. Introduction

Shells are defined as structural members of which thickness is very small compared to other dimensions. These are several practical applications of these structural members such as places of worship, dams, water tanks etc.

When the equations used in the analysis of these structural elements are derived by writing equilibrium equations on a small part of the shell, it is seen that these equations contain four integration constants depending on the boundary conditions. These integration constants need to be determined to solve the equations. For this reason, many scientific studies have been conducted on the solutions of these equations until today. One of the methods used in these alternative solutions is the theory of beams on elastic foundation. The situation that enables this theory to be used in the cylindrical wall, is the similarity of the differential equations of the wall and beams. This situation has led to a rapid development in both scientific areas, as the analysis methods developed for the wall and can be used mutually. In this section, some important studies in the analysis methods of both structural members are summarized below.

A first model for the beams on elastic foundation was proposed by Winkler in 1867. According to this model, foundation is represented by infinite number of independent springs are used. Between the reaction forces on the soil and the displacement of the beams at that point, there is a ratio which is equal to the spring coefficient of the elastic springs. Also, it is assumed that the members that change shape under the applied load will return to their original state if the load is removed (Wang et al., 2005; Karaşin and Gülkan, 2008). Using this soil model, Winkler conducted stress analysis on railways. In the analysis, the rails were defined with beams and the displacements were obtained by solving the differential equation.

The integral coefficients in the displacement equation of the beam change with discontinuities in load distribution on the beam. This situation makes the determination of integral constants difficult. For that reason, various methods have been developed to overcome this problem. Initial parameter method developed by Umansky (1933) and the superposition method developed by Hetenyi (1936) are well known methods in scientific studies.

* *Corresponding author*. Tel.: +90-212-473-7070 ; Fax: +90-212-473-7180 ; E-mail address: ecekayabekir@gmail.com (A. E. Kayabekir)
ISSN: 2149-8024 / DOI: https://doi.org/10.20528/cjsmec.2021.01.002

The book written by Hetenyi in 1946 is one of the most important sources on this subject. Some other important books on this subject were written by Henry (1956), Jones (1997), Melerski (2000). Information on many solution methods can be found in these books. Apart from these, there are many methods published in various sources regarding the solution of the beams on elastic ground (Vianello, 1898; Cross, 1930; Levinton, 1947; Penzien, 1960; Miranda and Nair, 1966; Beaufait, 1977; Ting, 1982; Yankelevsky et al., 1989).

In the book called thin sell structures written by Billington in 1965, beam-wall similarity in the solution of the differential equation and flexibility theory in the analysis were used. Except this, the studies done by Bekdaş (2015; 2018; 2019) can be also given as examples for the analysis of the axial symmetric cylindrical walls.

In this study, a computer program has been developed for the design and analysis of the axial symmetric cylindrical wall considering the dome effects. Flexibility theory was used in the wall analyzes performed according to the long wall assumption. During the reinforced concrete design, rules of ACI 318 regulation are used. As numerical examples, totally 72 case analyses are done in order to observe effect of dome on design and analysis of the wall. In these cases, different support condition at the bottom and dome properties at the upper section for different wall height are investigated.

2. Analysis and Design Process

Analysis and design process of the axial symmetric cylindrical walls can be summarized with two main stages. First stage is entering the data of structure. These data contain geometrical and sectional properties for wall and dome (thickness, height, radius, etc.), material properties (elasticity modulus, Poisson's ratio, etc), support conditions of the bottom section wall and unit material cost for concrete and steel. In the second stage wall with dome calculations are performed. These calculations are done in three steps. These steps are:

- Calculation of the wall displacements and internal forces;
- RC design of the wall in accordance with ACI 318 requirements;
- Determination of total wall material cost concrete and steel rebar.

This process is also given in the flowchart (Fig. 1).

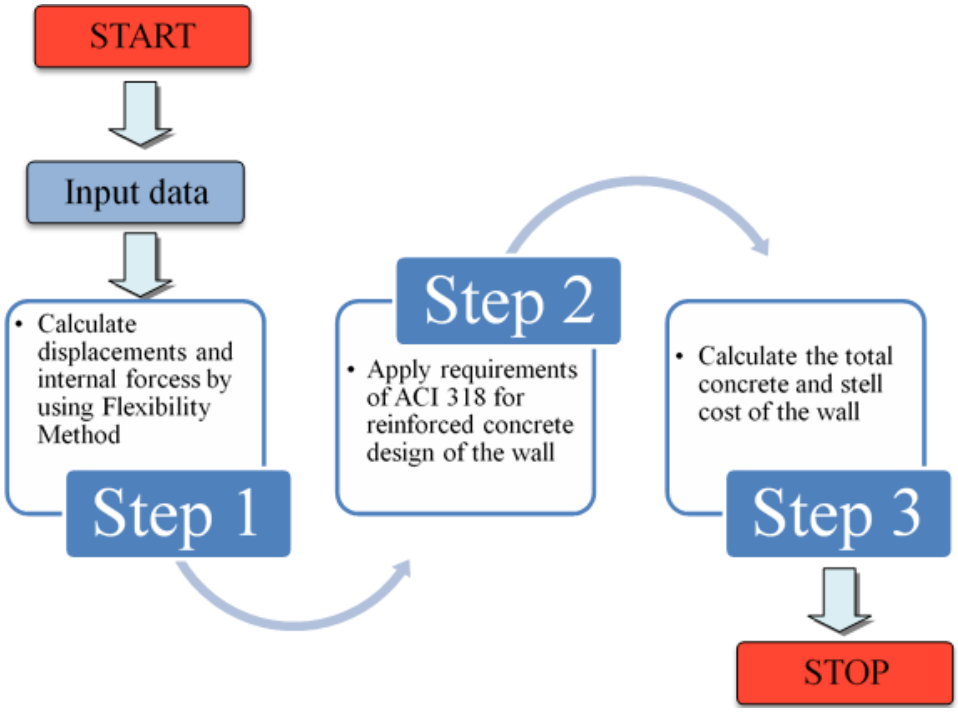

Fig. 1. Flowchart of the developed program.

2.1. Flexibility method for the analysis of the cylindrical walls with dome

In this section, the application of the flexibility method to the axial symmetric cylindrical walls with dome will be introduced. Accordingly, unknown forces at the bottom and the upper section of the wall are calculated on the equivalent isostatic system. During calculations of the unknown forces, at the bottom section only wall with fixed (or simple) support, at the upper section wall and dome connection are taken consideration. The wall and circular dome are directly connected without using a stiffness ring beam in this study. In that case, the connection is provided as a continuous connection and the analysis were done according to this assumption. In future studies, the connection with using a stiffness ring beam can be also investigated.

In Fig. 2, fixed supported wall under the liquid loads and the equivalent isostatic demonstration of the wall is given. In the figure, the triangle distributed loads, X_1 and X_2 show the liquid loads, lateral and rotational redundant forces respectively.

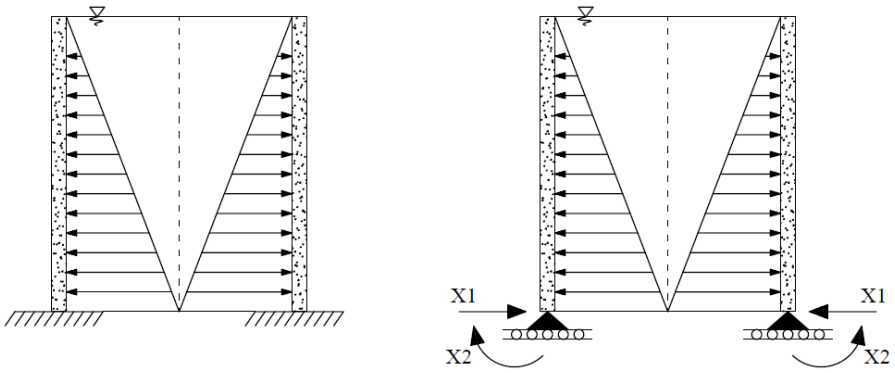

Fig. 2. Fixed supported cylindrical wall and equivalent isostatic system of the wall.

The redundant forces can be easily found by compatibility equations of system. For the fixed supported cylindrical walls, since there is no relative displacement at the support point, compatibility equations can be written as in Eq. (1).

$$D_{10} + F_{11}X_1 + F_{12}X_2 = 0 \quad \text{and}$$

$$D_{20} + F_{22}X_2 + F_{21}X_2 = 0 \tag{1}$$

In Eq. (1), D_{10} and D_{20} represent the displacements due to external loads in the freedoms corresponding to X_1 and X_2, respectively. F_{11}, F_{12}, F_{21} and F_{22} show flexibility coefficients. These flexibility terms indicate the displacement in the freedom indicated by the first subscript in case of a unit force applied to the freedom indicated by the second subscript.

The lateral (D_{10}) and rotational displacements (D_{20}) can be found by;

$$D_{10} = -\frac{\gamma r^2 H}{Eh} \quad and \quad D_{20} = \frac{\gamma r^2}{Eh} \tag{2}$$

where γ, r, H, E and h are density of liquid, radius of the wall, wall height, elasticity modulus and wall thickness respectively.

Flexibility coefficients can be calculated as in Eq. (3).

$$F_{11} = \frac{1}{2\beta^3 D} \quad , \quad F_{22} = \frac{1}{\beta D} \quad and \quad F_{12} = F_{21} = -\frac{1}{2\beta^2 D} \tag{3}$$

In Eq. (3), β and D are parameters (Eq. 4), including rigidity and geometrical properties, and flexural rigidity (Eq. 5) respectively.

$$\beta = \sqrt[4]{\frac{Eh}{4r^2 D}} = \sqrt[4]{\frac{3(1-\nu^2)}{r^2 h^2}} \tag{4}$$

$$D = \frac{Eh^3}{12(1-\nu^2)} \tag{5}$$

In Eqs. (4-5), ν represent Possion's ratio. If Eqs. (2-5) are implemented in Eq. (1), redundant forces will be;

$$\begin{bmatrix} X_1 \\ X_2 \end{bmatrix} = F^{-1} \begin{bmatrix} -\frac{\gamma \cdot r^2 \cdot H}{E \cdot h} \\ \frac{\gamma \cdot r^2}{E \cdot h} \end{bmatrix} \tag{6}$$

As mentioned before for the calculations at the upper section, wall and dome are considered together. The displacement and flexibility terms for the dome written as;

$$D_{10d} = \frac{r_d^2 q}{E_d h_d}\left(\frac{1+\nu_d}{1+\cos\alpha} - \cos\alpha\right)\sin\alpha \quad and$$

$$D_{20d} = \frac{r_d q}{E_d h_d}(2+\nu_d)\sin\alpha \tag{7}$$

$$F_{11d} = \frac{2 r_d \lambda_d \sin^2\alpha}{E_d h_d} \quad , \quad F_{12d} = F_{21d} = \frac{2\lambda_d^2 \sin\alpha}{E_d h_d} \quad and$$

$$F_{22d} = \frac{4\lambda_d^3}{E_d h_d r_d} \tag{8}$$

where the terms represent r_d, radius; ν_d, Poisson ratio; α, starting angle; E_d, modulus of elasticity; h_d, thickness of the dome; λ_d, a constant parameter including rigidity, geometrical properties; and q, distributed load on the dome.

The wall terms previously calculated for the bottom section is also valid for upper section. After by superposing of the wall and dome terms, the redundant forces can be calculated;

$$\begin{bmatrix} X_3 \\ X_4 \end{bmatrix} = F_s^{-1} \begin{bmatrix} D_{10s} \\ D_{20s} \end{bmatrix} \tag{9}$$

For further detailed information can be found in reference book of Billington (1965).

2.2. Reinforced concrete design of the cylindrical wall

In this section, design constants of the problem are summarized. According to the regulation of ACI 318-Building code requirements for structural concrete, these constraints are listed in the Table 1. As seen from the table, mainly these requirements are related to sections capacities and limits for area and orientation of reinforcement design.

3. Numerical Investigation

In this section, several numerical cases including different wall support condition and wall height, dome thickness and height are presented in order to investigate the effect of dome properties on cylindrical wall

analyses and design. Totally 72 cases are considered. In these cases, fixed and simple support at the bottom of the wall, 5-7 m for wall height, 2.5 m and 4.5 m dome heights and 0.2-0.3m dome thickness (0.02 m increment) are used. The other design parameters of the problem are presented in the Table 2.

Table 1. Design constraints.

Description	Constraints
Flexural strength capacity, M_d	$M_d \geq M_u$
Shear strength capacity, V_d	$V_d \geq V_u$
Minimum steel ratio, ρ_{min}	$A_s \geq A_{smin}$
Maximum steel bars spacing, S_{max}	$S \leq S_{max}$
Minimum steel bars spacing, S_{min}	$S \geq S_{min}$
Minimum concrete cover, c_{cmin}	$c_{cmin} \geq 40$ mm

Table 2. Design parameters for cases.

Definition	Value
Radius of wall, R (m)	8
Height of the wall, H (m)	5-7
Yield strength of steel, f_y (MPa)	420
Concrete cover, c_c (mm)	50
Compressive strength of concrete, f'_c (MPa)	30
Elasticity modulus of concrete, E_c (MPa)	$4700(f'_c)^{1/2}$
Poisson ratio of concrete, ν	0.2
Density of liquid, γ (kN/m^3)	7
Minimum reinforcement ratio, ρ_{min}	0.008
Unit concrete cost, C_c (TL/m^3)	200
Unit steel cost, C_s, TL/ton	5000

3.1. Simple support cases

This section presents the effects of the thickness (h_d) and height (H_d) of the dome on longitudinal moments and design for the simple supported cylindrical wall. For this purpose, the analyses of 36 different cases are conducted. An iterative way is followed during determining the wall thicknesses used in the analyzes. The minimum wall thickness, which provides all design constraints, is used in the design by repeating the analyzes for each wall height (H). In this way, it is aimed to find more economical results in terms of cost. Accordingly, the thickness values for the heights of 5m, 6m and 7m were obtained as 0.25, 0.3 and 0.35 m, respectively.

In Fig. 3, each graph corresponds the longitudinal moment distribution according to six different dome thicknesses for a constant wall and dome height.

When each wall height cases are evaluated within itself, by considering different dome thicknesses it is seen that the differences between the maximum moment on the wall and the moment at the junction point of the wall-dome are relatively small. At points with maximum moments it is understood that this difference is below 0.07% and this difference also does not change the wall design as well as material cost of the wall. A similar situation is valid for the height of the dome. The maximum difference depending on the height of the dome was found to be 0.22%.

Therefore, it is concluded that the effect of both dome thickness and height on the analysis and design is quite limited for the analyzed cases.

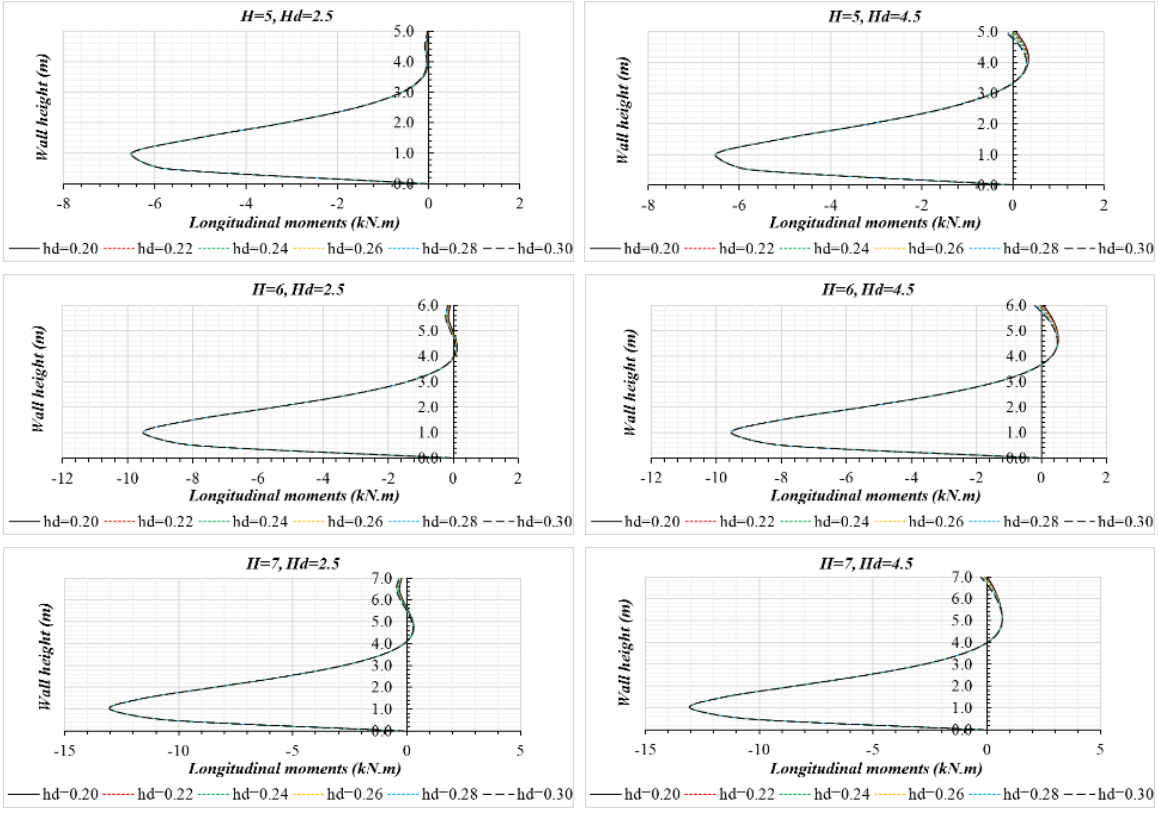

Fig. 3. Simple supported wall height-longitudinal moment graphs for different cases.

3.2. Fixed support cases

The same investigations are also done for fixed supported cylindrical wall. In this section, the results of these investigations are presented. Similar 36 cases are handled for fixed supported wall. According to the iterative process for obtaining minimum thickness, the wall thickness values are found 0.3, 0.35 and 0.45 m for 5m, 6m and 7m wall heights, respectively. In Fig. 4, longitudinal moment along wall height can be seen. Each graph corresponds six different dome thicknesses for a constant wall and dome height.

The analysis results show that the effect of dome thickness and height on longitudinal moment is quite limited, as in simple supported cases. For that reason, the wall design as well as material cost of the wall are same for the cases presented in each graph. When each plot is evaluated separately, it is concluded that the maximum differences are below 0.01% and 0.28% for the moments in fixed support, maximum moments along the wall respectively. If a similar comparison is done according to the dome height, the differences are seen to be 0.11% and 0.37%.

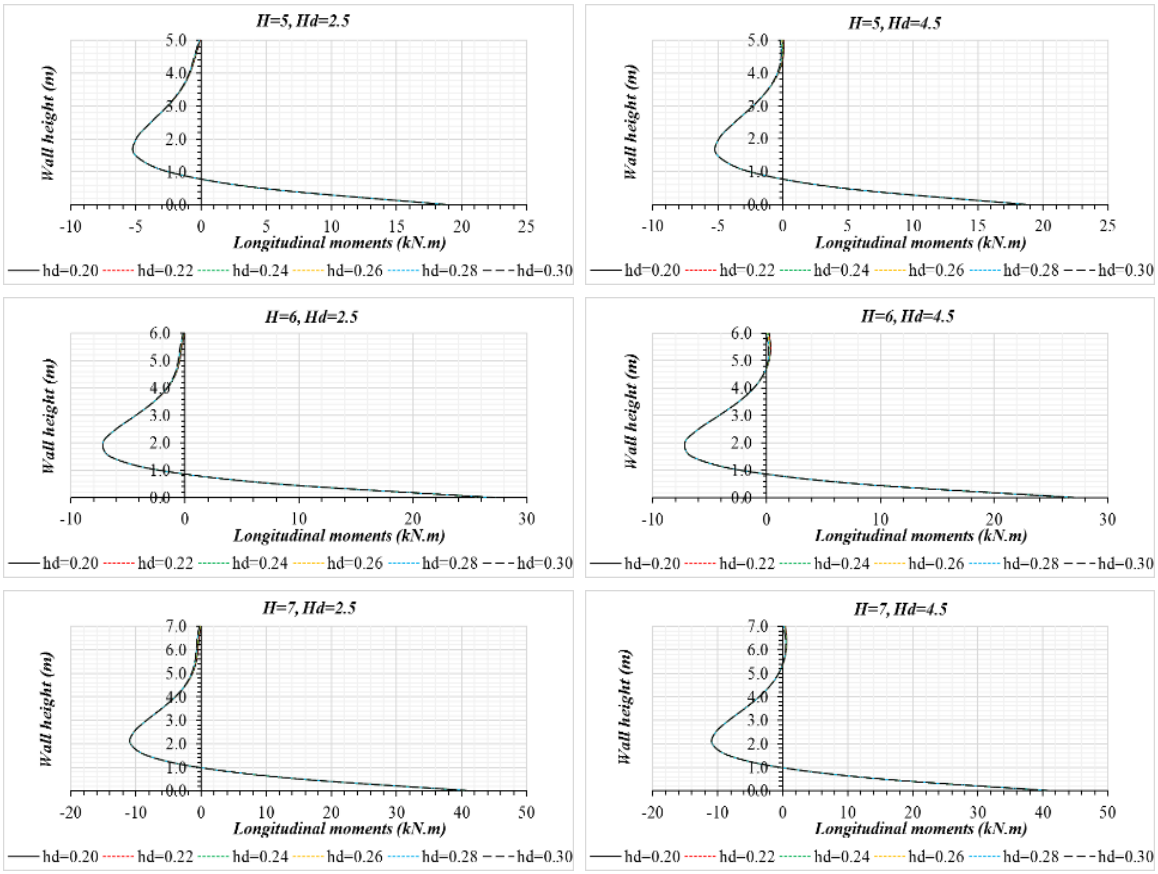

Fig. 4. Fixed supported wall height-longitudinal moment graphs for different cases.

4. Conclusions

In this study, a computer program has been developed to perform the analysis and design of axial symmetrical walls with a dome. In the analyzes, flexibility theory was considered, and reinforced concrete design was done according to ACI 318-Building code requirements for structural concrete. Total of 72 cases including different support conditions (fixed and simple) at the bottom of the wall, wall heights, dome heights and thicknesses were considered to investigate effect of dome properties on the longitudinal moment distribution and design of the wall.

For a constant wall height, wall thicknesses were determined according to the minimum value that provides design constraints by using 0.5 m increments. According to analyzes results, the effects of dome thickness and heights are quite limited in the simple support cases. When this effect is defined by the maximum moments on the wall for a specific wall and dome height, differences are below %0.07 and %0.22 for different dome thicknesses and heights respectively. When the similar evaluations were done for fixed support cases, it was seen that the maximum differences between the moments were found to be 0.28% and 37% for dome thickness and height, respectively. It was understood that these differences did not have any effect on the cost of the wall design for the solved 36 cases.

For future studies in order to verify these results, analyzes can be done for different loading conditions and dimensions for wall and dome). In addition, by adding an optimization module to the program, the lowest cost designs can be obtained. Scientific data to be obtained from these studies may guide engineers in practical applications as well as in design.

Publication Note

This research has previously been presented at the 6th International Conference on Harmony Search, Soft Computing and Applications (ICHSA 2020) held in İstanbul, Turkey, on July 16-17, 2020. Extended version of the research has been submitted to Challenge Journal of Structural Mechanics and has been peer-reviewed prior to the publication.

References

Beaufait FW (1977). Numerical Analysis of beams on elastic foundations. *Journal of the Mechanics Division Proceedings of the ASCE*, 103, 205-209.

Bekdaş G (2015). Harmony search algorithm approach for optimum design of post-tensioned axially symmetric cylindrical reinforced concrete walls. *Journal of Optimization Theory and Applications*, 164(1), 342-358.

Bekdaş G (2018). New improved metaheuristic approaches for optimum design of posttensioned axially symmetric cylindrical reinforced concrete walls. *The Structural Design of Tall and Special Buildings*, 27(7), e1461.

Bekdaş G (2019). Optimum design of post-tensioned axially symmetric cylindrical walls using novel hybrid metaheuristic methods. *The Structural Design of Tall and Special Buildings*, 28(1), e1550.

Billington DP (1965). Thin Shell Structures. McGraw-Hill, New York.

Cross H (1930). Analysis of continuous frames by distributing fixed-end moments. *Proceeding of the ASCE*, 57, 919-928.

Henry FDC (1956). The Design and Construction of Engineering Foundations. Mc-Graw Hill, New York.

Hetenyi M (1936). Analysis of bars on elastic foundation. *Final Report of the second International Congress for Bridge and structural Engineering* (*English Edition*), October Berlin- Munich, Verlag von Wilhelm Ernst and Son, 846-851.

Hetenyi M (1946). Beams on Elastic Foundation. The University of Michigan Press, Ann Arbor.

Jones G (1997). Analysis of Beams on Elastic Foundations using Finite Difference Theory. Thomas Telford Publishing, New York.

Karaşin HA, Gülkan P (2008). Elastik zeminlere oturan plakların sonlu ızgara yöntemi ile yaklaşık çözümü. *Teknik Dergi*, 293, 4445-4454. (in Turkish)

Levinton Z (1947). Elastic foundation analysed by the method of redundant reactions. *Journal of the Structural Division, Proceedings of the ASCE*, 73, 1529-1541. (also in *Transactions ASCE*, 114, 40-52).

Melerski ED (2000). Design Analysis of Beams. Circular Plates and Cylindrical Tanks on Elastic Foundations. Taylor & Francis Group, London.

Miranda C, Nair K (1966). Finite beams on elastic foundation. *Journal of the Structural Division, Proceedings of the ASCE*, 92, 131-142.

Penzien J (1960). Discontinuity stresses in beams on elastic foundation. *Journal of the Structural Division, Proceeding of the ASCE*, 86, 67-97.

Ting BY (1982). Finite beams on elastic foundation with restraints. *Journal of the Structural Division, Proceedings of the ASCE*, 108, 611-621.

Umansky AA (1933). Analysis of Beams on Elastic Foundation. Central Research Institute of Auto-Transportation, Leningrad.

Vianello L (1898). Graphische Untersuchungen der knickfestigkeit gerader stabe. *Zeitschrift des Vereins Deutscher Ingenieure*, 42, 1436-1443. (in German)

Wang YH, Tham LG, Cheung YK (2005). Beams and plates on elastic foundations: a review. *Progress in Structural Engineering and Materials*, 7,174–182.

Winkler E (1867). Die Lehre von der Elasticitaet und Festigkeit – mit besonderer Rücksicht auf ihre Anwendung in der Technik. Für polytechnische Schulen, Bauakademien, Ingenieure, Maschinenbauer, Architekten, etc., Verlag H. Dominicus, Prag. (in German)

Yankelevsky DZ, Eisenberger M, Adin MA (1989). Analysis of beams on nonlinear winkler foundation. *Computer and Structures*, 31, 287-292.

Challenge Journal of Structural Mechanics

Research Article

Evaluation of artificial neural network-based formulations for tuned mass dampers

Melda Yucel [a,*], Sinan Melih Nigdeli [a], Gebrail Bekdaş [a]

[a] *Department of Civil Enginering, İstanbul University-Cerrahpaşa, 34320 İstanbul, Turkey*

ABSTRACT

Tuned mass dampers (TMDs) are used to damp vibration of mechanical systems. TMDs are also used on structures to reduce the effects of strong forces such as winds and earthquakes. For the efficiency of TMD, optimization of TMD parameters is needed. Several classical formulations were proposed, but metaheuristic methods are generally used to find the best result. In addition, the metaheuristic based optimum results are used in machine learning of artificial intelligence-based models like artificial neural networks (ANN). These ANN models are also used in development of tuning equation via curve fitting. The classical and ANN-based formulations were found according to frequency domain responses. In the present study, the classical and ANN-based formulations were evaluated by comparing on time-history responses of seismic structure. In comparison, near-fault ground motion records including directivity pulses are used. The ANN based methods have advantages by providing smaller stroke requirement and damping for TMDs.

ARTICLE INFO

Article history:
Received 29 August 2020
Revised 13 October 2020
Accepted 23 October 2020

Keywords:
Artificial neural networks
Tuned mass dampers
Structural control
Optimization
near-fault
Metaheuristic

1. Introduction

In order to reduce structural vibrations, several control methods have been proposed. These methods may be passive, active, semi-active or hybrid control methods. All systems of different control strategies need to be optimized to find a perfect tuning of parameters according to controlled structure subjected to vibration sources like earthquakes, winds and traffics.

Tuned mass dampers are passive vibration control devices which are used in general mechanical systems. For this purpose, several simplified equations are proposed (Den Hartog, 1947; Warburton, 1982; Sadek et al., 1997; Leung and Zhang, 2009; Yucel et al., 2019). These equations were derived according to mathematical equations, curve fitting of numerical iteration and optimum results as details given in Section 2.1.

In recent years, the most chosen methods for optimum tuning of mass dampers is the usage of metaheuristic methods. As examples, the usage of harmony search (HS) (Bekdaş and Nigdeli, 2011; Nigdeli and Bekdaş, 2017), particle swarm optimization (Khatibinia et al., 2016), ant colony algorithm (Viana et al., 2008), genetic algorithm (Mohebbi et al., 2013; Pourzeynali et al., 2013; Arfiadi, 2016), artificial bee colony optimization (Farshidianfar and Soheili, 2013), simulated annealing (Yang and Li, 2016), cuckoo search (Etedali and Mollayi, 2018), gravitational algorithm (Khatibinia et al., 2018), bat algorithm (Bekdaş et al., 2018) and flower pollination (FPA) (Bekdaş et al., 2017); besides the usage of both harmony search, flower pollination algorithm, teaching-learning based optimization and jaya algorithm (Bekdaş et al., 2019) were proposed to optimize different types of TMDs for different objectives about responses of structures.

The process of numerical optimization method may need high amount of computation time. For that reason, Yucel et al. (2019) used the optimum TMD parameters on machine learning of an artificial neural network (ANN) model, and several equations were developed for easy use of engineers.

The classical and ANN-based formulations were found according to frequency-domain response of structures. The exact effect of TMDs can be only seen on time-history responses. For that reason, several formulations

* *Corresponding author*. E-mail address: melda.yucel@yahoo.com.tr (M. Yucel)
ISSN: 2149-8024 / DOI: https://doi.org/10.20528/cjsmec.2021.01.003

are investigated on time-history responses of seismic structures by using near-fault ground motions. As seen in Fig. 1, near fault ground motion have two significant impulsive motions.

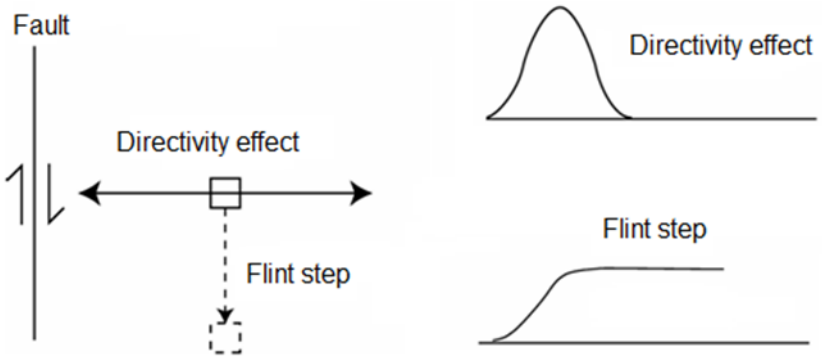

Fig. 1. Impulsive motions.

Directivity pulses, which are critically effective on structures, occur in the direction perpendicular to fault (Steward et al., 2001). These pulses have long period and high peak ground velocity. In FEMA P-695: Quantification of Building Seismic Performance Factors (2009), several near fault ground motion records with pulses are grouped, and these records given in Table 1 were used in the present study.

Table 1. Earthquake set for near-field excitations with pulses (FEMA P-695, 2009).

Earthquake No.	Earthquake Name	Recording Station	Year	Magnitude
1	Imperial Valley-06	El Centro Array #6	1979	6.5
2	Imperial Valley-06	El Centro Array #7	1979	6.5
3	Irpinia, Italy-01	Sturno	1980	6.9
4	Superstition Hills-02	Parachute Test Site	1987	6.5
5	Loma Prieta	Saratoga – Aloha	1989	6.9
6	Erzican, Turkey	Erzican	1992	6.7
7	Cape Mendocino	Petrolia	1992	7.0
8	Landers	Lucerne	1992	7.3
9	Northridge-01	01 Rinaldi Receiving Sta	1994	6.7
10	Northridge-01	01 Sylmar - Olive View	1994	6.7
11	Kocaeli, Turkey	Izmit	1999	7.5
12	Chi-Chi, Taiwan	TCU065	1999	7.6
13	Chi-Chi, Taiwan	TCU102	1999	7.6
14	Duzce, Turkey	Duzce	1999	7.1

2. Design of Tuned Mass Dampers

2.1. Equations of motion

In Fig. 2, a TMD attached to a single degree of freedom (SDOF) structures is shown. $\ddot{x}_g$ is the recorded acceleration of ground motions. The response of the structure is the displacement (x). The structural parameters taken as the design constants are the mass (m), stiffness (k) and the damping coefficient (c), which are found according to the inherent damping (ξ) of the structure as given in Eq. (1).

$$c = 2m\xi\sqrt{\frac{k}{m}} \tag{1}$$

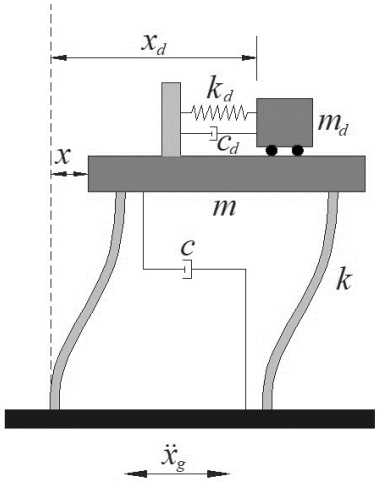

Fig. 2. SDOF structure with TMD.

The parameters of TMD are mass (m_d), stiffness (k_d) and damping coefficient (c_d) of the structure. Generally, the mass of TMD is optimum at the highest allowed value according to axial loading capacity of the structure. In tuning formulations, mass ratio (μ) is defined as given in Eq. (2).

$$\mu = \frac{m_d}{m} \tag{2}$$

In matrix form, the equation of motion of structure coupled with a TMD is given as Eq. (3). The mass, damping and stiffness matrices are shown as M, C and K, respectively. These matrices and the displacement vector ($x(t)$) are shown in Eqs. (4-7).

$$M\ddot{x}(t) + C\dot{x}(t) + Kx(t) = -M[1]\ddot{x}_g(t) \tag{3}$$

$$M = \begin{bmatrix} m & 0 \\ 0 & m_d \end{bmatrix} \tag{4}$$

$$C = \begin{bmatrix} c + c_d & -c_d \\ -c_d & c_d \end{bmatrix} \tag{5}$$

$$K = \begin{bmatrix} k + k_d & -k_d \\ -k_d & k_d \end{bmatrix} \tag{6}$$

$$x(t) = \begin{Bmatrix} x \\ x_d \end{Bmatrix} \tag{7}$$

The dots on $x(t)$ represent a derivative of $x(t)$ respect to time. Solving of x needs long calculation time, and the results are specific for the excited ground acceleration. Due to that, the response can be investigated in frequency domain (ω) by calculating the amplitude (f) of transfer function (TF(ω)). TF(ω) is the ratio of Laplace transformations of acceleration of the system and ground. TF(ω) and f are formulated as Eqs. (8) and (9), respectively.

$$TF(\omega) = \begin{bmatrix} TF \\ TF_d \end{bmatrix} = [-M\omega^2 + C\omega j + K]^{-1} M\omega^2\{1\} \tag{8}$$

$$f = 20\mathrm{Log}_{10}|\max(TF)| \tag{9}$$

2.2. Tuning equations for TMDs

In Table 2, the compared tuning equations with ANN-based equations are given. The equations are for optimum frequency ratio (f_{opt}) and optimum damping ratio TMD ($\xi_{d,\mathrm{opt}}$). f_{opt} and $\xi_{d,\mathrm{opt}}$ are formulated as Eqs. (10) and (11), respectively.

Table 2. The frequency and damping ratio expressions of the compared methods.

Method	f_{opt}	$\xi_{d,\mathrm{opt}}$
Den Hartog (1947)	$\frac{1}{1+\mu}$	$\sqrt{\frac{3\mu}{8(1+\mu)}}$
Warburton (1982)	$\frac{\sqrt{1-\left(\frac{\mu}{2}\right)}}{1+\mu}$	$\sqrt{\frac{\mu\left(1-\frac{\mu}{4}\right)}{4(1+\mu)\left(1-\frac{\mu}{2}\right)}}$
Sadek et al. (1997)	$\frac{1}{1+\mu}\left[1-\xi\sqrt{\frac{\mu}{1+\mu}}\right]$	$\frac{\xi}{1+\mu}+\sqrt{\frac{\mu}{1+\mu}}$
Leung and Zhang (2009)	$\frac{\sqrt{1-\left(\frac{\mu}{2}\right)}}{1+\mu}+\left(-4.9453+20.2319\sqrt{\mu}-37.9419\mu\right)\sqrt{\mu}\xi+(-4.8287+25.0000\sqrt{\mu})\sqrt{\mu}\xi^2$	$\sqrt{\frac{\mu\left(1-\frac{\mu}{4}\right)}{4(1+\mu)\left(1-\frac{\mu}{2}\right)}}-5.3024\xi^2\mu$

$$f_{opt} = \frac{\omega_d}{\omega_s} \tag{10}$$

$$\xi_{d,\mathrm{opt}} = \frac{c_d}{2m_d\omega_d} \tag{11}$$

$\omega_{d,\mathrm{opt}}$ is the frequency of the TMD as given in Eq. (12), and ω_s is the frequency of single degree of freedom (SDOF) structure as shown in Eq. (13).

$$\omega_d = \sqrt{\frac{k_d}{m_d}} \tag{12}$$

$$\omega_s = \sqrt{\frac{k}{m}} \tag{13}$$

The equation of Den Hartog (1947) was found for harmonic excitations. Warburton (1982) derived the formulation for white-noise excitation. Sadek et al. (1997) used curve-fitting of numerical optimization results to find a formulation including the effect of inherent damping of the structure. Leung and Zhang (2009) employed PSO to find the TMD tuning equations.

2.3. ANN-based formulation for TMD optimization

Artificial neural networks (ANN) are an artificial intelligence modelling tool, and it based on simulating human brain behavior on different systems. Via ANN, it is possible estimate final results without processing the solving of problems. Yucel et al. (2019) developed an ANN model for

optimization of TMDs providing optimum period (T_d) and damping ratio ($\xi_{d,\text{opt}}$) of TMDs. The relationship between T_d and stiffness of TMD (k_d) is given as Eq. (14).

$$T_d = 2\pi\sqrt{\frac{m_d}{k_d}} \tag{14}$$

The structure of the developed ANN model is shown as Fig. 3. The inputs are the period (T_s) of SDOF structure given as Eq. (15) and mass ratio (μ).

$$T_s = 2\pi\sqrt{\frac{m}{k}} \tag{15}$$

In machine learning of the ANN model, FPA algorithm developed by Yang (2012) was used. The methodology given in Bekdaş et al. (2017) was used to find the optimum TMD values for different cases of SDOF structures. The developed ANN model was used to find the simplified equations given in Table 3.

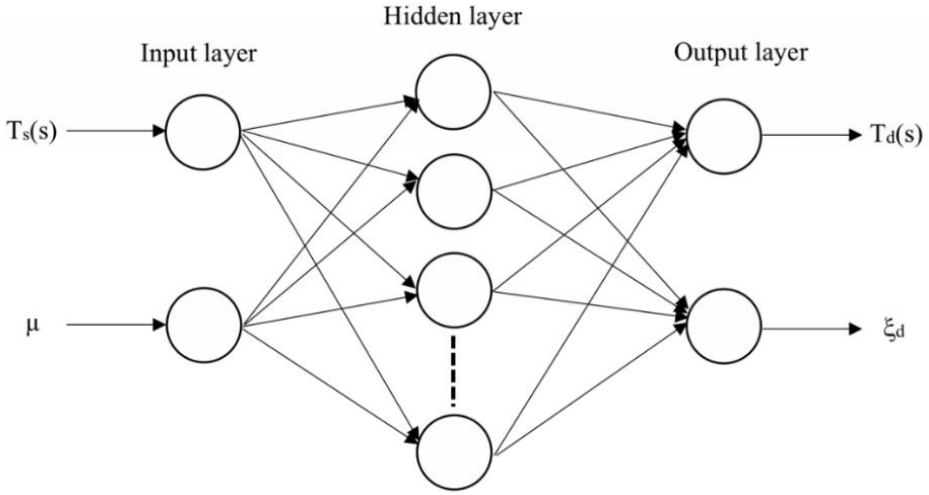

Fig. 3. ANN structure.

Table 3. ANN based formulations (Yucel et al., 2019).

Method	f_{opt}	$\xi_{d,\text{opt}}$
Linear	$f_{\text{opt}} = -0.6438\mu + 0.9966$	$\xi_{d,\text{opt}} = -0.5673\mu + 0.1235$
Polynomial	$f_{\text{opt}} = -249.91\mu^5 + 400.09\mu^4 -208.03\mu^3 + 43.801\mu^2 - 4.1453\mu + 1.0675$	$\xi_{d,\text{opt}} = -54.673\mu^4 + 54.639\mu^3 - 19.274\mu^2 +3.2302\mu + 0.0237$
Exponential	$f_{\text{opt}} = 1.0038\, e^{-0.747\mu}$	$\xi_{d,\text{opt}} = 1.1258\, e^{2.8573\mu}$

3. Comparison of the methods

The investigations were done for four cases of SDOF structure period. All structures were also tested for three mass ratio values. The cases are shown in Tables 4 and 5.

The results of different methods are presented in Tables 6-9 including the sub-cases of mass ratio in Appendix. Also, the comparisons intended for x, a and stroke values within these results of formulations, which were proposed in literature and developed as ANN-based, can be seen in Fig. 4-7 for case 1-4, respectively. The results include the optimum TMD values, maximum displacement (x) and acceleration (a) of the structure. Also, stroke values are presented for the TMD. The presented stroke value is a normalized value as given in Eq. (16).

$$stroke = \frac{max(|x_d|) - max(|x|)}{max(|x|)_{structure\ without\ TMD}} \tag{16}$$

Table 4. Numerical cases for periods.

Case	T_s (s)
1	0.5
2	1
3	2
4	4

Table 5. Numerical cases for mass ratio.

Case	μ
a	0.05
b	0.10
c	0.20

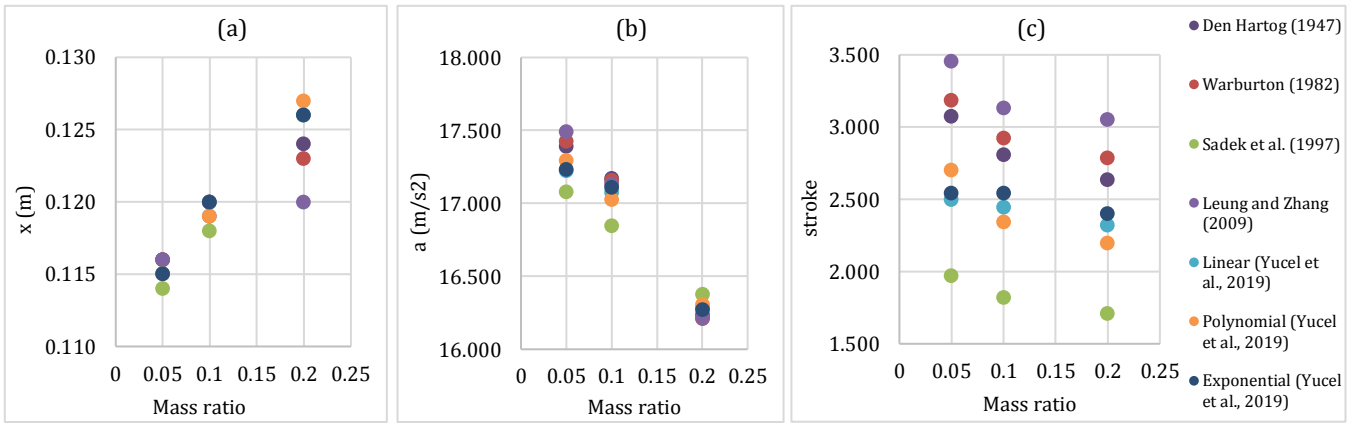

Fig. 4. The numerical results (Case 1): (a) x (m); (b) a (m/s²); (c) stroke.

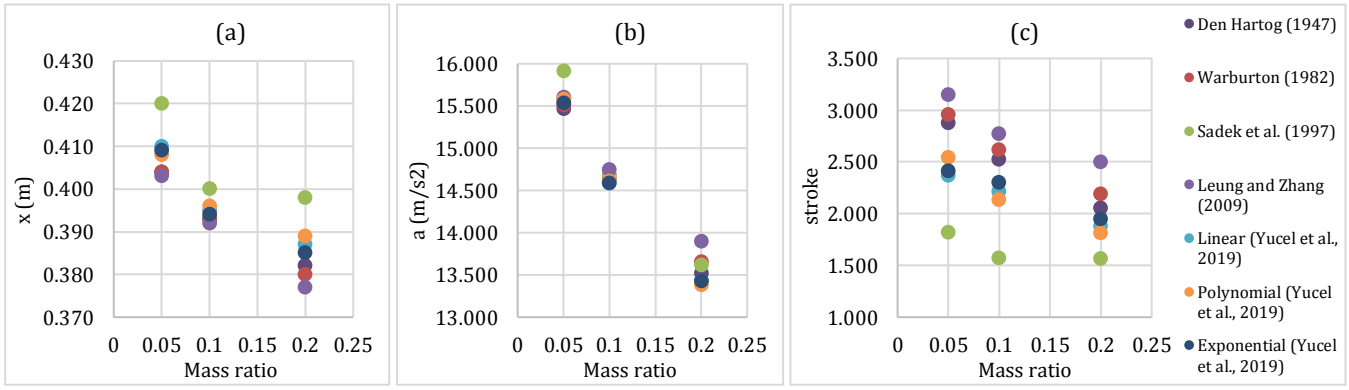

Fig. 5. The numerical results (Case 2): (a) x (m); (b) a (m/s²); (c) stroke.

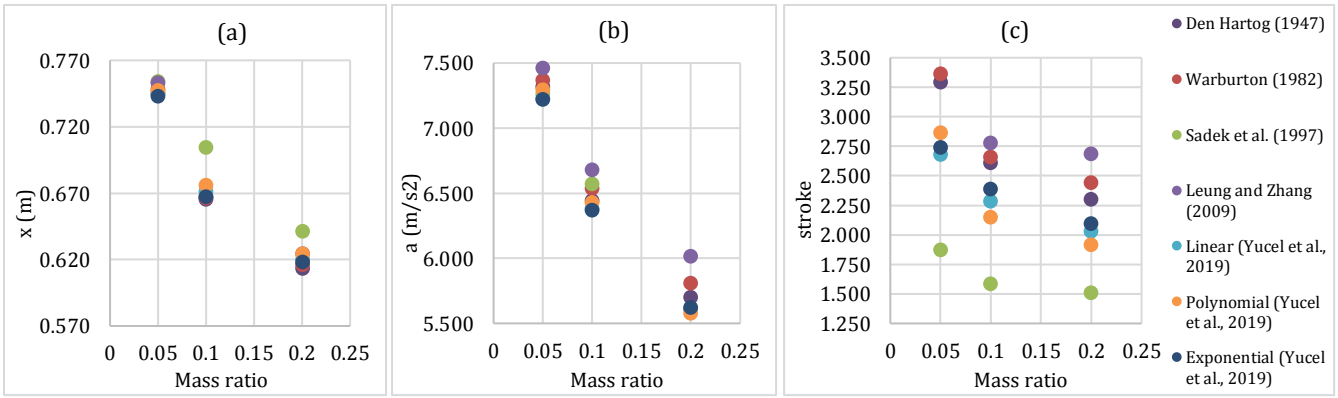

Fig. 6. The numerical results (Case 3): (a) x (m); (b) a (m/s²); (c) stroke.

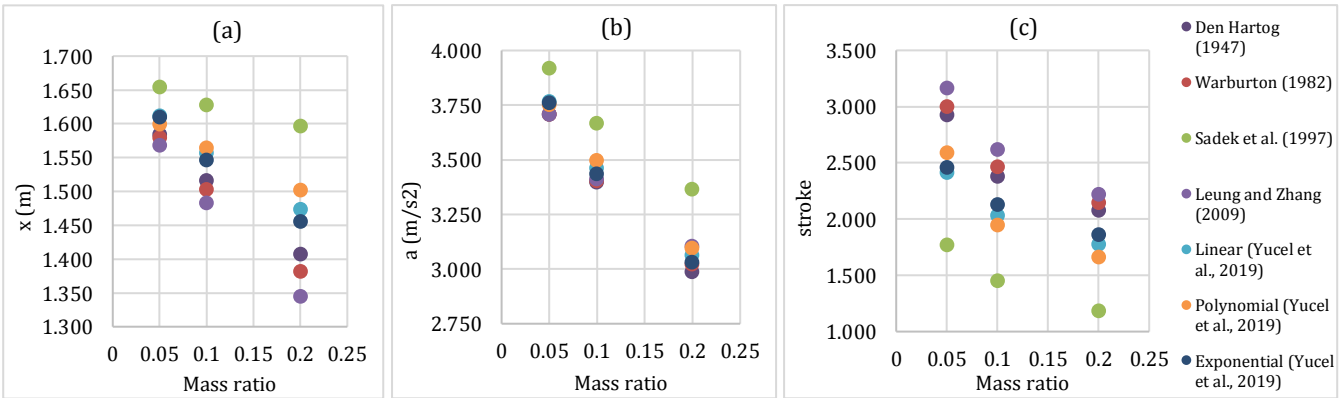

Fig. 7. The numerical results (Case 4): (a) x (m); (b) a (m/s²); (c) stroke.

4. Conclusions

In general, the ANN-based formulations are more effective than all formulations (except of Sadek et al. (1997)). When the optimum damping ratios of TMDs are investigated, Sadek et al. (1997) have a very big optimum value comparing to ANN-based method. Thus, the optimum TMD designed according to Sadek et al. (1997) have a high cost. By the increase of the damping, control can be provided with a small stroke value. The ANN-based methods have also small stroke values comparing to the others. By the increase of mass ratio, the damping values are increasing, and the values of Sadek et al. (1997) (4.5%) may need a high cost design. The effectiveness of the ANN-based formulations can be best seen in average results of response under different excitations.

While ANN-based methods (Yucel et al., 2019) and Sadek et al. (1997) are the best in reduction of maximum responses, the classical methods like Den Hartog and Warburton may be more effective for long period structures. For the same cases of 4s period SDOF structure, the best method is PSO-based formulations (Leung and Zhang, 2009).

In total, the ANN-based method provides comparative solutions with a feasible TMD design. The success of optimum values is both seen for the displacement and the acceleration values. By the increase of the mass ratio, a small advantage of the exponential equations can be seen, while all three types have similar performances.

Appendix

Table 6. The numerical values (Case 1).

		SDOF without TMD	Den Hartog (1947)	Warburton (1982)	Sadek et al. (1997)	Leung and Zhang (2009)	Linear (Yucel et al., 2019)	Polynomial (Yucel et al., 2019)	Exponential (Yucel et al., 2019)
					μ=0.05				
	T_d (s)		0.525	0.532	0.531	0.547	0.518	0.528	0.517
	ξ_d (%)		10.911	10.981	26.584	10.914	15.187	14.351	14.512
Critical	x (m)	0.124	0.116	0.116	0.114	0.116	0.115	0.115	0.115
	a (m/s²)	19.761	17.391	17.426	17.077	17.492	17.224	17.295	17.233
	stroke		3.076	3.185	1.972	3.457	2.499	2.702	2.544
Mean	x (m)	0.051	0.048	0.048	0.049	0.048	0.048	0.048	0.048
	a (m/s²)	8.119	7.280	7.284	7.314	7.308	7.268	7.272	7.267
	stroke		2.380	2.428	1.540	2.543	1.999	2.124	2.033
					μ=0.10				
	T_d (s)		0.550	0.564	0.558	0.587	0.536	0.543	0.537
	ξ_d (%)		15.076	15.273	34.697	15.140	18.023	20.315	16.741
Critical	x (m)	0.124	0.120	0.120	0.118	0.119	0.120	0.119	0.120
	a (m/s²)	19.761	17.169	17.158	16.844	17.133	17.073	17.026	17.109
	stroke		2.806	2.924	1.821	3.130	2.446	2.345	2.542
Mean	x (m)	0.051	0.048	0.048	0.049	0.047	0.049	0.048	0.049
	a (m/s²)	8.119	6.891	6.896	7.010	6.911	6.886	6.889	6.885
	stroke		2.025	2.094	1.357	2.216	1.800	1.733	1.863
					μ=0.20				
	T_d (s)		0.600	0.632	0.613	0.695	0.576	0.564	0.578
	ξ_d (%)		20.412	20.972	44.991	20.707	23.696	24.842	22.277
Critical	x (m)	0.124	0.124	0.123	0.126	0.120	0.126	0.127	0.126
	a (m/s²)	19.761	16.234	16.211	16.378	16.212	16.284	16.308	16.273
	stroke		2.636	2.787	1.710	3.054	2.321	2.198	2.402
Mean	x (m)	0.051	0.049	0.047	0.050	0.046	0.050	0.050	0.049
	a (m/s²)	8.119	6.326	6.317	6.585	6.382	6.369	6.405	6.360
	stroke		1.841	1.945	1.253	2.170	1.627	1.545	1.682

Table 7. The numerical values (Case 2).

		SDOF without TMD	Den Hartog (1947)	Warburton (1982)	Sadek et al. (1997)	Leung and Zhang (2009)	Linear (Yucel et al., 2019)	Polynomial (Yucel et al., 2019)	Exponential (Yucel et al., 2019)
					μ=0.05				
	T_d (s)		1.050	1.063	1.062	1.093	1.037	1.057	1.034
	ξ_d (%)		10.911	10.981	26.584	10.914	15.187	14.351	14.512
Critical	x (m)	0.454	0.404	0.404	0.420	0.403	0.410	0.408	0.409
	a (m/s²)	17.987	15.466	15.510	15.915	15.604	15.560	15.582	15.532
	stroke		2.878	2.959	1.821	3.149	2.368	2.543	2.414
Mean	x (m)	0.165	0.142	0.142	0.150	0.141	0.145	0.144	0.145
	a (m/s²)	6.553	5.448	5.457	5.684	5.490	5.512	5.506	5.500
	stroke		2.297	2.326	1.468	2.402	1.940	2.044	1.976
					μ=0.10				
	T_d (s)		1.100	1.129	1.117	1.174	1.073	1.086	1.073
	ξ_d (%)		15.076	15.273	34.697	15.140	18.023	20.315	16.741
Critical	x (m)	0.454	0.393	0.393	0.400	0.392	0.395	0.396	0.394
	a (m/s²)	17.987	14.630	14.675	14.687	14.744	14.590	14.614	14.589
	stroke		2.524	2.618	1.573	2.770	2.217	2.132	2.299
Mean	x (m)	0.165	0.139	0.138	0.144	0.137	0.141	0.141	0.140
	a (m/s²)	6.553	5.138	5.142	5.283	5.182	5.146	5.154	5.142
	stroke		1.814	1.855	1.201	1.932	1.622	1.555	1.680
					μ=0.20				
	T_d (s)		1.200	1.265	1.225	1.389	1.152	1.128	1.157
	ξ_d (%)		20.412	20.972	44.991	20.707	23.696	24.842	22.277
Critical	x (m)	0.454	0.382	0.380	0.398	0.377	0.387	0.389	0.385
	a (m/s²)	17.987	13.520	13.654	13.620	13.899	13.425	13.384	13.430
	stroke		2.054	2.188	1.567	2.502	1.882	1.812	1.948
Mean	x (m)	0.165	0.136	0.134	0.142	0.133	0.138	0.139	0.138
	a (m/s²)	6.553	4.756	4.786	4.849	4.882	4.731	4.731	4.731
	stroke		1.519	1.587	1.041	1.746	1.354	1.290	1.400

Table 8. The numerical values (Case 3).

		SDOF without TMD	Den Hartog (1947)	Warburton (1982)	Sadek et al. (1997)	Leung and Zhang (2009)	Linear (Yucel et al., 2019)	Polynomial (Yucel et al., 2019)	Exponential (Yucel et al., 2019)
					μ=0.05				
	T_d (s)		2.100	2.127	2.123	2.186	2.074	2.114	2.068
	ξ_d (%)		10.911	10.981	26.584	10.914	15.187	14.351	14.512
Critical	x (m)	0.830	0.745	0.748	0.754	0.753	0.744	0.747	0.743
	a (m/s²)	8.237	7.316	7.364	7.258	7.458	7.223	7.291	7.218
	stroke		3.291	3.362	1.872	3.524	2.678	2.861	2.737
Mean	x (m)	0.382	0.344	0.344	0.356	0.343	0.348	0.347	0.348
	a (m/s²)	3.788	3.303	3.311	3.392	3.329	3.325	3.327	3.320
	stroke		2.337	2.374	1.485	2.465	1.975	2.086	2.011
					μ=0.10				
	T_d (s)		2.200	2.257	2.234	2.349	2.145	2.173	2.147
	ξ_d (%)		15.076	15.273	34.697	15.140	18.023	20.315	16.741
Critical	x (m)	0.830	0.665	0.666	0.704	0.667	0.671	0.676	0.667
	a (m/s²)	8.237	6.442	6.533	6.571	6.677	6.376	6.427	6.369
	stroke		2.608	2.655	1.586	2.776	2.281	2.145	2.385
Mean	x (m)	0.382	0.328	0.327	0.346	0.325	0.333	0.335	0.331
	a (m/s²)	3.788	3.053	3.072	3.178	3.108	3.065	3.085	3.055
	stroke		1.902	1.950	1.253	2.045	1.692	1.627	1.755
					μ=0.20				
	T_d (s)		2.400	2.530	2.450	2.779	2.305	2.256	2.313
	ξ_d (%)		20.412	20.972	44.991	20.707	23.696	24.842	22.277
Critical	x (m)	0.830	0.613	0.616	0.641	0.624	0.620	0.624	0.618
	a (m/s²)	8.237	5.700	5.808	5.611	6.016	5.609	5.574	5.621
	stroke		2.301	2.442	1.508	2.685	2.026	1.917	2.094
Mean	x (m)	0.382	0.310	0.307	0.335	0.305	0.318	0.321	0.316
	a (m/s²)	3.788	2.751	2.798	2.877	2.893	2.741	2.742	2.735
	stroke		1.600	1.670	1.064	1.811	1.424	1.356	1.472

Table 9. The numerical values (Case 4).

		SDOF without TMD	Den Hartog (1947)	Warburton (1982)	Sadek et al. (1997)	Leung and Zhang (2009)	Linear (Yucel et al., 2019)	Polynomial (Yucel et al., 2019)	Exponential (Yucel et al., 2019)
					μ=0.05				
	T_d (s)		4.200	4.254	4.246	4.372	4.148	4.228	4.137
	ξ_d (%)		10.911	10.981	26.584	10.914	15.187	14.351	14.512
Critical	x (m)	1.936	1.585	1.580	1.655	1.569	1.612	1.600	1.610
	a (m/s²)	4.797	3.707	3.707	3.918	3.707	3.768	3.753	3.760
	stroke		2.928	2.999	1.770	3.165	2.415	2.589	2.461
Mean	x (m)	0.639	0.591	0.591	0.599	0.590	0.593	0.592	0.592
	a (m/s²)	1.591	1.448	1.450	1.450	1.454	1.444	1.447	1.443
	stroke		2.209	2.226	1.364	2.271	1.861	1.951	1.901
					μ=0.10				
	T_d (s)		4.400	4.514	4.467	4.698	4.291	4.346	4.294
	ξ_d (%)		15.076	15.273	34.697	15.140	18.023	20.315	16.741
Critical	x (m)	1.936	1.517	1.503	1.628	1.483	1.557	1.565	1.547
	a (m/s²)	4.797	3.399	3.403	3.667	3.412	3.462	3.496	3.437
	stroke		2.378	2.466	1.451	2.619	2.033	1.950	2.130
Mean	x (m)	0.639	0.571	0.570	0.582	0.570	0.573	0.574	0.573
	a (m/s²)	1.591	1.372	1.378	1.367	1.388	1.364	1.365	1.365
	stroke		1.710	1.732	1.080	1.781	1.535	1.461	1.593
					μ=0.20				
	T_d (s)		4.800	5.060	4.900	5.558	4.609	4.513	4.627
	ξ_d (%)		20.412	20.972	44.991	20.707	23.696	24.842	22.277
Critical	x (m)	1.936	1.408	1.382	1.597	1.345	1.474	1.502	1.456
	a (m/s²)	4.797	2.989	3.023	3.366	3.104	3.065	3.097	3.033
	stroke		2.077	2.148	1.185	2.218	1.775	1.662	1.863
Mean	x (m)	0.639	0.542	0.540	0.563	0.537	0.548	0.551	0.546
	a (m/s²)	1.591	1.264	1.276	1.252	1.302	1.251	1.246	1.253
	stroke		1.329	1.358	0.859	1.423	1.194	1.142	1.236

Publication Note

This research has previously been presented at the 6th International Conference on Harmony Search, Soft Computing and Applications (ICHSA 2020) held in İstanbul, Turkey, on July 16-17, 2020. Extended version of the research has been submitted to Challenge Journal of Structural Mechanics and has been peer-reviewed prior to the publication.

References

Arfiadi Y (2016). Reducing response of structures by using optimum composite tuned mass dampers. *Procedia Engineering*, 161, 67–72.

Bekdaş G, Kayabekir AE, Nigdeli SM, Toklu YC (2019). Tranfer function amplitude minimization for structures with tuned mass dampers considering soil-structure interaction. *Soil Dynamics and Earthquake Engineering*, 116, 552–562.

Bekdaş G, Nigdeli SM (2011). Estimating optimum parameters of tuned mass dampers using harmony search. *Engineering Structures*, 33, 2716–2723.

Bekdaş G, Nigdeli SM, Yang XS (2017). Metaheuristic based optimization for tuned mass dampers using frequency domain responses. *International Conference on Harmony Search Algorithm,* Singapore, 271–279.

Bekdaş G, Nigdeli SM, Yang XS (2018). A novel bat algorithm based optimum tuning of mass dampers for improving the seismic safety of structures. *Engineering Structures*, 159, 89–98.

Den Hartog JP (1947). Mechanical Vibrations. 3rd ed., McGraw-Hill, New York, USA.

Etedali S, Mollayi N (2018). Cuckoo search-based least squares support vector machine models for optimum tuning of tuned mass dampers. *International Journal of Structural Stability and Dynamics*, 18(2), 1850028.

Farshidianfar A, Soheili S (2013). ABC optimization of TMD parameters for tall buildings with soil structure interaction. *Interaction and Multiscale Mechanics*, 6(4), 339–356.

FEMA P-695 (2009). Quantification of Building Seismic Performance Factors. Federal Emergency Management Agency, Washington DC, USA.

Khatibinia M, Gholami H, Kamgar R (2018). Optimal design of tuned mass dampers subjected to continuous stationary critical excitation. *International Journal of Dynamics and Control*, 6(3), 1094–1104.

Khatibinia M, Gholami H, Labbafi SF (2016). Multi–objective optimization of tuned mass dampers considering soil–structure interaction. *Iran University of Science & Technology*, 6(4), 595–610.

Leung AYT, Zhang H (2008). Particle swarm optimization of tuned mass dampers. *Engineering Structures*, 31(3), 715–728.

Mohebbi M, Shakeri K, Ghanbarpour Y, Majzoub H (2013). Designing optimal multiple tuned mass dampers using genetic algorithms (GAs) for mitigating the seismic response of structures. *Journal of Vibration and Control*, 19(4), 605–625.

Nigdeli SM, Bekdaş G (2017). Optimum tuned mass damper design in frequency domain for structures. *KSCE Journal of Civil Engineering*, 21(3), 912–922.

Pourzeynali S, Salimi S, Kalesar HE (2013). Robust multi-objective optimization design of TMD control device to reduce tall building responses against earthquake excitations using genetic algorithms. *Scientia Iranica*, 20 (2), 207–221.

Sadek F, Mohraz B, Taylor AW, Chung RM (1997). A method of estimating the parameters of tuned mass dampers for seismic applications. *Earthquake Engineering and Structural Dynamics*, 26, 617–635.

Steward JP, Chiou S, Bray JD, Graves RW, Somerville PG, Abrahamson NA (2001). Ground Motion Evalution Procedures for Performance-Based Design. Pacific Earthquake Engineering Research Center. Report 2001/09; September 2001.

Viana FAC, Kotinda GI, Rade DA, Steffen JV (2008). Tuning dynamic vibration absorbers by using ant colony optimization. *Computers & Structures*, 86(13-14), 1539–1549.

Warburton GB (1982). Optimum absorber parameters for various combinations of response and excitation parameters. *Earthquake Engineering and Structural Dynamics*, 10, 381–401.

Yang XS (2012). Flower pollination algorithm for global optimization. *Unconventional Computation and Natural Computation,* 240–249.

Yang Y, Li C (2016). Performance of tuned tandem mass dampers for structures under the ground acceleration. *Structural Control and Health Monitoring*, 24(10), e1974.

Yucel M, Bekdaş G, Nigdeli SM, Sevgen S (2019). Estimation of optimum tuned mass damper parameters via machine learning. *Journal of Building Engineering*, 26, 100847.

Challenge Journal of Structural Mechanics

Research Article

Strengthening and performance assessing historical cinema hall balcony according to new Turkish Earthquake Code

Memduh Karalar [a,*], Murat Çavuşli [a]

[a] *Department of Civil Engineering, Zonguldak Bülent Ecevit University, İncivez, 67100 Zonguldak, Turkey*

ABSTRACT

Strengthening historical buildings and evaluating their performances make great contributions to both the history of the country and the tourism of the country. In this study, performance analysis and evaluations of the historical cinema hall balcony, which was built in 1933 by a French company and served to Zonguldak province for a long time, are presented in detail. This cinema hall was frequently used by local people between 1933 and 1999 and hosted many Yeşilçam movies. Firstly, examinations were performed in the historical cinema hall and the areas (columns, beams and floors) that were damaged in time were identified. According to the obtained information, it was determined that there were significant damages in the carrier system of the building and there were visible cracks and damages in the columns of the cinema hall. It was also observed that explosions occurred in one of the main carrier columns of the balcony. After the core samples taken from the balcony were tested in the laboratory, the current status of the carrier elements and reinforcements were determined with the help of an x-ray rebar scanner. After all these processes, the structure was modeled as three dimensional (3D) using a special computer program and performance evaluations were performed regarding the current state of the structure. As a result of the performance evaluation, it was determined that the balcony of the historical cinema hall could not survive anymore and would collapse over time. It was concluded that there were great damages especially on the balcony columns and a reinforcement should be made on a total of 6 columns. Strengthening was made to 4 different main columns and a performance analysis was performed again in strengthened structure. After strengthening, it was understood that the columns of the balcony of the cinema hall could survive for a long time.

ARTICLE INFO

Article history:
Received 28 July 2020
Revised 23 October 2020
Accepted 17 November 2020

Keywords:
Structural strengthening
Performance evaluation
Deflection evaluation
Column end force
Turkish Earthquake Code

1. Introduction

Turkey has a very ancient history and many empires that have witnessed this history have left deep traces and historical heritages in this country. It is seen that there are many building types in this historical heritage, from wooden structures with excellent architecture to reinforced concrete structures built thousands of years ago. The protection and reuse of these historical buildings make great contributions to the economy and tourism of our country. Nowadays, studies on the protection of historical buildings have become widespread. The main purpose of strengthening and preserving historical constructions is to ensure surviving of these structures for a long time. However, while performing these vital operations, it should be essential to keep the historical texture of the historical building. Recently, historical structures in Turkey are faced with strong ground movements such as earthquakes, floods and negative threats of rapid urbanization that has occurred.

While Turkey can protect the large-scale public structures, small-scale structures, most of which are privately owned, cannot adequately protect due to the lack of legal infrastructure. For this reason, many historical buildings

* *Corresponding author*. Tel.: +90-372-291-2582 ; Fax: +90-372-257-4023 ; E-mail address: memduhkaralar@beun.edu.tr (M. Karalar)
ISSN: 2149-8024 / DOI: https://doi.org/10.20528/cjsmec.2021.01.004

have been demolished recently. However, these structures could have been used for both local people and country tourism for a long time by performing earthquake evaluation of structures. The strength of a historical building depends on the structural system, the geometry of the building and the mechanical properties of building. For this reason, different structural deformations and defeats can occur under constant loads in similar historical buildings. The main causes of the defeats in historical buildings are the loads caused by the building's own weight, loads caused by ground vibrations and other natural disasters. However, it is very rare situation that a historical building destroyed or damaged due to its own weight. The main reason for the damage or demolition of historical buildings are natural external loads, man-made artificial loads or structural problems due to other environmental effects (Örmecioğlu, 2010). In the literature, the studies on the strengthening and reuse of historical structures are summarized as follows: In a study, it has been performed strengthening of the walls, domes, vaults and foundations with injection resins and anchorage systems. In this study, it is stated that the compressive and shear strength of resins are very high. Moreover, it was observed that the reaction time of said resins ranged from 30 to 180 seconds. It has been stated that Carbopur WF resin does not swell voluntarily in anhydrous environment and its compressive strength reaches around 800 kg/cm2 in a few minutes. It is stated that Carbopur S resin swells 100-200% in anhydrous environment and its compressive strength is around 100-300 kg/cm2 in a few minutes. It is shown that two component resins have swelling and foaming rate of 2-6 in free environments (such as direct contact with air). However, it is stated that their swelling rates in environments such as concrete and ground are between 1.0-2.5. The tensile, torsional and compressive strengths of these resins have been proved to be very high (Kasapgil, 2007). In addition, the strengthening was carried out in Adana Ulucami minaret in 2007. Separated and broken stones and cracks in Adana Ulucami Tower are filled with resins that adhere well. With this filling process, the stones are prevented from cracking due to expansion, water leaking into the cracks, washing the material inside and expanding the cracks (Kasapgil, 2007). Later, a study was carried out on the repair and strengthening of the Ahi Celebi Mosque. In this study, the repair and strengthening methods of masonry domes damaged due to effects such as vertical loads, support collapse, earthquake, and the effectiveness of the pull circle formed in the support area are given with the application example of Ahi Çelebi Mosque. The structure is modeled using SAP2000 software under the influence of vertical and earthquake loads. The application of the pull-out circle led to a significant reduction in the tensile stresses formed in the dome (Sesigür and Çelik, 2007). In addition, a building was proposed to be demolished and reconstructed by technical teams. The building is located only 7.5 km from the Arifiye fault zone torn in the 1999 East Marmara Earthquake. As a result of this study, a strengthening and repair project of the building was made and the building was opened eight months after the earthquake. The behavior curve of the structure (bottom shear force - peak displacement) remained at the “immediate use” level (Arioglu et al., 2007). Moreover, a study on the pre-fire condition of Urla Old Monopoly Building (Arditi Pavilion) and the strengthening of the building was carried out. Although the outer walls of the building were standing before the fire, it was determined that there were collapses and decays in the building (Aydın et al., 2015). In a study, structural analyses were carried out within the scope of restorations of historical bridges and their results are presented in detail. It has been proved that in cases where the said research is not done / insufficient, the damage can occur again after the restoration. It has been stated that the determinations related to the building and the ground are important in terms of supporting the carrier systems of the historical bridges (Sert and Partal, 2015). The dynamic behavior of the scaled stone arch bridge model was examined experimentally and analytically. In this study, the dynamic behavior of the 1/10 scale model of a stone arch bridge, which is frequently encountered in applications, was investigated experimentally. The first six frequencies, mode shape and modal damping rate of the model, which was carried out using the environmental vibration test, were determined. In order not to damage the model during the measurement, the bridge behavior was determined with uniaxial seismic accelerometers under the vibrations coming from the environment without using additional vibrators. Dynamic characteristics were determined analytically by performing modal analysis on the model created using three-dimensional solid elements in the SAP2000 program. At the end of the study, experimental dynamic characteristics and analytical results were compared and differences were revealed (Türker et al., 2015). Then, a study was presented the restoration-conservation of historical Malabadi Bridge. Restoration-conservation carried out by the General Directorate of Highways between 2009-2013 on the Historical Malabadi Bridge, which was built in the Artuqid Period on the Batman Water in Diyarbakır province (Sert and Yılmaz, 2015). Linear and nonlinear seismic analyzes of the historical Tağar Bridge on Tağar stream in Çemişgezek district of Tunceli province were performed. For this purpose, the bridge is modeled with three dimensional finite elements. Acceleration records of the Erzincan earthquake were considered as seismic effects. ANSYS finite element program was used in the analysis (Onat and Sayın, 2015). A study has been carried out on structural system features, damages, repair and strengthening techniques in historical buildings. In the study, information is given about how the concept of protection is perceived from past to present and what steps are taken, types of historical buildings, materials and properties used in historical buildings. In addition, detailed information about carrier system constituting the historical structure, damages occurring in these structures and damage determination methods applied today, the examination of earthquake safety within the framework of the conditions specified in the earthquake regulation of masonry buildings and the repair and strengthening techniques applied in historical buildings are presented (Mahrebel, 2006). In another study, seismic performance evaluation of a historical wall structure

was performed. The building performance was made by comparing the old and new Turkish earthquake standards. Non-destructive experimental measurement methods have been used to obtain reliable results in seismic performance evaluation. As a result of the analyzes, maximum displacements and basic stresses were obtained. In terms of displacement control, the structure showed only limited damage during the earthquake recording applied. In other word, the building behaved linearly when it was exposed to the selected earthquake (Günaydın, 2019). New Zealand is a country famous for its historical structures and the protection of the historical texture is vital for this country. In a study, performance assessment of historical buildings in a city in New Zealand was made. Using the MCDA methodology, the performance of historical buildings was revealed and suggestions were made (Aigwi et al., 2019). Performance-based assessment has recently become crucial for multi-story, non-reinforced walled buildings. However, it is very difficult to evaluate the performance of multi-storey historical buildings due to their complex engineering features and structural performances. In a study, the historical scribe school in Erzurum was selected for performance analysis, and the seismic weaknesses of this historical building were identified and its structural performance was evaluated (Korkmaz et al., 2018). It is vital to protect the historical heritage against horizontal loads (such as earthquakes) and to examine these structures in three dimensions. In a study, the earthquake performance of three different damaged palace walls in Mantua (Northern Italy) after the 2012 Emilia earthquake was investigated. Three different palace structures are modeled in three dimensions and the material parameters are laid out in detail. Comparison between three-dimensional numerical results and damage research has shown that the numerical approach used in this study may be an adequate tool to accurately assess the seismic response of historic structures (Valente and Milani, 2019). In the construction of historical buildings, only static loads are generally taken into account. Therefore, these structures can be damaged or destroyed due to seismic effects. Earthquake performances of historical buildings should be obtained in order to move them to the future and protect them. In a study, the nonlinear seismic responses of the Malabadi Bridge built in the 12th century were evaluated. To determine the material properties of the bridge, uniaxial compressive strength tests, ultrasound tests, Schmidt hammer tests and mass loss tests were performed. It was observed that there was no damage zone on the arches and spandrel walls under D1 and D2 earthquake loads and plastic deformations occurred in the filling material under D2 earthquake loads. Numerical results showed that the main arch of the bridge was heavily damaged under the earthquake load D3 (Karaton et al., 2017). Historical buildings are often vulnerable to earthquake damage throughout their lifetimes, and strengthening is needed to survive these structures. This strengthening process is handled through analysis considering the current state of the buildings. However, there are few studies focusing on the strengthening methods applied. In a study, the structural behavior of conditions before and after the strengthening of a historical structure was investigated. In order to compare the conditions, theoretical finite element models were developed and then experimental analysis of the historical building was performed. The results show that the strength of the reinforced structure increased 3 times compared to the initial state (Ercan, 2018). In another study, in the east of Turkey on October 23, 2015 during the main shock of the Van earthquake damage in two historic buildings partially collapsed was investigated. The solid body of both structures survived without earthquake damage, but the Narthex of both structures collapsed. First, the existing standards (ASCE 41, 2006; EC8-3, 2005; PERPETUATE, 2010) were extensively studied. Then, response spectrum analyzes were performed to evaluate the seismic performance of the structures. According to the results of the numerical analysis, the causes of the collapse of the building were revealed (Cakir et al., 2015). Finally, in a study, an algorithm was developed to determine the failure loads of single span circular masonry arch bridges according to the lower-limit theorem of limit analysis. The algorithm uses linear programming techniques and converges at the bottom of the true burden load value, that is, on the safe side. The algorithm is programmed in Matlab environment (Orhan and Özyazıcıoğlu 2015).

As can be seen from the studies in the literature, there are many studies on historical structures in the past. However, there is no study on the strengthening of movie theaters, which are important for tourism and a place frequently used by the public, by taking into consideration the 2018 Turkish earthquake regulation and earthquake performance. The aim of this study is to perform earthquake strengthening and to evaluate the earthquake performances in order to survive of the historical movie theater, which is important for the country's tourism, for a long time. For this purpose, the historical cinema hall built in 1933 was selected for analysis and evaluations. This movie theater is very important for Zonguldak and our country's tourism and it is vital to extend the life of this building. For this reason, this study contributes significantly to the literature and country tourism.

2. Material and Method

In this study, the incremental single-mode push (pushover) analysis method was used for performance evaluations. This method impacts the calculated horizontal loads on the system, taking into account a predetermined distribution. The structure is increased step by step up to a certain limit value with these imposed loads and the carrier system elements are brought to capacity. This limit value can occur in two ways. It occurs when the lateral stability of the carrier system is degraded or the horizontal displacement value that brings the structure to the mechanism state is reached. In incremental single-mode propulsion analysis, in each step, internal forces, displacements and plastic deformations in the carrier system elements are calculated. Accordingly, the curve that gives the relationship between the base shear force and the peak displacement of the structure, that is, the pushover curve, is determined. In addition, building

performance evaluations have been performed considering the 2018 Turkish New Earthquake Regulation. In the current status of the building, there are major damages and explosion in the balcony columns. In addition, there are deflections in the existing balcony beams. Most of the balcony flooring reinforcements have come out and are corroded. In this study, first of all, the relievo of the historical movie theater was obtained in detail. Because this building is a historical monument building, no project or technical knowledge of this structure was available. Each carrier element is determined in detail and the length information of each carrier is entered in detail in the AUTOCAD program. Due to the fact that the balcony flooring is inclined and variable thickness, very sensitive measurement has been taken and sensitivity has been shown while removing the leveling. Then, information was obtained about the current status of the fittings in the carrier elements using an x-ray device. Concrete X-ray scanning has been in use for a long time in the construction industry due to its accuracy. By using this device, information was obtained about the current state of the reinforcements in the concrete and it was observed that most of the reinforcement was corroded. 3D model of the building, which was removed, was created with the help of the IDECAD static program. IDECAD program is used finite element method while 3D modelling and 3D analyzing of structures. All carrier elements are carefully entered into the program and balcony flooring has been created in accordance with the project. Finally, core samples were taken from bearing columns supporting the balcony flooring, bearing beams and flooring. While taking the core sample, due to the historical feature of the building, care was taken not to damage the building too much. Moreover, while testing cylinder samples, initial speed, dimensions (diameter, height) defined to device. Core samples were experimentally pressure tested and their mechanical properties were determined. After the concrete samples were tested in the test device, information about the current concrete quality in the structure was acquired. The material parameters of all carriers are carefully determined to program. Young's modulus, Poisson ratio, shear modulus is defined to IDECAD program to obtain more realistic analysis results of structure. In addition, the structure is divided into equal parts and mesh process has been made. During the meshing process, all the elements of the structure are divided into equal pieces of approximately 10 cm. The analyzes were first made by considering the current state of the building. Balcony columns and beams were evaluated for G+Q+E (X and Y) combinations according to 2018 earth-quake regulation. These standard combinations were used to obtain the most critical condition of the historical building during the earthquake. These combinations show the situation in which the structure receives the greatest moment and shear forces. Therefore, these combinations were used in this study. According to the results of the analysis, it was observed that the building had more difficulty in surviving and that earthquake reinforcement was essential. The carrier elements that need reinforcement were determined by examining the results in detail and reinforcement jacketing was performed on these carrier walls. During jacketing, care was taken not to damage the historical building too much. When the reinforced structure was analyzed again, it was seen that the cinema hall could remain standing for many years as a result of the jacketing, and the building was provided to contribute to the tourism and national economy for many years.

3. General Information about Historical Cinema Hall

After the proclamation of the republic, Zonguldak province became a province where large investments were made in tourism and economy. As a result of the investment of businessmen, Zonguldak has become one of the provinces with the highest population in Turkey. The historical cinema hall, which is the subject of this study, was built in Zonguldak Center after the proclamation of the Republic in 1933 and served as a community center for the tourism of our country and the people of Zonguldak for a very long time. The building, which served as a community center until 1951, continued to serve as a cinema and theater hall after 1951. This historical structure is one of the largest historical heritages left to Zonguldak after the proclamation of the Republic (Fig. 1).

Fig. 1. Views of Zonguldak historical theater hall (1965).

After 1951, many Yeşilçam artists watched films in this building and thousands of films were screened. At that time, what movies were on display (cowboy movies, adventure movies, crime) were first seen in this cinema. Even the 1974 world cup documentary was released in this cinema. But over time, the effectiveness of the population of the province of Zonguldak institutions were put dwindled, Turkey's most populous cities in between is between the least populated provinces. For this reason, interest in tourism and cultural events has decreased over time and these historical cinema structures have been abandoned to their fate. In 2013, this building was completely closed and local people were deprived of the cinema viewing activity in this historical building.

4. Material Parameters of Historical Cinema Hall and Modeling Three Dimensions

Since 1933, no interference (strengthening) has been carried on the carriers of the historical movie theater subject to this study. For this reason, it has been determined that the building is sufficiently tired and the modification of the structure is needed in order to survive longer. This structure is a reinforced concrete structure and the using of ribbed reinforcement in the building in 1933 is an indicator of the value given to the buildings and people at that time. In the building, there are beams with a thickness of about 1 meter and all of their floors are made of reinforced concrete. The lowest floor is the ground floor and at that time this floor was used as an entrance to the cinema and the place where the stage was placed. Ground floor and first floor plans are the same. But the slope of the balcony flooring on the 1st floor is very different from the ground floor. 1st floor balcony floor has 12% slope. The plans of the building before and after strengthening are presented in Figs. 2 and 3.

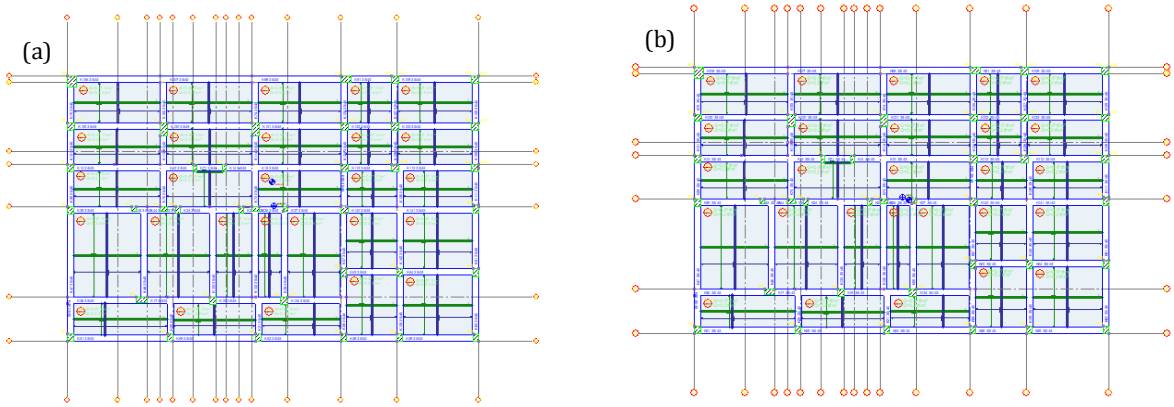

Fig. 2. Structure plan before reinforcement: (a) Ground floor; (b) 1st floor.

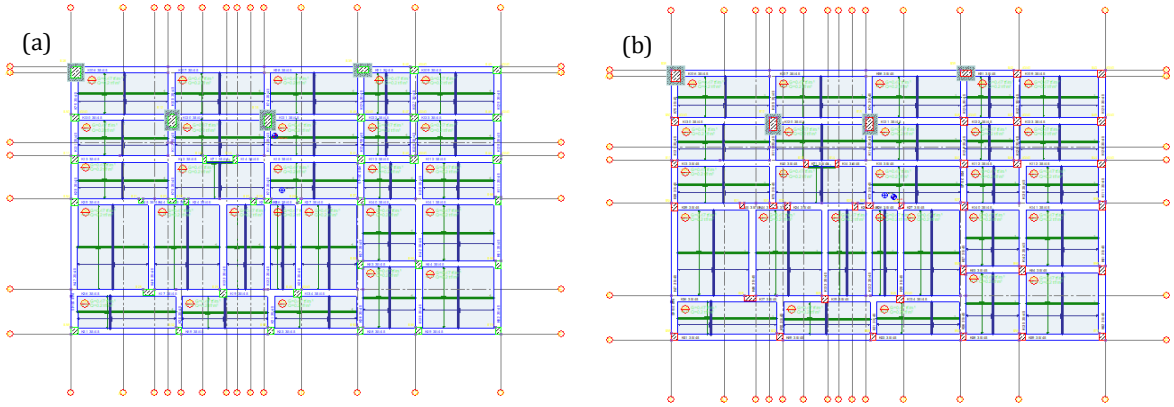

Fig. 3. Structure plan after reinforcement: (a) Ground floor; (b) 1st floor.

In this study, core samples were taken from the carrier elements of the building and the balcony floor. Due to the fact that the building is a historical building, care was taken not to damage the historical artifact while taking the core sample. Three samples were taken from each carrier and these samples were subjected to pressure testing in the laboratory (Fig. 4). According to the pressure test results, in some of the balcony main columns (S39, S40, S41, S42), concrete class has been determined as C14 and all other carriers have been determined as concrete class C18. Then all the carrier elements were scanned with an x-ray device and the current state of the reinforcements in it was determined (Fig. 5). It was determined that most of the reinforcements were corroded and it was observed that melts and explosions occurred in the reinforcements over time in both main bearing columns of the balcony. After all these operations were done, all geometric and mechanical properties of the building were entered into the IDECAD static program. First, the current state of the building was modeled, and after analyzing, some damaged parts of the building were reinforced. The existing modeled and reinforced state of the building are presented in Figs. 6 and 7. Moreover, moment-rotation relationship was obtained for main column (S41) of balcony of historical structure by using XTRACT program (Fig. 8). Finally, a performance objective may include consideration of damage states for several levels of ground motion and would then be termed a dual or multiple-level performance objective. Based on performance objective the capacity and demand curve is drawn and based on it the suitable design is chosen for 3D analyses (Fig. 9). Moreover, jacketing detail of S41 column is shown in Fig. 10.

Fig. 4. Core samples taken from the structure:
(a) Main column S41; (b) Main column S42; (c) Balcony flooring.

Fig. 5. Examination of carrier elements with X-ray device.

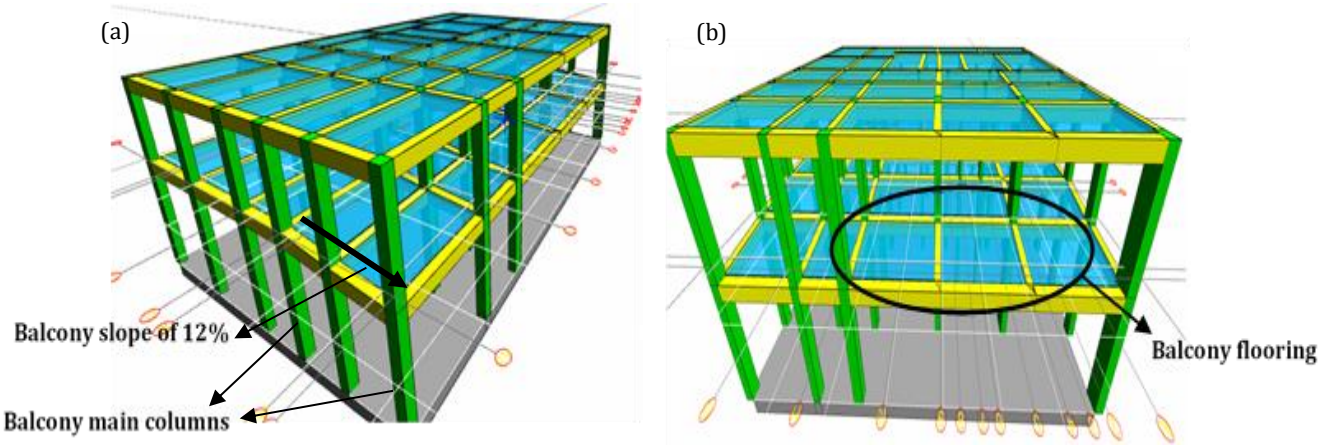

Fig. 6. Three-dimensional view of the building before reinforcement: (a) Right view; (b) Front view.

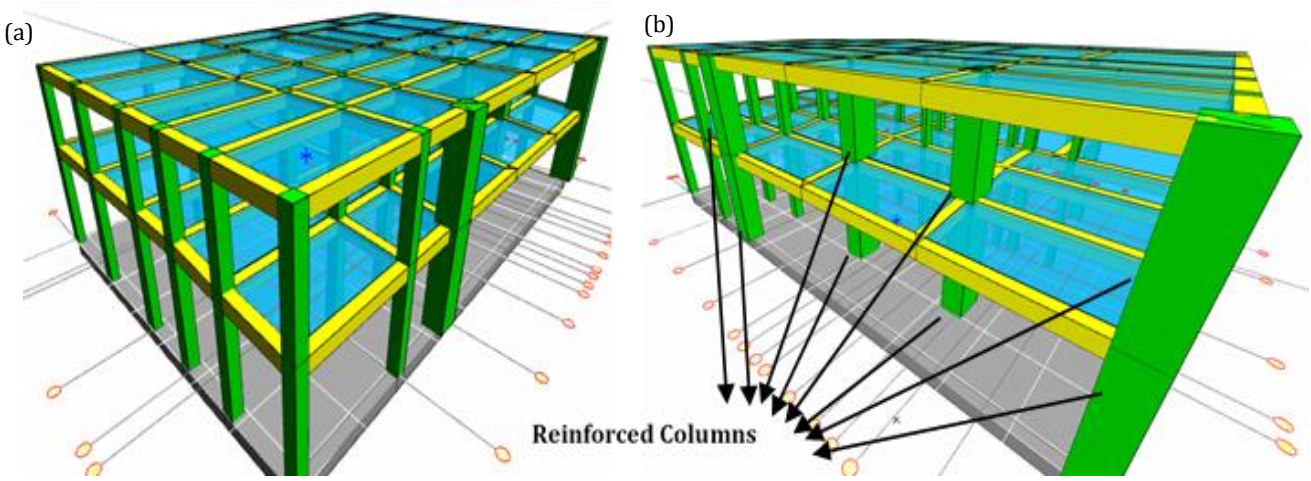

Fig. 7. Three-dimensional view of the building after reinforcement: (a) Right view; (b) Left view.

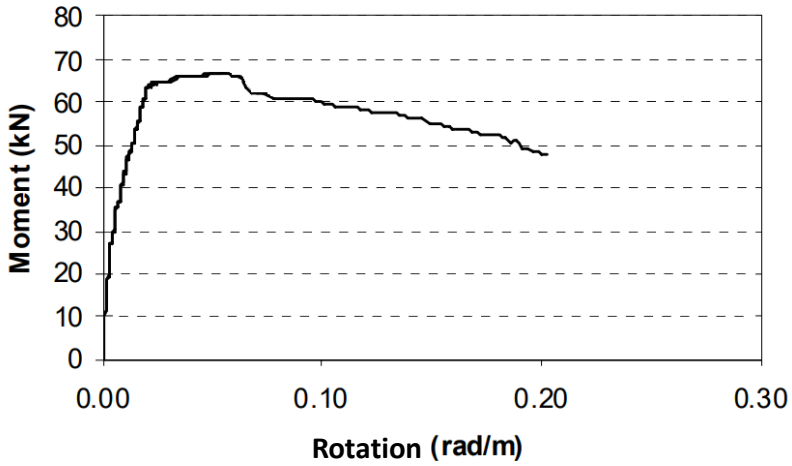

Fig. 8. Moment-rotation relationship for main column of balcony of RC structure.

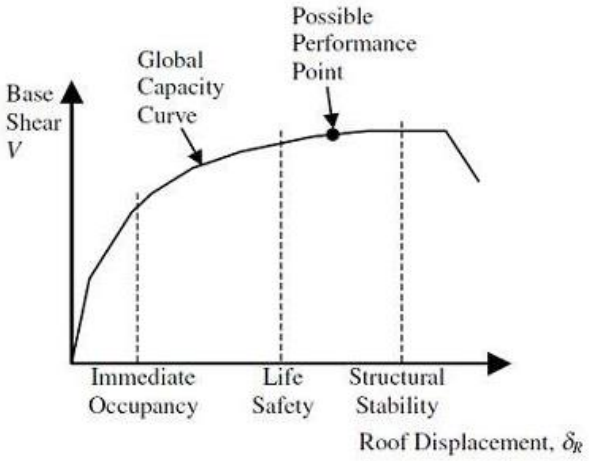

Fig. 9. Capacity curve of structure.

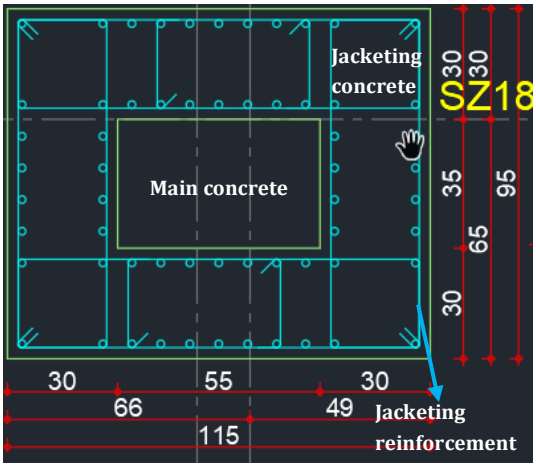

Fig. 10. Jacketing detail of S41 column.

5. Results and Discussions

In this section, the before and after conditions of Zonguldak historical movie theater balcony are evaluated and compared with each other. Firstly, the current situation of the building is taken into consideration and a performance evaluation is performed for current situation of building. As a result of this evaluation, damaged carrier elements of the building were identified. According to the results of the analysis, it was seen that damages occurred on the balcony floor and columns and it was thought that this balcony could be demolished in a

short time. The carrier elements detected later were reinforced with jacketing. A total of 4 columns on the ground floor and 4 columns on the first floor were jacketed. The jacket thickness is 20 cm and C25 concrete was used when jacketing. A total of 4 columns and 3 balcony beams were examined both before and after reinforcement and presented in this section. These columns and beams are presented in Fig. 11. In this study, balcony columns and beams were evaluated for G+Q+E (X and Y) combinations according to 2018 earthquake regulation. These standard combinations were used to obtain the most critical condition of the historical building during the earthquake. These combinations show the situation in which the structure receives the greatest moment and shear forces. Therefore, these combinations were used in this study.

5.1. Analysis results for the current situation of the building

Analysis results for damaged columns and beams of Zonguldak historical movie theater balcony are presented in this section as table and graphically. Identified balcony columns were named as S39, S40, S41 and S42. In addition, the weak balcony beams are named as KZ1, KZ2 and KZ3 (Fig. 11). According to the G+Q+E (X and Y) combination, the loads occurred on the existing columns and beams of the building are given in Tables 1-7. Besides, force charts for reinforced situation of this structure are presented in Tables 8-14. In Table 1, the end forces of S40 column for 8 different load combinations are shown in detail. When these forces are examined, the maximum normal force in *i* direction is -21.7 kN and this force was obtained in G + Q + EY combination. Moreover, the maximum normal force in *j* direction is 18.5 kN. When the largest shear forces occurred in S40 column are examined, the largest shear force obtained in *i* direction is 3.87 kN. When the largest shear forces in *j* direction are examined, it is observed that 4.44 kN occurred for G+Q+EX combination. When the biggest moment values in *i* direction are examined, the biggest moment occurred in S40 column is obtained in G+Q+EX combination and this moment value is 7.89 kNm. In addition, the greatest moment value in *j* direction is 6.76 kNm (Table 1). When these values are examined, it is determined that very big forces and moments are on the S40 column.

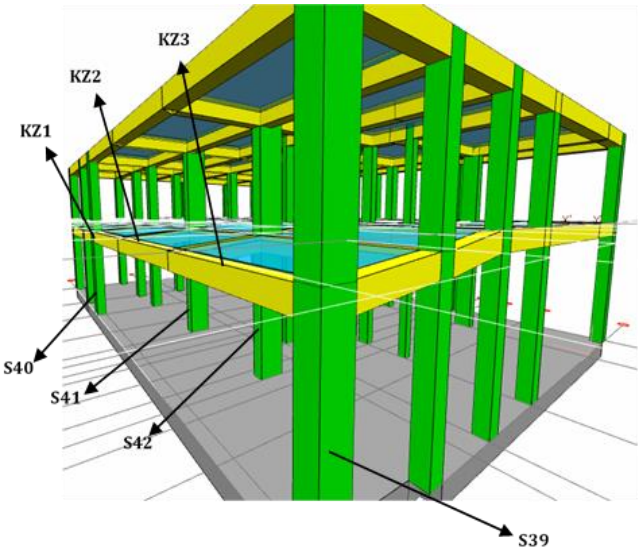

Fig. 11. The most critical sections for the current situation of the building.

Table 1. End forces for S40 column.

Load	Ni	V2i	V3i	M2i	M3i	Nj	V2j	V3j	M2j	M3j
Unit	kN	kN	kN	kNm	kNm	kN	kN	kN	kNm	kNm
G+Q+EX1	-14.5025	3.8774	0.1412	1.0019	7.8907	10.9293	4.4465	0.0424	0.8112	6.7651
G+Q+EX2	-14.9606	3.6124	0.2147	1.151	7.3354	11.2831	4.1399	-0.0117	0.8255	6.3374
G+Q+EY1	-21.0659	1.0628	1.2323	2.5222	3.711	15.6528	1.837	-0.5852	1.1936	3.5332
G+Q+EY2	-21.7739	0.6313	1.3573	2.7769	-1.2605	16.1889	1.3439	-0.6745	1.2251	0.2736
G+Q-EX1	-21.625	-2.6017	0.0827	-0.589	-6.1615	18.5192	-1.9367	0.0337	0.3868	-3.9555
G+Q-EX2	-21.1669	-2.3367	0.0092	-0.7381	-5.6062	18.1654	-1.6301	0.0878	0.3725	-3.5278
G+Q-EY1	-15.0616	0.2129	-1.0084	-2.1093	-1.9818	13.7958	0.6728	0.6613	0.0044	-0.7236
G+Q-EY2	-14.3537	0.6444	-1.1335	-2.364	2.9897	13.2596	1.1659	0.7506	-0.027	3.0832

It was determined as a result of on-site examinations that the explosions occurred in S39 column over time. According to performance analysis results, it was observed that the greatest moments and forces occurred in this column. The greatest normal force occurred in S39 column is -26.21kN in *i* direction and -10.23 kN in *j* direction. In addition, the largest shear force took place in this column is -5.58 kN in *i* direction and -2.98 kN in *j* direction, and these forces occurred in G+Q+EY combination. The biggest moments in this column are 11.33 kNm in *i* direction and -5.89 kNm in *j* direction (Table 2). When these values are evaluated, it is observed that larger loads and moments occurred in the S39 column when compared with S40 column and it was observed that more damage occurred in the S39 column.

S41 column is a column that is more inward than other columns. In Table 3, the end forces are presented considering the 8 different combinations for S41 column. The biggest normal force on this column is -52.8 kN, and this force was obtained in G+Q+EY combination in *i* direction. The largest shear force in *i* direction is 6.08 kN and the largest moment value in the same direction is

14.4 kNm. In *j* direction, the largest normal force is 3.2 kN. The largest shear force in the same direction is -0.16 kN. The maximum momentum value on this column is 0.0034 kNm. According to these values, the normal force, shear force in *i* direction are much more than *j* direction.

Table 2. End forces for S39 column.

Load	Ni	V2i	V3i	M2i	M3i	Nj	V2j	V3j	M2j	M3j
Unit	kN	kN	kN	kNm	kNm	kN	kN	kN	kNm	kNm
G+Q+EX1	-17.6446	-0.4132	2.3935	7.502	2.5474	-8.7533	-0.9911	-2.9699	-5.8891	-1.7796
G+Q+EX2	-16.473	0.4217	2.1592	6.8381	4.5809	-8.4962	-0.8773	-2.9571	-5.7653	-1.7749
G+Q+EY1	-26.2191	-5.5856	-0.693	1.9693	-14.1353	-10.658	-1.6476	-2.9846	-5.1369	-1.698
G+Q+EY2	-24.3029	-4.211	-1.0694	-3.7912	-10.9444	-10.236	-1.4615	-2.9674	-4.9715	-1.6962
G+Q-EX1	-19.002	-0.5947	-4.0105	-9.3649	-5.3447	-8.8902	-0.7288	-2.6494	-2.6065	-1.0605
G+Q-EX2	-20.1737	-1.4296	-3.7762	-8.701	-7.3782	-9.1474	-0.8425	-2.6623	-2.7303	-1.0652
G+Q-EY1	-10.4276	4.5777	-0.9241	-3.8322	11.338	-6.9856	-0.0723	-2.6348	-3.3587	1.1422
G+Q-EY2	-12.3437	3.2031	-0.5476	1.9283	8.1471	-7.4071	-0.2583	-2.652	-3.5241	-1.144

Table 3. End forces for S41 column.

Load	Ni	V2i	V3i	M2i	M3i	Nj	V2j	V3j	M2j	M3j
Unit	kN	kN	kN	kNm	kNm	kN	kN	kN	kNm	kNm
G+Q+EX1	-48.7032	0.7899	2.8457	7.027	-3.8821	3.1913	-0.1367	0.0842	-0.0021	0.0024
G+Q+EX2	-48.5319	0.9015	2.7247	6.7085	5.0593	3.187	-0.1367	0.0792	-0.0019	0.0024
G+Q+EY1	**-52.8743**	-4.375	0.2716	2.4961	-13.3664	3.2735	-0.0689	-0.0084	0.0018	0.0013
G+Q+EY2	-52.7482	-4.1513	0.0898	2.0797	-12.8567	**3.275**	-0.0736	-0.0125	0.0019	0.0015
G+Q-EX1	-49.3692	0.9242	-2.7437	-6.848	4.9191	3.2652	-0.1009	-0.0863	**0.0034**	0.0011
G+Q-EX2	-49.5405	0.8126	-2.6227	-6.5295	-4.0223	3.2695	-0.1009	-0.0813	0.0033	0.0011
G+Q-EY1	-45.1981	**6.0891**	-0.1696	-2.3171	**14.4034**	3.1831	**-0.1687**	0.0063	-0.0004	0.0022
G+Q-EY2	-45.3242	5.8654	0.0122	-1.9008	13.8937	3.1816	-0.164	0.0101	-0.0005	0.002

When the S42 column was examined, it was observed that the largest normal force in *i* direction was -56.3 kN (Table 4). This value is larger than S41 column. This is because the S42 column is one of the main columns and the most critical columns that hold the balcony floor. The biggest shear force obtained in *i* direction is 6.62 kN. This value is greater than the shear force value obtained for S41 column, and this shear force value was obtained in the same combination with S41 column. The greatest moment value in the same direction is 16.11 kN. The largest normal force occurring in *j* direction is 5.66 kN. The greatest shear force obtained in the same direction is -0.21 kN. Finally, the largest moment value obtained on this column is -0.005 kNm.

Table 4. End forces for S42 column.

Load	Ni	V2i	V3i	M2i	M3i	Nj	V2j	V3j	M2j	M3j
Unit	kN	kN	kN	kNm	kNm	kN	kN	kN	kNm	kNm
G+Q+EX1	-51.4463	1.0572	2.9484	7.1131	5.383	**5.6668**	-0.1696	0.1437	-0.0009	-0.0046
G+Q+EX2	-52.9597	1.6198	2.8359	6.8063	6.925	5.6517	-0.1748	0.1382	-0.0008	-0.0047
G+Q+EY1	**-56.3155**	-4.9636	0.0737	2.2645	-15.614	5.6125	-0.071	0.0073	0.0008	-0.0013
G+Q+EY2	-55.6158	-4.0023	-0.1085	-2.2028	-13.1544	5.5996	-0.083	-0.0005	0.0009	-0.0015
G+Q-EX1	-50.6571	0.6009	-2.882	-6.9882	-4.8848	5.3883	-0.1179	-0.1129	0.0016	-0.0017
G+Q-EX2	-51.1437	0.0383	-2.7695	-6.6814	-6.4268	5.4034	-0.1127	-0.1073	0.0015	-0.0016
G+Q-EY1	-47.7879	**6.6217**	-0.0074	-2.1397	**16.1122**	5.4425	**-0.2164**	0.0237	-0.0001	**-0.005**
G+Q-EY2	-48.4876	5.6604	0.1749	2.3277	13.6516	5.4555	-0.2045	0.0315	-0.0002	-0.0048

Balcony beams are named KZ1, KZ2 and KZ3. Table 5 shows the maximum force values for 8 combinations of KZ1 beam. Fig. 12 shows the deflection values occurred in the beam under G and Q loads. When Table 5 is examined, it is seen that the maximum normal force values in *i* and *j* directions for KZ1 beam are 1.12 kN and 2.13 kN, respectively. The biggest shear force value in *i* direction is -0.99 kN and the biggest shear force in *j* direction is 4.61 kN. The maximum moment values in *i* and *j* directions are 0.92 kNm and -7.17 kNm, respectively. Also, the deflection behavior of this beam under G and Q loads is shown in Fig. 12. Under G loading, deflection value at 0 m is -3.37 mm and at 4.5 m deflection value is -0.45 mm. The biggest deflection value in the beam under Q loading is -0.45 mm (Fig. 12).

Table 5. End forces for KZ1 beam.

Load	Ni	V2i	V3i	M2i	M3i	Nj	V2j	V3j	M2j	M3j
Unit	kN	kN	kN	kNm	kNm	kN	kN	kN	kNm	kNm
G+Q+EX1	0.5186	-0.5063	-0.1428	-0.0825	0.7007	-1.8608	**4.6131**	0.043	0.2804	**-7.1787**
G+Q+EX2	0.4959	-0.5338	-0.1418	-0.0819	0.6893	-1.7843	4.5606	0.0359	0.2762	-7.0227
G+Q+EY1	1.076	-0.4052	-0.2673	-0.1702	0.9146	0.348	4.611	-0.1142	0.3498	-6.9812
G+Q+EY2	0.6283	-0.4371	-0.2776	-0.192	**0.9232**	0.8566	4.4986	-0.1254	0.3463	-6.721
G+Q-EX1	1.1049	-0.8919	-0.2009	-0.1378	-0.0362	**2.1338**	3.7048	-0.39	0.3268	-3.7176
G+Q-EX2	**1.1276**	-0.8644	-0.2019	-0.1383	-0.0248	2.0573	3.7573	-0.3829	0.3311	-3.8736
G+Q-EY1	0.5475	**-0.993**	-0.0764	-0.05	-0.2501	-0.075	3.7069	-0.2328	0.2574	-3.9151
G+Q-EY2	0.9953	-0.9611	-0.0661	-0.0283	-0.2587	-0.5836	3.8193	-0.2216	0.261	-4.1753

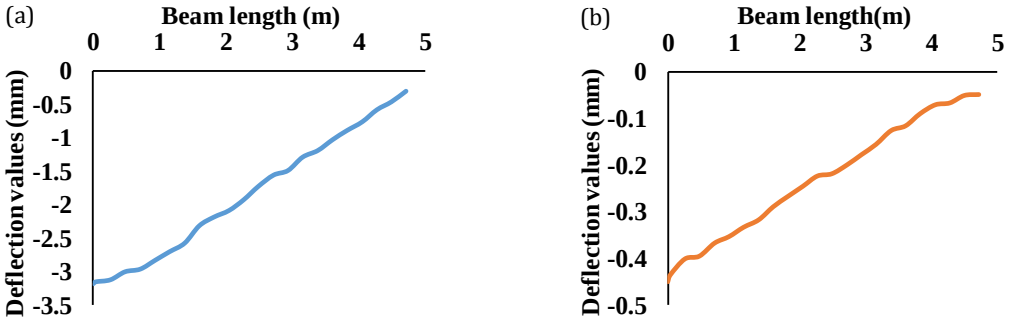

Fig. 12. Deflection values for KZ1 beam: (a) Under G loading; (b) Under Q loading.

When Table 6 is examined, force values are seen for KZ2 beam. The largest normal forces occurred in the KZ2 beam in *i* and *j* directions are 4.06 kN and 1.47 kN, respectively. In addition, the largest shear force value in *i* direction is -5.05 kN and the largest shear force in *j* direction is 1.49 kN. Besides, the greatest moment values in *i* and *j* directions are -8.11 kNm and 1.02 kNm (Table 6). Moreover, deflection values of this beam in G and Q loads are presented in Fig.13. The maximum deflection value occurred in the beam under G loading is -4.01 mm and this value occurred in the middle parts of the beam. In Q loading, the biggest deflection value occurred right in the middle of the beam and the deflection value is -0.61 mm. Finally, when the KZ3 beam is examined, it is seen that the largest shear force values in *i* and *j* directions are -2.07 kN and 1.88 kN, respectively (Table 7). In addition, the largest moment values in *i* and *j* directions were determined to be -1.33 kNm and -0.48 kNm. In Fig. 14, the biggest deflection values of the KZ3 beam under G and Q loads are presented. The largest deflection obtained in beam under G loading is -3.4 mm and this value occurred at the ends of the beam. The biggest deflection value acquired in the beam under Q loading is -0.46 mm.

Table 6. End forces for KZ2 beam.

Load	Ni	V2i	V3i	M2i	M3i	Nj	V2j	V3j	M2j	M3j
Unit	kN	kN	kN	kNm	kNm	kN	kN	kN	kNm	kNm
G+Q+EX1	**4.0688**	-3.2688	0.0788	0.1044	-2.2957	**1.4731**	**1.4986**	0.1147	-0.0387	-0.3564
G+Q+EX2	3.8195	-3.2798	0.1373	0.118	-2.3929	1.4365	1.4941	0.1027	-0.0303	-0.4146
G+Q+EY1	1.7387	-4.5999	-0.5744	0.1131	-6.7931	0.7974	0.7443	0.2079	-0.1501	**1.0271**
G+Q+EY2	1.3104	-4.6218	-0.4578	0.1427	-6.9585	0.4713	0.7419	0.1958	-0.1386	0.9242
G+Q-EX1	-1.3995	**-5.0542**	-0.1308	0.3456	**-8.1118**	-0.3083	0.5638	0.0703	-0.0981	0.8377
G+Q-EX2	-1.1503	-5.0432	-0.1893	0.332	-8.0145	-0.2717	0.5682	0.0823	-0.1065	0.8959
G+Q-EY1	0.9305	-3.7231	0.5224	0.3369	-3.6144	0.3674	1.318	-0.0229	-0.0133	-0.5458
G+Q-EY2	1.3588	-3.7011	0.4058	0.3072	-3.4489	0.6935	1.3204	-0.0108	-0.0018	-0.4429

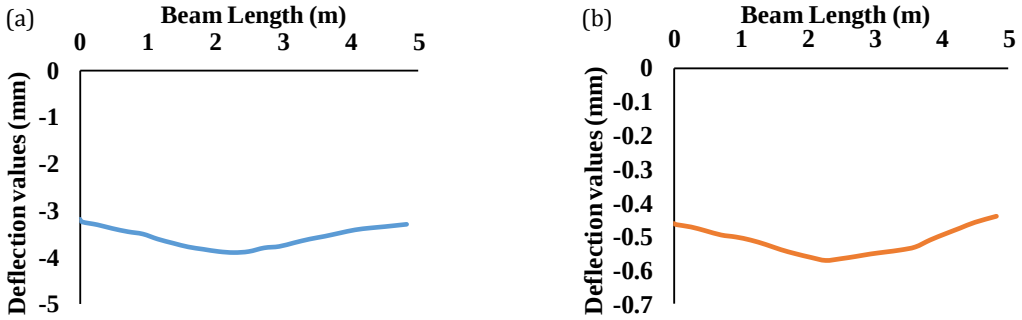

Fig. 13. Deflection values for KZ2 beam: (a) Under G loading; (b) Under Q loading.

Table 7. End forces for KZ3 beam.

Load	Ni	V2i	V3i	M2i	M3i	Nj	V2j	V3j	M2j	M3j
Unit	kN	kN	kN	kNm	kNm	kN	kN	kN	kNm	kNm
G+Q+EX1	**0.9482**	-1.9184	0.3348	0.1365	-0.5125	0.488	1.8541	-0.0748	-0.0285	-0.3113
G+Q+EX2	0.9471	-1.9459	0.3334	0.141	-0.9508	0.4461	1.834	-0.0833	-0.0265	-0.2869
G+Q+EY1	0.3691	-1.846	0.2175	0.0309	-0.1181	0.8361	1.8156	-0.1527	-0.0376	0.3567
G+Q+EY2	0.088	-1.9083	0.2219	0.0411	-0.2706	0.2988	1.7885	-0.1656	-0.0415	0.4227
G+Q-EX1	-0.3304	-1.999	0.1828	0.0506	-0.9361	0.6726	1.8175	-0.3315	0.0624	0.2476
G+Q-EX2	-0.3293	-1.9715	0.1843	0.0461	-0.4978	0.7153	1.8375	-0.323	0.0605	0.2231
G+Q-EY1	0.2487	**-2.0714**	0.3002	0.1562	**-1.3305**	0.3253	1.856	-0.2535	0.0715	-0.4205
G+Q-EY2	0.5298	-2.0091	0.2957	0.146	-1.178	0.8626	**1.883**	-0.2407	0.0755	**-0.4865**

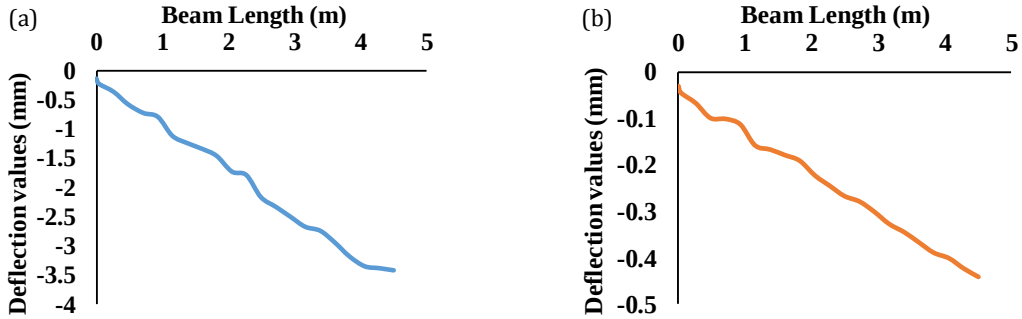

Fig. 14. Deflection values for KZ3 beam: (a) Under G loading; (b) Under Q loading.

5.2. Analysis results for situation after strengthening

The reinforcement was carried out on damaged carrier elements for the current situation of the building, and this was applied to 4 balcony main columns. In this section, the maximum force values obtained after reinforcement for 4 main columns and 3 balcony beams are presented. Table 8 shows the maximum forces for the S40 column. As can be seen from Table 8, the big-gest normal force affecting the column is -35.6 kN in *i* direction and 23.1 kN in *j* direction. When these values are compared with the currently obtained values, it can be seen that the S40 column can carry more normal force after reinforcement. When the largest shear forces occurred in *i* and *j* directions are examined, it is seen that the maximum shear force in *i* direction is 10.24 kN and in *j* direction it is 10.27 kN. When the current analysis results and post-reinforcement analysis results are examined, it is concluded that the columns can carry more shear force after reinforcement. Finally, when the largest moment values in *i* and *j* directions are examined, it is seen that the moment values are 30.46 kNm and 10.3 kNm, respectively (Table 8).

The end force values of S39 column under 8 load combinations are presented in Table 9. When Table 9 is examined, it is seen that the load and moment values that the S39 column can carry are close to the load and moment values that the S40 column can carry. The greatest normal force values occurring in *i* and *j* directions are -36.9 kN and -17.5 kN, respectively. In addition, the largest shear force values occurring in *i* and *j* directions are -10.02 kN and -3.55 kN, respectively. It is concluded that for the S39 column, the normal force and shear forces obtained after reinforcement are higher than the normal force and shear forces obtained. Finally, it is seen that the maximum moment values that the column can carry *i* and *j* directions are much larger after reinforcement (Table 9).

Table 8. End forces for S40 column.

Load	Ni	V2i	V3i	M2i	M3i	Nj	V2j	V3j	M2j	M3j
Unit	kN	kN	kN	kNm	kNm	kN	kN	kN	kNm	kNm
G+Q+EX1	-24.9408	**10.2401**	2.67	15.1234	**30.4665**	14.5928	**10.2725**	-1.1492	-2.1116	**10.3**
G+Q+EX2	-25.7792	9.6012	3.5366	17.3775	28.5153	15.0945	9.5511	-1.3727	-2.8172	9.8458
G+Q+EY1	-34.2425	0.5635	7.3494	22.1163	-5.4131	21.2956	1.2501	-3.425	-1.8632	-1.6568
G+Q+EY2	**-35.614**	-0.505	8.8625	26.1148	-8.7449	22.0898	0.0396	-3.8044	-3.1088	-2.4848
G+Q-EX1	-31.6792	-8.2347	-1.4106	-11.6412	-27.1047	**23.1024**	-7.0087	-0.8044	5.3134	-7.0174
G+Q-EX2	-30.8408	-7.5958	-2.2772	-13.8953	-25.1535	22.6008	-6.2872	-0.6172	6.0191	-6.5631
G+Q-EY1	-22.3775	1.4419	-6.09	-18.6341	8.7749	16.3996	2.0137	1.435	5.065	4.9395
G+Q-EY2	-21.006	2.5104	-7.6031	-22.6325	12.1067	15.6055	3.2242	1.8144	6.3106	5.7674

Table 9. End forces for S39 column.

Load	Ni	V2i	V3i	M2i	M3i	Nj	V2j	V3j	M2j	M3j
Unit	kN	kN	kN	kNm	kNm	kN	kN	kN	kNm	kNm
G+Q+EX1	-26.6655	3.5962	7.8924	28.9874	17.9951	-13.6691	-2.9335	-3.3922	-7.0787	-9.1926
G+Q+EX2	-25.4067	5.669	7.4203	27.2472	24.578	-13.2283	-2.8526	-3.4379	-7.1503	-9.6613
G+Q+EY1	**-36.9216**	-9.9872	-1.6869	-8.7823	-41.067	**-17.592**	**-3.5511**	-3.1639	-2.0658	-6.4892
G+Q+EY2	-34.8039	-6.4941	-2.4541	-11.7044	-30.1029	-16.8455	-3.4126	-3.2347	-2.1687	-7.274
G+Q-EX1	-32.2685	-6.1465	-10.0284	-31.3217	-30.3015	-15.2505	-0.4679	-2.8166	-0.0211	2.5691
G+Q-EX2	-33.5272	-8.2193	-9.5564	-29.5815	-36.8843	-15.6913	-0.5489	-2.771	0.0505	3.0377
G+Q-EY1	-22.0123	7.4369	-0.4492	6.448	28.7607	-11.3276	0.1497	-3.045	-5.034	-0.1344
G+Q-EY2	-24.13	3.9438	0.3181	9.3701	17.7966	-12.0741	0.0112	-2.9742	-4.9311	0.6505

According to Table 10, the biggest normal forces occurred on the S41 column for *i* and *j* directions are -65.01 kN and 32.77 kN, respectively. Moreover, the largest shear force took place in *i* direction is 12.95 kN and -3.81 kN in *j* direction. The maximum moment values in *i* and *j* directions for the S41 column are -44.14 kNm and 5.96 kNm (Table 10), respectively. These values are much larger than force values obtained for current situation. This result is an indication that strengthening and historical structures can carry more strength and survive more. When Table 11 is examined, the end forces and moments of S42 column are seen. When com-pared with S41 column, it is seen that S42 column can carry similar loads and moments. The largest normal forces occurred in *i* and *j* directions are -67.35 kN and 34.52 kN, respectively. In addition, the largest shear force value in *i* direction is 10.86 kN and 5.84 kN in *j* direction. Finally, the largest moment for *i* and *j* directions are -42.18 kNm and 4.97 kNm, respectively.

Table 10. End forces for S41 column.

Load	Ni	V2i	V3i	M2i	M3i	Nj	V2j	V3j	M2j	M3j
Unit	kN	kN	kN	kNm	kNm	kN	kN	kN	kNm	kNm
G+Q+EX1	-61.6509	-0.25	8.5475	26.986	-20.3559	31.8096	-2.4216	3.6752	5.2608	4.8879
G+Q+EX2	-61.5739	-0.6433	8.5353	26.7604	-21.1942	31.8737	-2.667	3.6068	5.6704	5.6919
G+Q+EY1	-65.1565	-10.3567	-0.0281	6.6646	-42.5935	32.6335	-1.0561	0.0984	1.7837	4.5999
G+Q+EY2	**-65.0191**	-11.0301	0.0095	6.3548	**-44.1465**	**32.7707**	-1.5781	0.0077	2.3997	**5.9697**
G+Q-EX1	-60.4007	2.175	-8.8615	-27.3627	16.383	29.7635	-2.4401	**-3.8171**	0.8604	0.3315
G+Q-EX2	-60.4777	2.5682	-8.8492	-27.1371	17.2213	29.6994	-2.1947	-3.7487	0.4508	-0.4726
G+Q-EY1	-56.8951	12.2817	-0.2858	-7.0413	38.6206	28.9397	-3.8056	-0.2403	4.3375	0.6194
G+Q-EY2	-57.0325	**12.9551**	-0.3234	-6.7315	40.1736	28.8025	-3.2836	-0.1496	3.7215	-0.7504

Table 11. End forces for S42 column.

Load	Ni	V2i	V3i	M2i	M3i	Nj	V2j	V3j	M2j	M3j
Unit	kN	kN	kN	kNm	kNm	kN	kN	kN	kNm	kNm
G+Q+EX1	-62.8816	2.9726	8.5852	26.83	16.7672	32.8466	-0.9902	**5.8495**	4.5431	0.4245
G+Q+EX2	-62.5615	3.864	8.5956	26.6401	20.1994	32.7544	-1.2195	5.8155	**4.9761**	0.6165
G+Q+EY1	**-67.3568**	-8.8745	-0.1915	6.381	**-42.1887**	**34.529**	1.1498	1.4108	3.4787	0.1533
G+Q+EY2	-66.917	-7.2738	-0.1774	-6.7407	-36.3103	34.3787	0.7355	1.3982	4.2231	0.4709
G+Q-EX1	-63.9995	-0.983	-8.7864	-27.1143	-22.7481	33.1155	-1.8639	-3.0975	1.4281	3.7528
G+Q-EX2	-64.3196	-1.8743	-8.7969	-26.9244	-26.1802	33.2077	-1.6346	-3.0635	0.9951	3.5608
G+Q-EY1	-59.5243	**10.8642**	-0.0098	-6.6653	36.2079	31.4331	-4.0039	1.3413	2.4926	4.024”
G+Q-EY2	-59.964	9.2635	-0.0238	6.4563	30.3295	31.5834	-3.5895	1.3538	1.7482	3.7064

Table 12 presents the end forces for the KZ1 beam. The largest normal force value in *i* direction affecting the beam is 1.81 kN. In addition, the largest normal force in *j* direction is 3.85 kN. The greatest moment value in *i* direction is -0.78 kNm and the greatest moment value in *j* direction is -7.36 kNm. In Fig. 15, deflection values took place in the beam under G and Q loading are presented graphically. Under G loading, deflection value of -0.1 mm occurred in the beam at 0 m. However, deflection of -1.61 mm took place at the end of the beam (4.7 m) (Fig. 15a). Under Q loading, the maximum deflection occurred at the ends of the beam and its value is -0.27 mm (Fig. 15b).

Table 12. End forces for KZ1 beam.

Load	Ni	V2i	V3i	M2i	M3i	Nj	V2j	V3j	M2j	M3j
Unit	kN	kN	kN	kNm	kNm	kN	kN	kN	kNm	kNm
G+Q+EX1	0.7922	-0.6835	-0.0651	-0.0198	0.419	-2.8833	4.642	0.3589	0.0992	**-7.3611**
G+Q+EX2	0.5136	-0.7055	-0.0765	-0.1169	0.4208	-2.9764	4.5906	0.3961	0.0869	-7.2328
G+Q+EY1	-0.0223	-0.6944	-0.2103	-0.1482	0.437	0.5966	4.254	0.1622	0.1935	-6.6254
G+Q+EY2	-0.4492	-0.714	-0.3269	-0.1882	0.4403	0.7894	4.1444	0.2376	0.1691	-6.3903
G+Q-EX1	0.5737	-1.1491	-0.1801	-0.1175	-0.758	3.7651	3.1172	-0.86	0.5257	-2.9859
G+Q-EX2	0.8523	-1.1271	-0.1688	-0.0204	-0.7597	**3.8582**	3.1686	-0.8972	0.5381	-3.1142
G+Q-EY1	1.3882	-1.1382	-0.0349	0.011	-0.7759	0.2851	3.5052	-0.6633	0.4315	-3.7216
G+Q-EY2	**1.8151**	-1.1186	0.0817	0.0509	**-0.7792**	0.0924	3.6149	-0.7387	0.4559	-3.9567

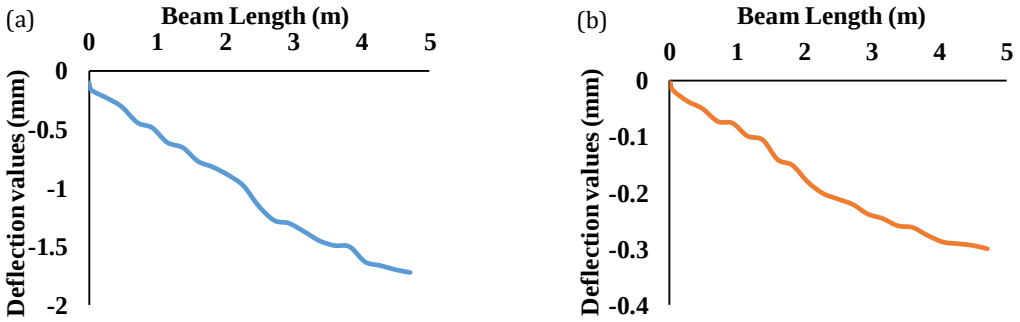

Fig. 15. Deflection values for KZ1 beam: (a) Under G loading; (b) Under Q loading.

In Tables 13 and 14, force values are presented for 8 different combinations for KZ2 and KZ3 beams. According to Table 13, maximum normal force of 2.41 kN occurred for G+Q+EX loading in *i* direction in the KZ2 beam. In *j* direction, 1.93 kN normal force was obtained. In addition, the maximum shear forces in *i* and *j* directions are 2.04 kN and 1.98 kN, respectively. Finally, the maximum moment values in *i* and *j* directions are -1.53 kNm and -0.87 kNm, respectively (Table 13). Also, deflection values occurred under G and Q loads in KZ2 beam are presented in Fig. 16. According to Fig. 16, maximum deflection took place in the middle parts of the beam under G loading and its numerical value is -2.12 mm. Under Q loading, the maximum deflection is similarly observed in the middle parts of the beam and its numerical value is -0.4 mm.

Table 14 presents the maximum force values for the KZ3 beam. The largest normal forces occurred in *i* and *j* directions are 9.45 kN and 3.05 kN, respectively. Considering 8 different combinations in this beam, the largest

shear force value is -4.95 kN in the *i* direction and 1.6 kN in the *j* direction. Finally, the greatest moment values in the KZ3 beam in *i* and *j* directions are -7.51 kNm and -1.09 kNm, respectively. Deflection values under G and Q loads for KZ2 beam are presented in Fig. 17. The maximum deflection for G loading occurred at the ends of the beam and its value is -1.58 mm. In addition, the biggest deflection value for Q loading is -0.28 mm. In addition, in Table 15, deflection values occurred in beams before and after reinforcement were compared and tabulated. As can be seen from Table 15, earthquake reinforcement in historical buildings reduces deflection values in beams.

Table 13. End forces for KZ2 beam.

Load	Ni	V2i	V3i	M2i	M3i	Nj	V2j	V3j	M2j	M3j
Unit	kN	kN	kN	kNm	kNm	kN	kN	kN	kNm	kNm
G+Q+EX1	**2.4181**	-1.9981	0.4074	0.193	-0.9261	0.9735	1.8793	0.0266	-0.0506	-0.6934
G+Q+EX2	2.2173	-2.0239	0.4006	0.1947	-1.2984	0.6584	1.8596	0.0322	-0.0539	-0.659
G+Q+EY1	0.1875	-1.9251	0.1841	0.0478	-0.719	-0.12	1.8267	0.0518	-0.0656	-0.0582
G+Q+EY2	-0.4105	-1.9848	0.1805	0.0538	-0.8555	-0.7814	1.8084	-0.0529	-0.0519	0.0111
G+Q-EX1	-1.3955	-1.9729	0.0873	0.0364	-1.3241	0.1803	1.9137	-0.27	0.1006	-0.1746
G+Q-EX2	-1.1947	-1.9471	0.0941	0.0347	-0.9518	0.4954	1.9334	-0.2756	0.1039	-0.2089
G+Q-EY1	0.8352	**-2.0458**	0.3105	0.1815	**-1.5312**	1.2738	1.9663	-0.2952	0.1156	-0.8098
G+Q-EY2	1.4331	-1.9861	0.3141	0.1755	-1.3947	**1.9352**	**1.9846**	-0.1904	0.1019	**-0.879**

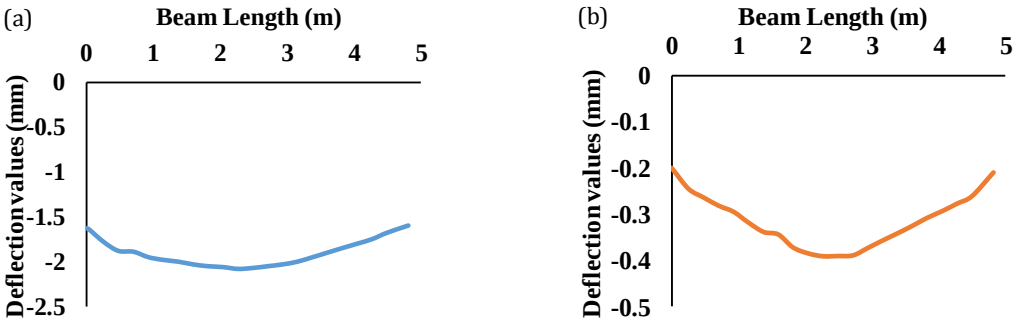

Fig. 16. Deflection values for KZ2 beam: (a) Under G loading; (b) Under Q loading.

Table 14. End forces for KZ3 beam.

Load	Ni	V2i	V3i	M2i	M3i	Nj	V2j	V3j	M2j	M3j
Unit	kN	kN	kN	kNm	kNm	kN	kN	kN	kNm	kNm
G+Q+EX1	**9.4559**	-3.1857	1.4965	0.6483	-2.666	**3.0547**	1.6025	0.107	0.0095	-1.0472
G+Q+EX2	8.9764	-3.17	1.8195	0.7214	-2.6935	2.8082	**1.6056**	0.0944	0.0172	**-1.0932**
G+Q+EY1	1.0484	-4.5252	-1.7616	-0.2927	-6.5348	0.4798	0.9807	0.1748	-0.0971	0.3714
G+Q+EY2	0.2457	-4.501	-1.1794	-0.1571	-6.5827	-0.1855	0.9929	0.1579	-0.0857	0.2851
G+Q-EX1	-6.3024	-4.9345	-1.6016	-0.24	**-7.5151**	-1.6796	0.8938	-0.0319	-0.04966	0.4676
G+Q-EX2	-5.8229	**-4.9502**	-1.9246	-0.3131	-7.4882	-1.4331	0.8907	-0.0192	-0.0573	0.5137
G+Q-EY1	2.1051	-3.595	1.6565	0.701	-3.6469	0.8953	1.5156	-0.0997	0.0571	-0.951
G+Q-EY2	2.9078	-3.6192	1.0743	0.5653	-3.599	1.5606	1.5033	-0.0828	0.0456	-0.8646

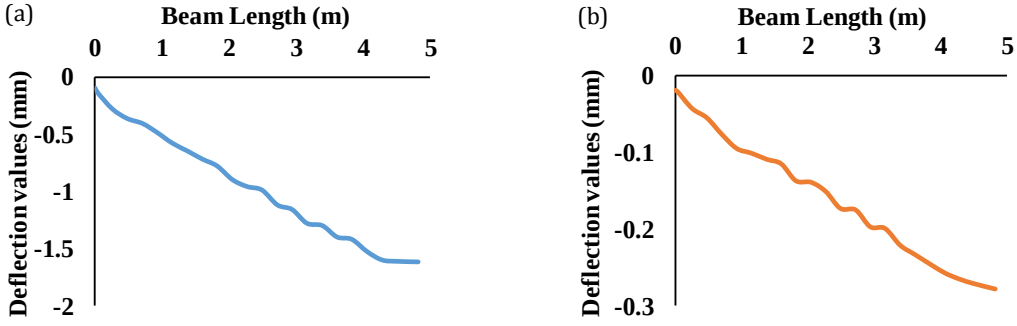

Fig. 17. Deflection values for KZ3 beam: (a) Under G loading; (b) Under Q loading.

Table 15. Deflection values in beams before and after reinforcement.

Beam Name	KZ1		KZ2	KZ3	
Length	0 m	0.45 m	Middle point	0 m	0.45 m
Deflection Before Strengthening (mm)	-0.45	-3.37	-4.01 mm	-0.25 mm	-3.4 mm
Deflection After Strengthening (mm)	-0.1 mm	-1.61 mm	-2.12 mm	-0.15 mm	-1.58 mm

6. Conclusions

In this study, it is aimed to determine how important the jacketing is for earthquake safety and service life of historical buildings. For this purpose, Zonguldak historical cinema building was selected for 3D modeling in this study. After the building was modelled as three dimensional, current situation of building was analyzed by using IDECAD program. Later, it was ensured that the building survived for a long time by using jacketing method. According to analysis results, jacketing behaviour of concrete historical building is evaluated as below.

- Strengthening historical structures by using jacketing is great importance for safety and future of these structures. During jacketing process, great care should be taken thickness and location of jacketing.
- During strengthening of historical buildings, care should be taken to consider the damaged areas that were determined by using 3D modeling and 3D analyzing.
- When compared the current situation of building and strengthened situation of building, it is clearly observed that the moments and shear forces resisted to demolition are higher after strengthening for balcony beams.
- According to the 2018 Turkish earthquake code, although the collapse damage zone was obtained for RC building before strengthening, limited damage zone was obtained after strengthening.
- When compared before and after strengthening process, it was clearly seen that more deflections occurred in balcony beams before strengthening and that these deflection values decreased after strengthening.
- The moments of the columns and beams after strengthening have significantly increased due to the increased rigidity by jacketing. This result is an indication that historical structures can carry more strength and moment and survive more with jacketing.

References

Aigwi IE, Egbelakin T, Ingham J, Phipps R, Rotimi J, Filippova O (2019). A performance-based framework to prioritise underutilised historical buildings for adaptive reuse interventions in New Zealand. *Sustainable Cities and Society*, 48, 101547.

Arıoğlu E, Anadol K, Arıoğlu AÜ (2007). Uluslararası deprem mühendisliği açısından önemli bir olgu ve kayıp: "Güçlendirilmiş Adapazarı Vilayet Binası". *Tarihi Eserlerin Güçlendirilmesi ve Geleceğe Güvenle Devredilmesi Sempozyumu*, 27-29 September 2007, 241-254.

Aydın AP, Kul FN, Dönmez C, Erberik A (2015). Urla eski Tekel Binası (Arditi Köşkü): Yangın öncesi durum ve yapısal iyileştirme-güçlendirme kararları. *5. Tarihi Eserlerin Güçlendirilmesi ve Geleceğe Güvenle Devredilmesi Sempozyumu*, 1-3 October 2015, 13-28.

Cakir F, Uckan E, Shen J, Seker BS, Akbas B (2015). Seismic damage evaluation of historical structures during Van earthquake, October 23, 2011. *Engineering Failure Analysis*, 58, 249-266.

Ercan E (2018). Assessing the impact of retrofitting on structural safety in historical buildings via ambient vibration tests. *Construction and Building Materials*, 164, 337-349.

Günaydın M (2019). Seismic performance evaluation of a fire-exposed historical structure using an updated finite element model. *Engineering Failure Analysis*, 106, 104149.

Karaton M, Aksoy HS, Sayın E, Calayır Y (2017). Nonlinear seismic performance of a 12th century historical masonry bridge under different earthquake levels. *Engineering Failure Analysis*, 79, 408-421.

Kasapgil M (2007). Adana Ulucami minaresi güçlendirme çalışması. *Tarihi Eserlerin Güçlendirilmesi ve Geleceğe Güvenle Devredilmesi Sempozyumu*, 27-29 September 2007, 219-224.

Kasapgil ME (2007). Eski eserlerde, yığma duvarların, kubbelerin, tonozların ve temellerin enjeksiyon reçineleri ve ankraj sistemleriyle güçlendirilmesi. *Tarihi Eserlerin Güçlendirilmesi ve Geleceğe Güvenle Devredilmesi Sempozyumu*, 27-29 September 2007, 215-218.

Korkmaz M, Ozdemir MA, Kavali E, Cakir F (2018). Performance-based assessment of multi-story unreinforced masonry buildings: The case of historical Khatib School in Erzurum, Turkey. *Engineering Failure A*nalysis, 94, 195-213.

Mahrebel HA (2006). Tarihi Yapılarda Taşıyıcı Sistem Özellikleri, Hasarlar, Onarım ve Güçlendirme Teknikleri. *M.Sc. thesis*, İstanbul Technical University, Turkey.

Onat O, Sayın E (2015). Tarihi Tağar Köprüsünün doğrusal olmayan sismik analizi. *5. Tarihi Eserlerin Güçlendirilmesi ve Geleceğe Güvenle Devredilmesi Sempozyumu*, 1-3 October 2015, 301-311.

Orhan S, Özyazıcıoğlu MH (2015). Determination of collapse load of single span circular masonry arch bridges by the methods of limit analysis. *Pamukkale University Journal of Engineering Sciences*, 21(3), 88-93.

Örmecioğlu HT (2010). Tarihi yapıların yapısal güçlendirilmesinde ana ilkeler ve yaklaşımlar. *Journal of Polytechnic*, 13(3), 233-237.

Sert H, Partal EM (2015). Tarihi köprülerin restorasyonları kapsamında yürütülen yapısal analiz çalışmaları ve sonuçları. *5. Tarihi Eserlerin Güçlendirilmesi ve Geleceğe Güvenle Devredilmesi Sempozyumu,* 1-3 October 2015, 83-97.

Sert H, Yılmaz S (2015). Tarihi Malabadi (Batman Su) Köprüsü'nde yürütülen restorasyon-konservasyon çalışmaları. *5. Tarihi Eserlerin Güçlendirilmesi ve Geleceğe Güvenle Devredilmesi Sempozyumu*, 1-3 Ekim 2015, s.143-153.

Sesigür H, Çelik OC (2007). Ahi Çelebi Camisinin onarımı ve güçlendirilmesi. *Tarihi Eserlerin Güçlendirilmesi ve Geleceğe Güvenle Devredilmesi Sempozyumu*, 27-29 September 2007, 231-238.

Türker T, Bayraktar A, Kocaman İ, Çoruhlu B (2015). Ölçekli yığma taş kemer köprü modelinin dinamik davranışının deneysel ve analitik olarak incelenmesi. *5. Tarihi Eserlerin Güçlendirilmesi ve Geleceğe Güvenle Devredilmesi Sempozyumu*, 1-3 October 2015, 113-126.

Valente M, Milani G (2019). Damage assessment and collapse investigation of three historical masonry palaces under seismic actions. *Engineering Failure Analysis*, 98, 10-37.

Challenge Journal of Structural Mechanics

Research Article

Effect of high temperature on the mechanical behavior of cement-bonded wood composite produced with wood waste

Mehmet Canbaz [a,*], İlkay Kara [a], İlker Bekir Topçu [a]

[a] *Department of Civil Engineering, Eskişehir Osmangazi University, 26480 Eskişehir, Turkey*

ABSTRACT

The increase in the population day by day and urbanization has led to a rapid increase in the construction sector. With the increase in demand in construction, the product types of building materials are increasing. It is seen that wastes are formed during and after the production of the materials used in the building. This highlights studies on waste management and recycling of waste. After construction activities, wastes are recycled or converted to secondary products. One of these is wood waste, a traditional building material. In addition to the production of wood furniture, it is used in various areas from the beginning of construction to the end of the building. In this study, sawdust, which is the waste of a woodworking company, was used. Utilizing the advantages of wood, recyclable and sustainable cement bonded wood composite production practices have been explored. It is aimed to produce nature and environment friendly, ecological and economic and durable composite materials. In this research, it is aimed to determine the optimum ratio by using different ratios of sawdust-cement while keeping the water-cement ratio constant in production. The specimens taken from the production were exposed to high temperature after gaining strength. The strength results, unit weights and ultrasonic pulse velocity results of cement bonded wood composite samples exposed to high temperature were examined. Although cement bonded wood composites are exposed to high temperatures such as 400°C, it has been observed that strength is achieved. With this study, an alternative area was proposed for the evaluation of these wastes.

ARTICLE INFO

Article history:
Received 28 August 2020
Revised 31 October 2020
Accepted 10 December 2020

Keywords:
Wood
Cement-bonded
Sawdust
Composite
High temperature

1. Introduction

Composite material is defined as the combination of two or more materials that give superior properties compared to the use of its components individually. Each material composing the composite materials composition retains its physical, chemical and mechanical properties (Campbell, 2010; Aras and Kalaycıoğlu, 2016). In wood-based composite materials, they typically coexist with cement and wood or its derivatives (sawdust, chip, fiber, etc.) in the binding of matrix cement. These materials are suitable for building and construction works as they provide easy production, as well as improved biodegradation and are produced from sustainable sources (Şahin et al., 2019).

With the decreasing forest presence and rising wood prices worldwide, it has increased the tendency towards wood composite materials (Kaya, 2018). Wood waste is produced worldwide. Recycling and reuse of wood waste as aggregate in concrete or mortar becomes a sustainable and developed solution for building materials (Li et al., 2019a). As an alternative to traditional construction materials, wastes such as bio-sourced wood fibers combined with cement matrix have been used. These materials, which are cheap and environmentally friendly to manufacture, provide economic and ecological solutions. Wood cement composites have low weight, thermal and acoustic properties, ease of recycling and less energy requirements (Li et al., 2019b).

* *Corresponding author*. Tel.: +90-222-239-3750 ; Fax: +90-222-239-3613 ; E-mail address: mcanbaz@ogu.edu.tr (M. Canbaz)
ISSN: 2149-8024 / DOI: https://doi.org/10.20528/cjsmec.2021.01.005

Cement bonded wood composites is the name given to the material with high specific gravity and smooth surface, which is formed by combining wood chips or agricultural plants with cement, water and various chemical substances in appropriate proportions (Kalaycıoğlu, 2016). The compatibility of water, sawdust and cement in wood composites significantly affects the hardening and strength properties of cement (Yel, 2020). Water / cement ratio is important for cementitious composites. It is also possible for wood to absorb the water required for hydration of the cement. In this case, some of the cement cannot be hydrated and the composite causes low strength (Caprai et al., 2018; Kochova et al., 2020). Since wood is a natural material, its properties can change even within the same type. This case is an important factor for lignocellulosic composite (Gauvin et al., 2019). For the production of high quality cement bonded wood composite, woods such as spruce, fir and pine with the lowest water solubility are recommended. Depending on the type of wood, the water-soluble substances change and affect the setting time of the wood-cement mixture (Sanaev et al., 2016). Hemicelluloses in Wood decompose, form monosaccharides and polysaccharides and can delay cement hydration (Berger, 2020).

Cement bonded woodcretes can be versatile lightweight building materials such as interior panels, noise barriers, and partition walls (Hossain et al., 2018). The combination of cement and wood offers advantages such as strength performance, structural durability, lightness, heat / sound insulation and fire resistance in wood cement composites (Wang, 2017). Cement bonded wood composites have high resistance and dimensional stability against external weather conditions or rapid aging. These materials have high fire, sound and heat insulation as well as high resistance to biological factors. Although they are heavier than resin-based boards, they are lighter than concrete. For this reason, it is preferred especially in the sections that are not exposed to load in the prefabricated building sector (Kaya, 2018). Cemented chipboards, one of the cemented wood composites, are defined according to the type, shape, color and surface condition of the cement used in the TS EN 633 standard (TS EN 633). Examples of wood-cement composites used in practice are shown in Fig. 1.

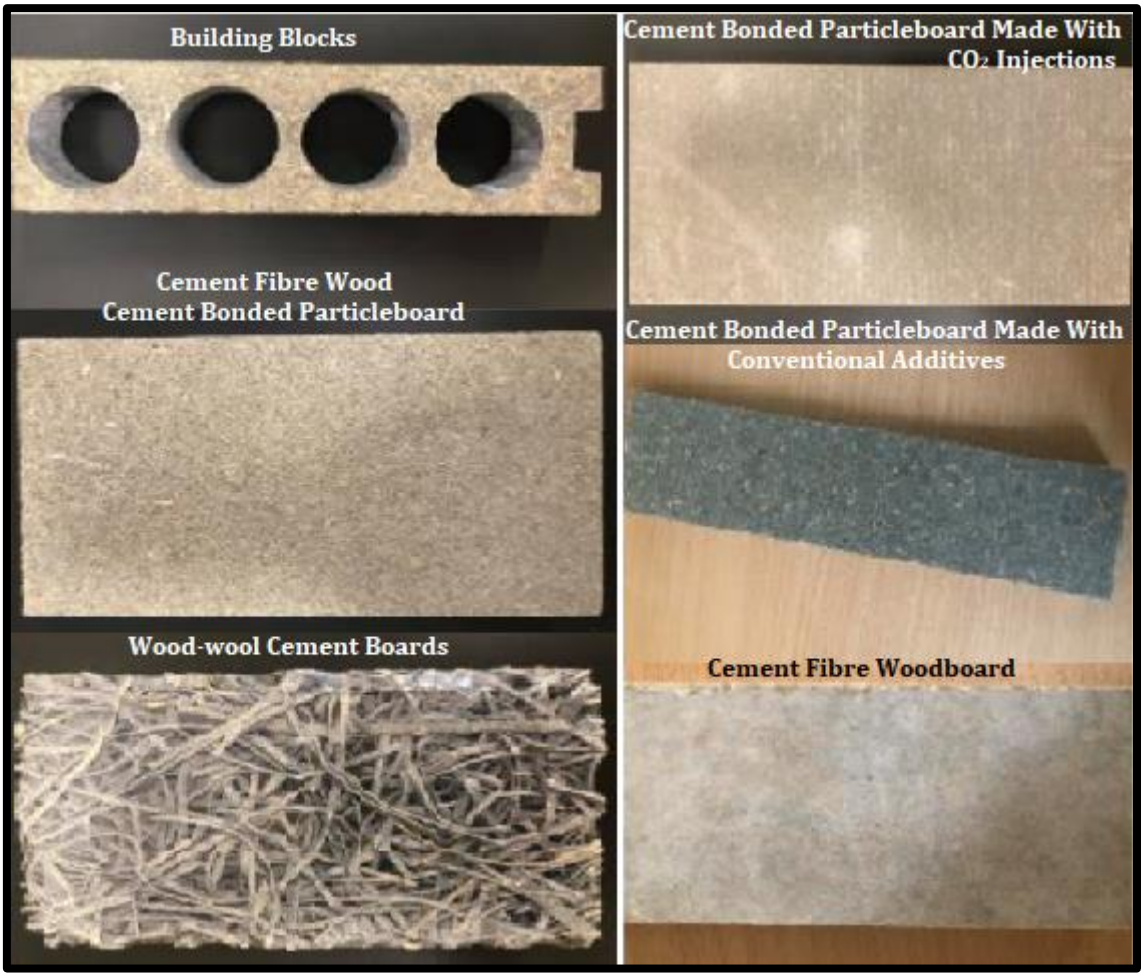

Fig. 1. Wood-cement composite types used in the application (Brahmia et al., 2020).

Although up to 2% waste is generated during the processing of wood, very few of them are used as recycling in chipboard production (Ateş, 2018). With the applied standards, it is seen that various composite building materials researches are increased in order to take advantage of the wood such as insulation. Researches on

the use of these products as insulation materials, especially since they are not flammable, are still up-to-date. Unlike these studies, the negative effect of high temperature on the mechanical properties of cement-bonded wood composites was investigated in this study. For this purpose, specimens produced with different sawdust-cement ratios were exposed to temperatures reaching 400°C, and losses in physical and mechanical properties were determined.

2. Experimental Study

2.1. Materials

Sawdust, which are the waste of a firm that carries out woodworks, were used in the study. The type of wood used is the baked Russian pine, called north Saphire 117, taken from the Siberian region. The sawdust shown in Fig. 2 appeared during timber production. The unit weight of the chips is found as 230 kg/m^3 and its granulometry is given in Table 1. As mixing water, mains water which property is given in Table 2, is used. CEM I.42.5 R Portland cement, the properties of which are given in Table 3, was used as binder.

Fig. 2. The sawdust used in the production of cement-bonded composite.

Table 1. Granulometry of sawdust.

Sieve size, mm	4	2	1	0.5	0.25
Granulometry, %	100	99.5	88.7	44.9	15.2

Table 2. Properties of mixing water

Chemical Property, mg/l						Physical property	
Al	0.04	Cu	0.016	Ni	5,07	Conductivity, µS/cm	628
NO_3	11.1	Fe	0.007	K	6,8	Hardness, Fd^0	30.11
NH_4	0.06	Mn	0.015	As	1,19	pH	7.35

Table 3. Properties of cement

Chemical properties				Physical properties	
SiO_2	19.2	K_2O	0.63	Density, g/cm^3	3.09
Al_2O_3	4.56	Na_2O	0.31	Specific surface cm^2/g	3190
Fe_2O_3	3.09	SO_3	3.21	Setting Time(initial), min	163
CaO	62.9	CI-	0.01	Setting Time(final), min	228
MgO	1.88	LOI	3.8	Soundness, mm	1

2.2. Method and tests

The sawdust was used as filler in cement-bonded wood composite production. Water-cement ratio was kept constant at 0.50 in production. Three different mixtures were made with a sawdust-cement ratio of 0.4, 0.8 and 1.25. 4x4x16 cm prismatic specimens were taken from the produced composite mixtures and removed from the mold after 1 day and placed in a standard curing environment. Some of the specimens that gained their strength for 28 days were kept at 200°C and some were kept at 400°C for 3 hours after the oven reached the desired temperature. Left to cool at room temperature. Unit weight, ultrasonic pulse, bending and compressive tests were carried out on the specimens. Also, at least 3 specimens were used for each test. The three-point bending test is carried out in accordance with TS EN 196-1. Specimens that are divided into two parts in the bending test are tested for compressive strength. Compressive strength test was carried out on these parts by using 4x4 cm^2 metal plates. According to the TS EN 12504-4 Standard, it is based on the determination of the transition

times of the ultrasonic sound waves generated between the receiver and the transmitter in the specimen. The unit weight was calculated according to TS EN 12390-1 by dividing the specimen weight by volume. Cement-sawdust mixtures and compressive test were shown in Fig. 3. Since the wood becomes charred at temperatures above 280 degrees (Vural, 2013) and loses its properties, the temperature before carbonization was chosen as 200°C, and the temperature after carbonization was 400°C.

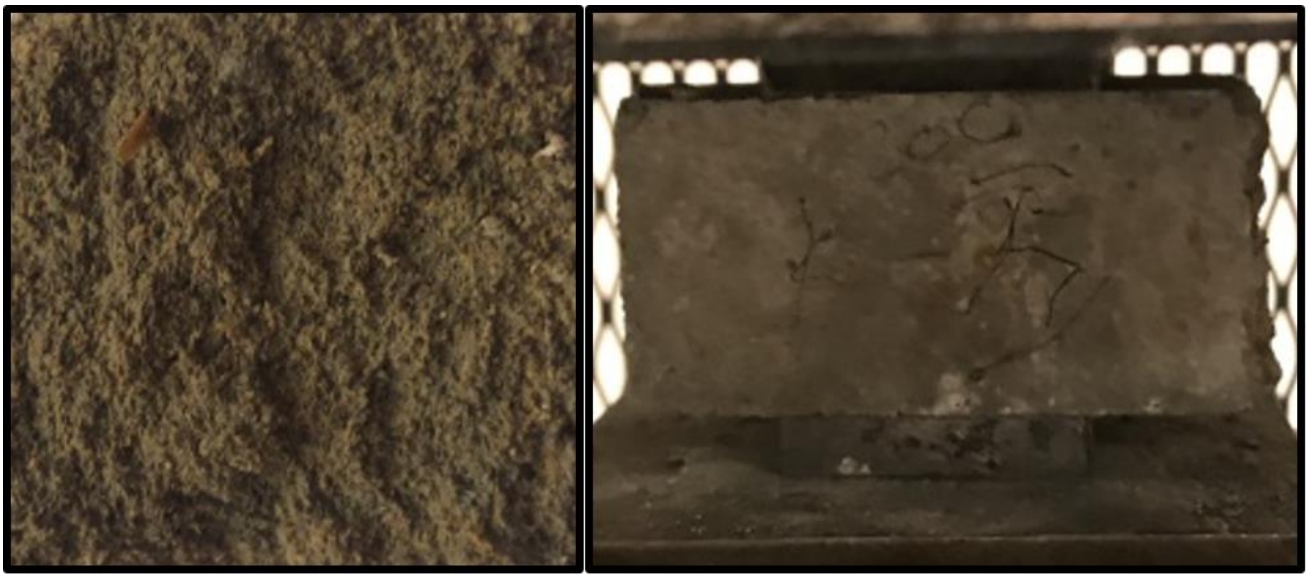

Fig. 3. Cement-bonded wood mixtures and compressive test.

3. Results and Discussion

Unit weight test results were given in Fig. 4. As the sawdust-cement ratio decreased, the unit weights increased by 6%. Similar to other studies (Oliveira et al., 2020), it can be stated that a very light composite is obtained since the unit weights of the specimens are around 1.3 kg/dm^3. Depending on the evaporation of the water contained in the specimens kept at a temperature of 200°C, losses were observed in the rates up to 2% in unit weights. When the temperature reached 400°C, unit weights decreased at the rate of low sawdust-cement by 7.4% while this decrease rate was 4.3% at the rate of high sawdust-cement. It can be said that the reason for the relatively higher losses in unit weight at 400 °C is carbonization (Vural, 2013) of the sawdust by partial burning.

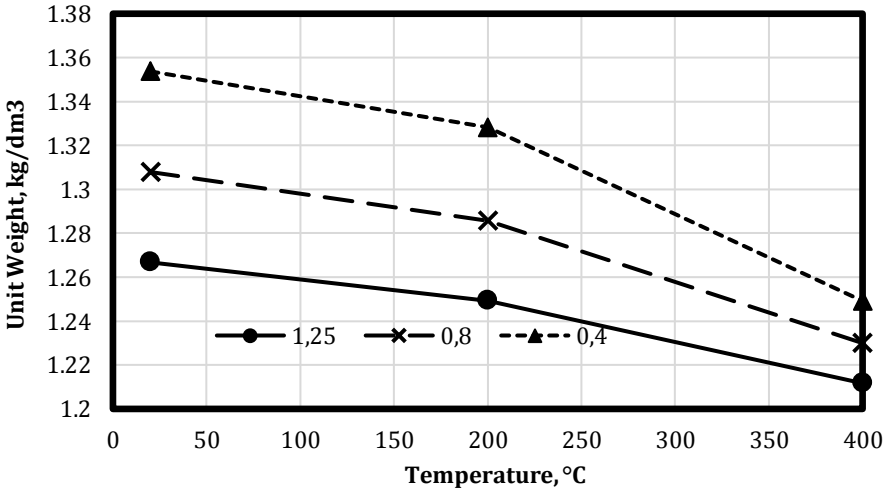

Fig. 4. The effect of high temperature on unit weights of composite specimens.

Ultrasonic pulse velocity losses occurring under the influence of high temperature were shown in Fig. 5. As shown in Fig. 3, when the sawdust-cement ratio increased, ultrasonic pulse velocity decreased by 14%. Increasing the amount of sawdust causes gaps to increase. In addition, since the hardened cement paste and sawdust create different media, the transmission of the vibration movement is slower in the sawdust, resulting in the reduction of the ultrasonic pulse velocity. When the temperature increased from 20°C to 200°C, micro cracks caused by the evaporation of water trapped in the interior and the application of pressure caused a decrease in the rate

of ultrasonic pulse velocity reaching 13%. When the temperature was 400°C, sawdust was partially burned and the gases formed as a result of this burning applied pressure to the inner walls, as a result of the propagation and branching of micro-cracks that occurred earlier, caused a decrease in the ultrasonic pulse velocity reaching 67%.

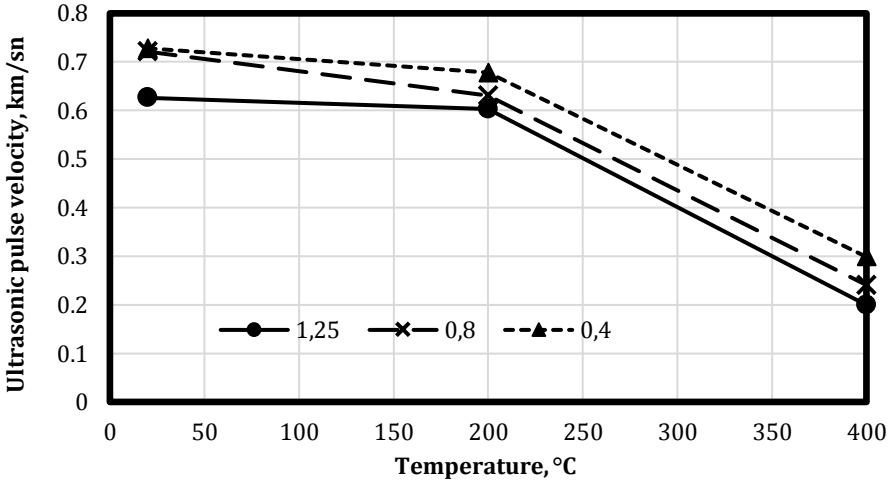

Fig. 5. Ultrasonic pulse velocity rate change of composite specimens with high temperature.

Variation of bending strength with temperature and sawdust-cement ratio were shown in Fig. 6. The increase in the sawdust content of the composite caused the bending strength to decrease by 13%. Since Sawdust is in powder form and not long enough to form a fibrous structure, it did not affect bending strength positively. In addition, sawdust being less rigid than cement caused decreases in bending strength. With increasing ambient temperature, bending strength decreased linearly. The rate of decrease has reached 25%. Micro cracks caused by dehydration and burning can be cited as the reason for these significant decreases in bending strength.

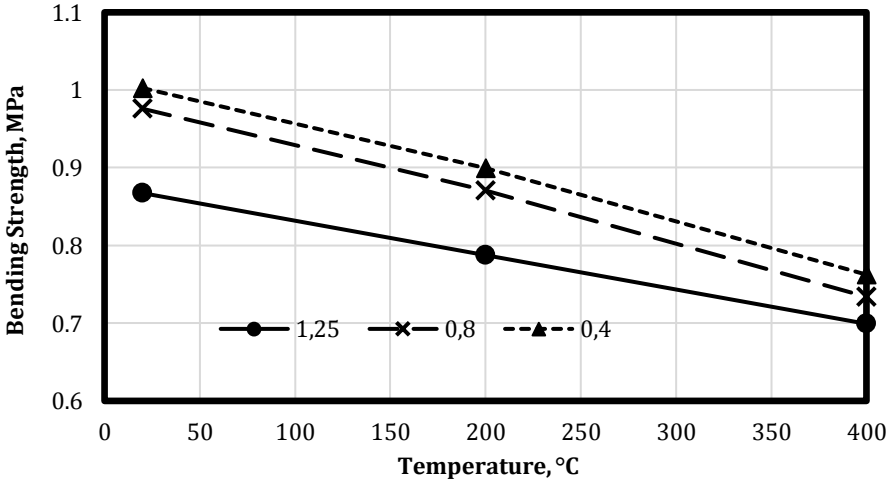

Fig. 6. Effect of high temperature on bending strength of composite specimens.

Compressive strength test results on cement-bonded wood composite specimens were shown in Fig. 7. Strengths were determined to be below 10 MPa, similar to other studies in the literature (Oliveira et al., 2020). İllustrated in Fig. 7. When the sawdust-cement ratio increased from 0.4 to 0.8, the compressive strength decreased by 7%. When the sawdust-cement ratio reached 1.25, compressive strengths remained nearly the same. When the effect of high temperature on compressive strength is examined, compressive strength has decreased due to the increase in temperature. When the temperature reached 400°C, specimens with sawdust-cement ratio of 0.4 experienced 23% strength loss. When the sawdust-cement ratio is 0.8, the strength loss is 25%, while when the sawdust-cement ratio reaches 1.25, the strength loss has reached 26%. Sawdust is being more viscous than cement and lack of binding properties caused a decrease in strength in specimens where sawdust was high. $Ca(OH)_2$, which is a hydration product with high temperature in cementitious structures, loses water and turns into CaO, causing shrinkage and cracks. This situation shows that sawdust is effective in the decrease in strength together with the inward burning. The high residual strengths can be interpreted as the deterioration of calcium silicate hydrate gels, which are among the hydration products and provide a solid structure, has not yet started.

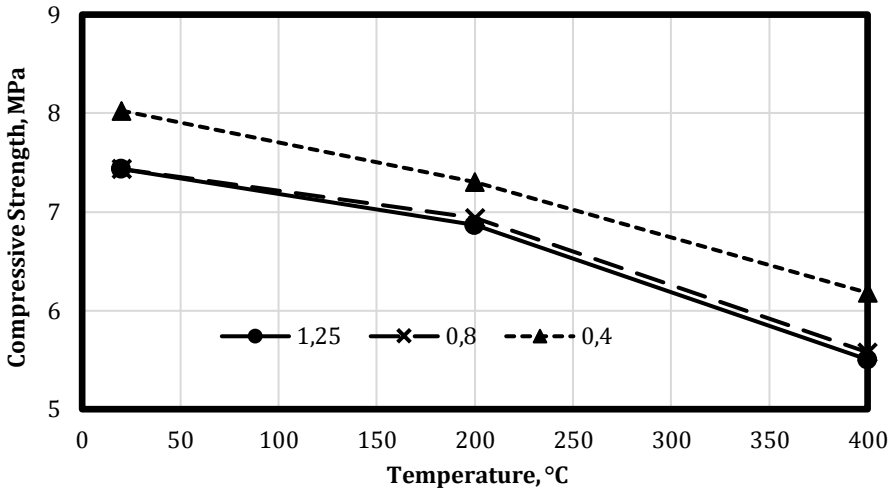

Fig. 7. Compressive strength variation of composite specimens with high temperature.

During the reactions of the main components of cement with water, they interact with components such as cellulose and lignin in the sawdust structure and dissolve in alkaline environments caused by Ca (OH)2. Although more than one reaction occurs at the same time, the formation of hydrogen bridges between cement and sawdust is primarily effective on the bond. Due to the large number of hydroxyl groups in Sawdust's structure, the strength of the composite matrix largely depends on its hydrogen binding potential. Fig. 8 shows the bond structure of sawdust and cement (Şahin et al., 2019).

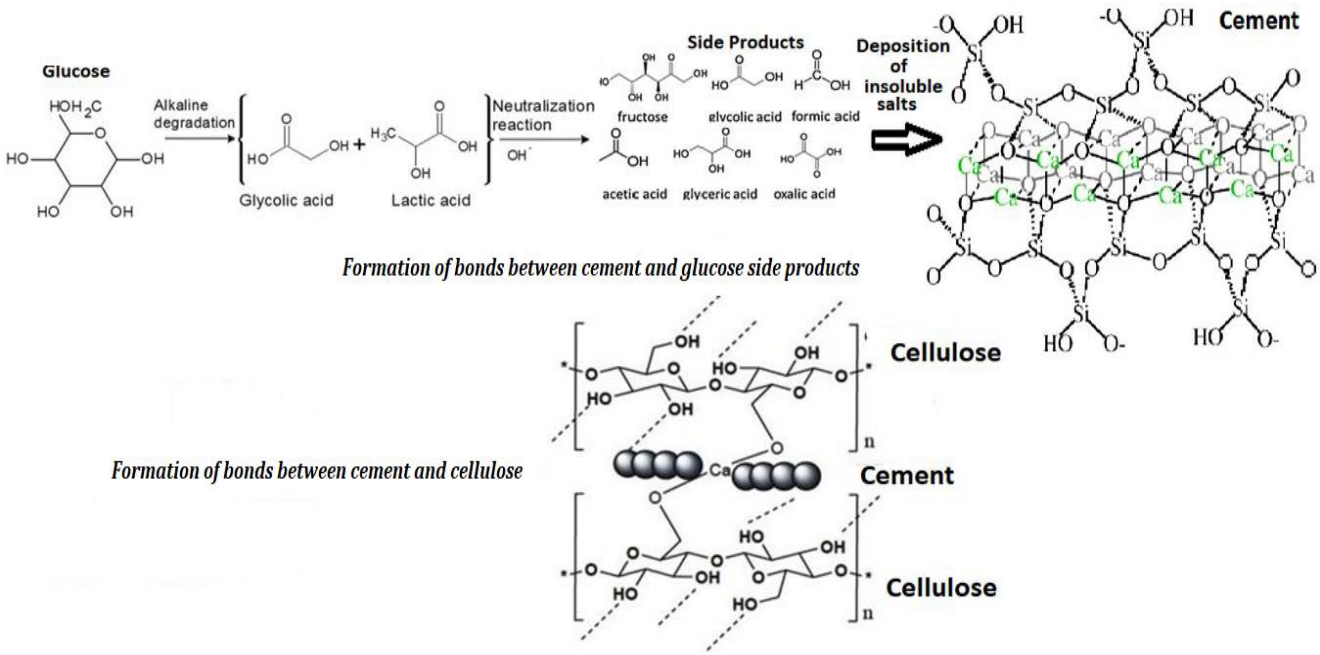

Fig. 8. Chemical structures of cement-bonded wood composite.

4. Conclusions

The following results have been achieved with the experimental study conducted:

- The unit weights of the produced cement-bonded wood composites were found to vary between 1.26-1.36 kg/dm^3, ultrasonic pulse velocity of 0.6-0.8 km/sec, flexural strengths of 0.8-1 MPa, and compressive strengths of 7-8 MPa. The values found indicate that a fairly light block can be produced for masonry structures or partition walls with this material or this material can be used for insulation purposes by turning it into a plate. Especially when considering strength, sawdust-cement ratio is recommended as 0.4.
- When the properties that remained under the influence of high temperature were examined, it was observed that the unit weights decreased by 7% and dropped to 1.21 kg/dm^3. It is noteworthy that ultrasonic pulse velocity decreased to 0.2 km/sec and decreased by 0.7 MPa with a loss of 25% in flexural strength. In addition, it was observed that the com-

pressive strength losses reached 26%, and the remaining strength decreased by 5.5 MPa. Despite the decreases in physical and mechanical properties, it shows that the specimens do not disintegrate at high temperatures such as 400°C and residual strengths still do not lose their carrier properties. It is recommended to use cement-bonded wood composite products, especially because of the insufficient high temperature and fire performance of composite products produced using sawdust-resin. When residual strengths were examined, it was found that the optimum sawdust-cement ratio was 0.4.

- Wood is one of the most widely used building materials with its wide usage area. Recycling of waste generated during wood processing is not sufficient. With this study, an alternative field is proposed for the evaluation of these wastes. Thus, products with sufficient mechanical properties can be produced for the structure. However, it is recommended to investigate other durability properties that can disrupt the cement structure, especially for cement-bonded wood composite. In addition, it is recommended to investigate the changes in the mechanical and physical properties of this product when used at temperatures above 400°C.

REFERENCES

Aras U, Kalaycıoğlu H (2016). Wood Based Composites and Usage Areas. *International Refereed Journal of Engineering and Science*, 120-136.

Ateş E (2018). Determination of the amount of the waste wood dust and its energy value in the city center of Balıkesir. *Technological Applied Sciences*, 13(4), 329-346.

Berger F, Gauvin F, Brouwers HJH (2020). The recycling potential of wood waste into wood-wool/cement composite. *Construction and Building Materials*, 260, 119786.

Brahmia FZ, Horváth PG, Alpár TL (2020). Effect of pre-treatments and additives on the improvement of cement wood composite: a review. *BioResources*, 15(3), 7288-7308.

Campbell FC (2010). Structural Composite Materials. ASM International, 612 p., USA.

Caprai V, Gauvin F, Schollbach K, Brouwers HJH (2018). Influence of the spruce strands hygroscopic behaviour on the performances of wood-cement composites. Construction and Building Materials, 166, 522-530.

Gauvin F, Kochova K, Caprai V, Schollbach K, Brouwers HJH (2019). Study of different spruce strands and their effect on the properties of wood-cement composites. *Academic Journal of Civil Engineering*, 37(2), 37-41.

Hossain MU, Wang L, Iris KM, Tsang DC, Poon CS (2018). Environmental and technical feasibility study of upcycling wood waste into cement-bonded particleboard. *Construction and Building Materials*, 173, 474-480.

Kaya Aİ (2018). Some wood based composite materials. Turkchem News Portal. http://www.turkchem.net/ahsap-esasli-bazi-kompozit-malzemeler.html Downloaded on 26.07.2020

Kochova K, Caprai V, Gauvin F, Schollbach K, Brouwers HJH (2020). Investigation of local degradation in wood stands and its effect on cement wood composites. Construction and Building Materials, 231, 117201.

Li M, Nicolas V, Khelifa M, El Ganaoui M, Fierro V, Celzard A (2019a). Modelling the hygrothermal behaviour of cement-bonded wood composite panels as permanent formwork. *Industrial Crops and Products*, 142, 111784.

Li M, Khelifa M, Khennane A, El Ganaoui M (2019b). Structural response of cement-bonded wood composite panels as permanent formwork. *Composite Structures*, 209, 13-22.

Oliveira CA, Silva JV, Bianchi NA, Campos CI, Oliveira KA, Galdino DS, Bertolini MS, Morais CAG, Souza AJD, Molina JC (2020). Influence of Indian cedar particle pretreatments on cement-wood composite properties. *BioResources*, 15(1), 1656-1664.

Sanaev VG, Zaprudnov VI, Gorbacheva GA, Oblivin AN (2016). Factors affecting the quality of wood-cement composites. *Bulletin of the Transilvania University of Brasov*. *Forestry, Wood Industry, Agricultural Food Engineering. Series II*, 9(2), 63.

Şahin HT, Kaya Aİ, Yalçin ÖÜ, Kilinçarslan Ş, Şimşek Y, Mantanis Gİ (2019). A study on the production process and properties of cement-based wood composite materials. *The Journal of Graduate School of Natural and Applied Sciences of Mehmet Akif Ersoy University*, 10(2), 219-228.

TS EN 196-1 (2016). Methods of testing cement - Part 1: Determination of strength. Turkish Standardization Institute, Ankara, Turkey.

TS EN 633 (1999). Cement-Bonded particleboards- Definition and classification. Turkish Standardization Institute, Ankara, Turkey.

TS EN 12390-1 (2013). Testing hardened concrete - Part 1: Shape, dimensions and other requirements for specimens and moulds. Turkish Standardization Institute, Ankara, Turkey.

TS EN 12504-4 (2012). Testing concrete - Part 4: Determination of ultrasonic pulse velocity. Turkish Standardization Institute, Ankara, Turkey.

Vural S (2013). Species of charcoal used in Konya region and its effects on charcoal quality. *M.Sc. thesis*, Süleyman Demirel University, Isparta, Turkey.

Wang L (2018). Value-added recycling of construction waste wood into eco-friendly cement-bonded particleboards. *Ph.D. thesis*, Hong Kong Polytechnic University, Hung Hom, Kowloon, Hong Kong.

Yel H, Cavdar AD, Torun SB (2020). Effect of press temperature on some properties of cement bonded particleboard. *Maderas. Ciencia y tecnología*, 22(1), 83-92.

Challenge Journal of Structural Mechanics

Research Article

Study on slope stability of frame prestressed anchor sheet pile wall with finite element strength reduction method

Amna Saeed Al-Banaa [a,*], Zhou Yong [a]

[a] *Department of Civil Engineering, Lanzhou University of Technology, Lanzhou 730050, China*

ABSTRACT

Slope stability analysis is performed in practical geotechnical engineering using the finite element method, which is an advanced method and is widely used by engineers. With the development of computer technology, it has become easy to study the slope's stability supported by frame prestressed anchor and sheet pile wall through the displacement-based finite element numerical analysis method, to calculate the safety factors. However, the expansion angle ψ' is not widely covered. In this study, PLAXIS two-dimensional finite element method is using to establish the slope model supported by frame prestressed anchor and sheet pile wall, and the influence of expansion angle on slope deformation is studied. The results show that the expansion angle has a different effect on the convergence of the two-dimensional slope model. In the model slope, a prestressed frame anchor and sheet pile wall reinforce the slope. The failure mechanisms were unclear when $\phi' = \psi'$ (flow base). Besides, when the slope has high soil strength parameters (c' or φ'), the expansion angle will affect the calculation results and convergence. In general, the expansion angle significantly influences the slope's stability and is not affected. Therefore, it was necessary to note the effect of the angle of expansion on stability.

ARTICLE INFO

Article history:
Received 26 September 2020
Revised 31 October 2020
Accepted 10 December 2020

Keywords:
Sheet pile wall
Prestressed anchors
Safety factor
Dilatancy angle
Finite element method

1. Introduction

Slope stability analysis is a hot issue that scientists have debated since the advent of geotechnical engineering (Griffiths and Marquez, 2007). Research on slope stability and prevention of landslides has become a very important topic in geotechnical engineering. In addition, due to the regional limitations of slopes, complexity of geotechnical materials and diversity of surrounding environmental conditions; transition from the stable to the unstable, and from the hazardous state to the landslide become very complex. Therefore, how to accurately analyze and study rocks and soils requires detailed research. Soil slope stability and precise determination of landslide are the subjects of historical research (Davis, 1968; Griffiths, 1999).

When studying slope stability, several methods can be used to assess the ramp safety factor. The marginal equilibrium analysis (LE) provides values for FS on the predetermined failure surface of the circular roof (Bishop, 1955; Morgenstern and Price, 1965). The slope considers itself as a solid body with the force determined by the Mohr-Coulomb parameters and *c*. Due to the determination of its strength to the nature, the fault surface corresponding to the lowest constant service level is repeatedly determined. However, this does not guarantee that the solution represents a sliding surface with the slightest safety factor. The upper and lower limits of energy balance and static equilibrium are estimated by boundary analysis (LA). With the help of the finite element method (FEM), even for complex problems (Lyamin and Sloan, 2002a; 2002b); these limits can be determined (Sulsky et al., 1995) as well as inserted instability analysis (Zabala and Alonso, 2011). Slope stability is measured by analysis of slope stability using the finite element method. There are several methods for the assessment of a safety factor. The surface fault corresponding to the minimum fixed service is determined in an iterative manner. In the finite element method, stability of the slope is determined by force.

* *Corresponding author*. Tel.: +86-189-190-33010 ; E-mail address: eng_amna20000@yahoo.com (A. S. Al-Banaa)
ISSN: 2149-8024 / DOI: https://doi.org/10.20528/cjsmec.2021.01.006

Nomenclature

Ψ	The volumetric expansion angle
ψ'	Dilatancy angle
φ	Angle of friction
φ'	Effective friction angle
c	Soil cohesion coefficient
γ	Unit weight
ν	Poisson's ratio
E	Young's modulus
FoS	Factor of safety

The reduction method (SR) was developed by (Zienkiewicz et al., 1975). They combined it with the Mohr-Coulomb model. After, Tschuchnigg et al. (2015) carried out extensive research on this problem, including the refinement of finite element mesh and the elastic-plastic flow rule. Further modifications of SR can also be found in Tschuchnigg et al. (2015). It is essential to combine staged structural modeling and stability analysis without using other tools while preserving variable stress and history. Even if the Mohr-Coulomb model can predict the stress state.

When failure occurs, the results of predicting the stress response are not ideal. The foundational modeling theories of advanced elastomeric plastics, such as compact surface plasticity and other modeling frameworks of Dafalias (1986), including Under Plastic Woo and Columba's (Wu and Kolymbas, 1990) and the Odyssey Columba's Bar (Kolymbas, 2012), were directed in order to overcome these difficulties.

Suggested, these models were further refined to capture the stiffness of niemonis, anisotropy or viscosity by Jerman and Mašín (2020). These models can consider not only the nonlinear strain response of soil but also the state and load history dependence of soil. However, methods of reducing the strength of these models are not often feasible. Therefore, if an advanced foundation model is to be used in the staging construction and stability analysis is required, the parameters must be recalibrated. The M-C model must be used.

However, if it is assumed that ψ'=0°, the following two main factors should be taken into consideration. First, the worst case is considered in the numerical analysis to obtain a low *FoS* (Manzari and Nour, 2000; Hang and Ping, 2012; Kumar, 2004). In addition, in the second case, when the soil is sheared, ultimately small (constant volume) the plastic volume of soil changes. In contrast, soil strength is overestimated when relevant flow rules are applied. This leads to overestimation and insecurity of *FoS* (Michalowski, 2002; Manzari and Nour, 2000). However, the role of ψ' is rarely discussed. Until recently, only a few researchers considered the swelling soil effect (Li et al., 2010; Griffiths and Marquez, 2007; Zienkiewicz et al., 1975). Therefore, this study takes 2D frame prestressed anchor sheet pile wall as the research object and uses the PLAXIS two-dimensional finite element method to study the influence of expansion angle.

2. Calculation of Strength Reduction Factor by the Mohr-Coulomb Model

The M-C model's stress state is limited in the principal stress space by the yield surface *F* of the hexagonal cone. Since M-C is an elastic-plastic complete plastic model, once the loading path reaches the stress state on the yield surface, the model will show a plastic strain response. At the integration point, the strength parameters decrease from the initial values of φ_1 (internal friction angle) and c_1 (cohesion) to their corresponding φ_2 and c_2, which directly reduces the size of yield surface *F*. These results in lower deviation *Q* and average stress *P* at the limit state, as shown in Fig. 1(a).

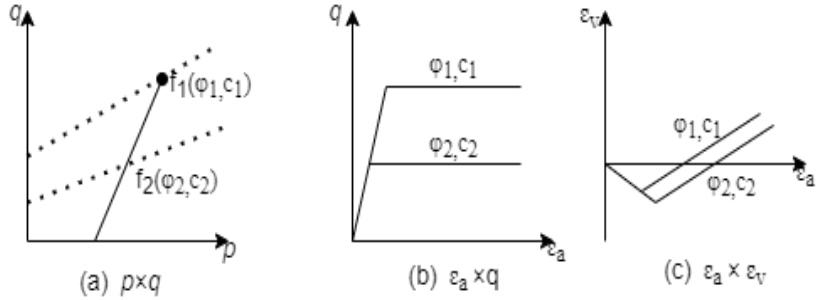

Fig. 1. Impact of force reduction on the M-C of the 3-axis dried stress.

The limit state is represented by a continuous excessive axial deformation ε_a, as shown in the Fig. 1(b). The volume strain ε_v in the limit as shown in the Fig. 1(c), state depends on the so-called flow rule controlled by the dilatancy parameter ψ. When the test stress state appears outside the yield surface, the stress recovery relies on the plastic deformation's consistent condition. In the finite element method, the strength parameters of each reduction step are evaluated as:

$$\tan \varphi_r = \frac{\tan \varphi_0}{FR} \tag{1}$$

$$c_r = \frac{c_0}{FR} \tag{2}$$

FR is the reducing factor, and the 0 and *r* which represent the initial and reduced value of a parameter, respectively. The reduction of the force coefficients finally reaches the limit state. In the finite element simulation, once the analyzer is unable to find a solution to the unbalanced force resulting from a further decrease in the material's strength, it is seen as reaching the bound state. It should not be considered that the iterative process of finding equilibrium is associated with excessive

deformation of the shear region. In any case, this deformation has no physical significance related to the reduction of the artificial force. However, the resulting displacement indicates the location of the potential shear regions. Then *FS* is calculated as:

$$FS = \frac{\tan \varphi_0}{\tan \varphi_f} = \frac{c_0}{c_f} \quad (3)$$

This means that the *FS* equation is equal to the *FR* (Eqs. (1 and 2)). The symbol *f* in Eq. (3) represents the parameter value at the time of failure. It should be not that M-C parameters can be chaos as φ>0 and *c*>0 to represent the peak state, or φ 0 and *c*=0 to predict the critical state, depending on the soil condition in the slope analyzed. Also, the behavior of the M-C model is determined by two additional parameters: Young elastic Stiffness *E* and Poisson's ratio *v*.

3. Numerical Modeling Procedure

3.1. Main parts of the prestressed anchor bar and sheet pile wall

The prestressed anchor sheet pile wall structure is mainly composed of a reinforced concrete, prestressed anchor rod, and sheet pile wall. The free part of the prestressed anchor cable is embedded in the filler and passed through the potential sliding surface, as shown in Fig. 2 the anchorage section is located in the soil, the anchor supporting structure, and the anchor head plate wall. The ground pressure load acts on the supporting system of the prestressed anchor cable wall. The external force through the anchorage section is transferred to the free area of the pile. The anchor's strength can maintain the stability of the pile sheet wall structure.

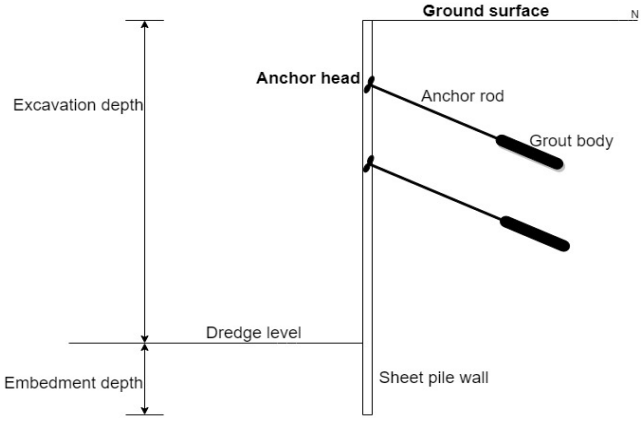

Fig. 2. Structure of the prestressed anchor bar and sheet pile wall.

3.2. Non-associated plasticity

Davis (1968) noted that only when a material has a corresponding flow law is the plastic field's stress and velocity properties. If it is $\varphi' \neq \psi$, he suggested using the force reduction parameters, c^* and φ^*, and flow rules applied in the model:

$$c^* = \beta \cdot c' \quad (4)$$

$$\tan \varphi^* = \beta \cdot \tan \varphi' \quad (5)$$

$$\beta = \frac{\cos \psi' \cos \varphi'}{1 - \sin \psi' \sin \varphi'} \quad (6)$$

Therefore, c^* and φ^* are used as input parameters in all analyzes called Davis methods.

The background of Here is a detailed strength reduction parameter. Fig. 3(a) shows an ABCD element tilted perpendicularly at an angle. The basic principle of stress and tension is also explained. It was assuming that it is coaxial and that the axes are congruent. Fig. 3(b) shows the Mohr stress circuit for a given case, where the daily pressure σ_s', the shear pressure is the stress ratio, and the failure criterion determined according to the Coulomb model.

$$\tau_s = c + \sigma_s' \tan \varphi' \quad (7)$$

The point PP on the stress circle represents the pole of the plane. Therefore, when drawing lines from PP to points (I) and (II), the stress σ'_s is found and τ_s the direction of the plane in which *s* acts. According to Davis (1968), the lines representing these directions are called the characteristic pressure lines, which is uniformly distributes in the order of the central pressure at an angle of 45°-$\varphi'/2$.

Fig. 3(c) shows the case of Mohr strain circle, where δ_{ε_1} and δ_{ε_3}. It represents the primary and secondary principal strain increments, and the increment of shear strain $\delta_{\gamma}/2$.

The expansion angle ψ can be defined if the level stress condition is assumed as follows:

$$\sin \psi' = \frac{\delta \varepsilon_{vo1}}{\delta_{\gamma max}} = \frac{\delta \varepsilon_n}{\delta_{\gamma max}} = \frac{\delta \varepsilon_1 + \delta \varepsilon_2}{\delta_{\gamma max}} \quad (8)$$

where $\delta_{\varepsilon_{vo1}}$ is the volumetric stress, and $\delta_{\gamma max}$ corresponds to the maximum shear stress. The points (I) and (II) represent the points of zero direct pressure increase (δ_{ε_n}=0) and the direction in which he called δ_{ε_n}=0 empty extension lines (Kumar, 2004). When drawing lines from *Pp* to points (I) and (II), the direction of the planes perpendicular to zero is found. Thus, when drawing the horizontal lines from (I) and (II) and connecting the intersection point to the Mohr strain circuit with *Pp*, the direction of the zero extension lines is found (Davis, 1968). Assumed that the extension lines of the zero represent slip lines, or in other words, velocity characteristics (Roscoe, 1970). This assumption was firstly proposed based on experiments. These velocity properties are eliminated evenly around the principal stress direction (strain), but at 45°-$\varphi'/2$. As a result, the stress properties are sliding lines only if Fig. 4(a) of the element ABCD. Fig. 3(a) represents each characteristic of stress and speed. If stability analyzes are performed based on assumed velocity characteristics (slip lines), then the ratio of actual stress should be applied to the zero extension lines rather than the proportion of stress to harmonic stress properties. The Mohr stress circuit (Fig. 4(b)) shows that shear stress τ_k and normal stress

$\sigma_{k'}$ do not reach the Mohr-Coulomb criterion. Based on these considerations. Davis (1968) proposed the use of c^* and φ^* as an effective grip angle and effective angle of friction, respectively, at sliding planes in combination with a bound flow base. The difference between φ', φ^*, c' and c^*, respectively, is illustrated in Fig. 4(b).

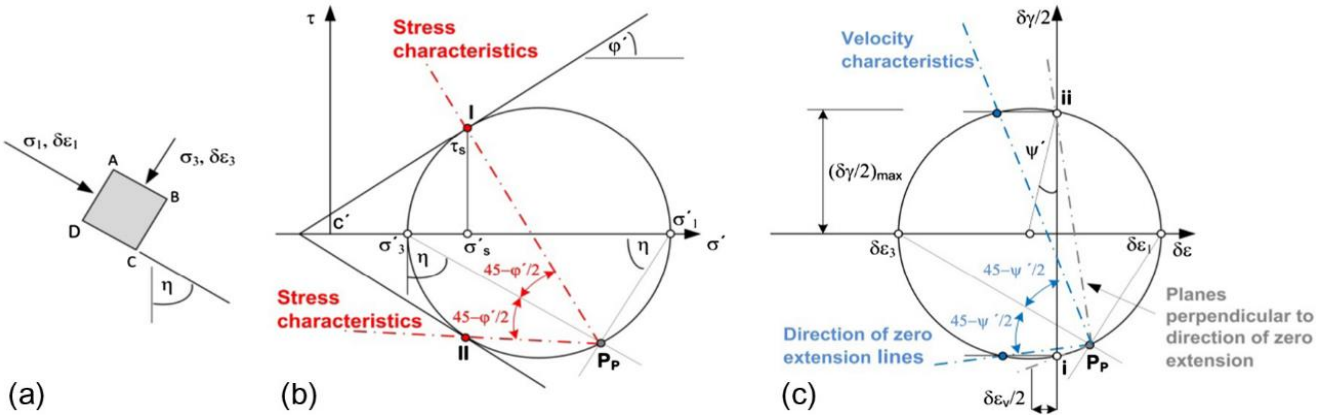

Fig. 3. (a) Considered element; (b) Stress circuit Mohr; (c) Dynasty circle Mohr.

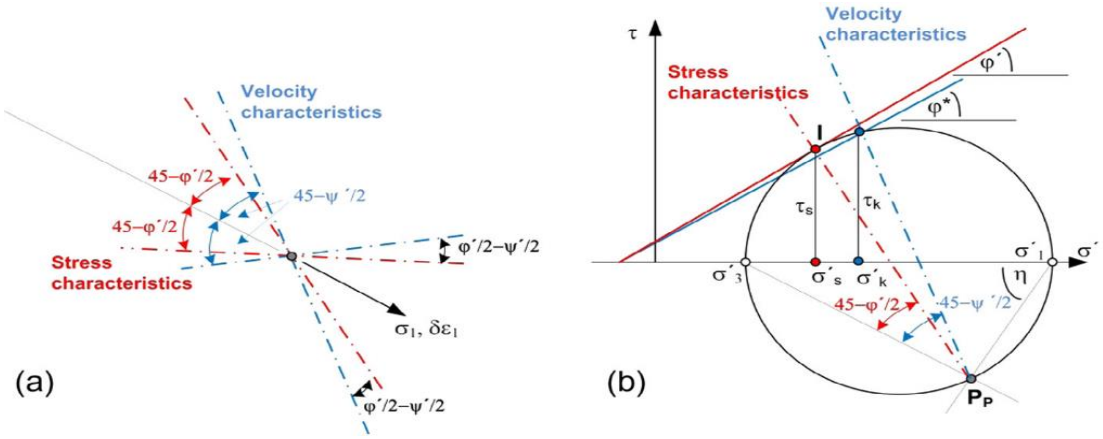

Fig. 4. Stress properties (a) with velocity (b).

3.3. Anchor bar and sheet pile wall and soil profiles

Using PLAXIS 2D software in numerical simulations. FoS safety factor was found .The analyzed results were analyzed by comparing the literature results for compatibility in three aspects: network roughness, expansion angle, and failure mechanism. In addition, after confirming that the results are reasonable and acceptable, the same as (Griffiths and Marquez, 2007). Use SRM to discuss the effects of boundary conditions, such as the geometry of the dam and the topography of the valley site, in 3D models. (Zienkiewicz et al., 1975). Parameters of throughput, including numerical calculation non-convergence, entry of plastic region, and displacement salinity at a given characteristic point, we are used to examining the *FoS* contrast ABAQUS and FLAC3D. Measures were used for the FEM model and expanded to include a pre-framed stabilizer bar and a laminate stack wall using PLAXIS 2D. Since the *FoS* was considered reasonable, The influence of the expansion angle on convergence direction discussed using different parameters (grid roughness, boundary conditions, slope angle, and soil parameters). Table 1 presents the main model parameters of an anchor framed with a sheet pile wall and Table 2 presents the soil parameters in 2D slope model.

Table 1. Main model parameters of an anchor framed with a sheet pile wall.

Items	Model	*EA* (kN/m)	*EI* (kN/m²)
Anchor	Elastic	5*106	-
Sheet pile wall	Elastic	7.5*106	1.0*106
Plate	Elastic	7.5*106	1.0*106

Table 2. Soil parameters in 2D slope model.

Parameter	Value
φ'	45°
c'	6 kPa
Ψ'	0°, 5°, 10°, 15°, 35°, 45°
E'	$1*10^5$
γ	20.20
υ	0.3

3.4. Calculations

According to the relevant flow rules, the *FoS* obtained from LAM and SRM are very close (Baker et al.,

2006). Likitlersang et al. (2018) used SRM to discuss the stability and deformation characteristics of high-speed railway embankments built on soft clay in Bangkok. The results show that most of the existing railway embankments show a greater degree of movement under a load of high-speed trains. (Cai et al., 2002) used SRM to compare the boundary effects between two-dimensional and three-dimensional models and showed that the assumed boundary conditions in the z-plane (thickness direction) are critical for three-dimensional finite element analysis, and if roller-roller Column conditions, the effect of z-direction length can be ignored. The results of ABAQUS were slightly higher than that of FLAC3D (2-4%) in the same yield. In addition, they point out that different software has different fusion standards, resulting in different FoS. Fig. 5 shows an example of a framed prestressed anchor bar and sheet pile wall.

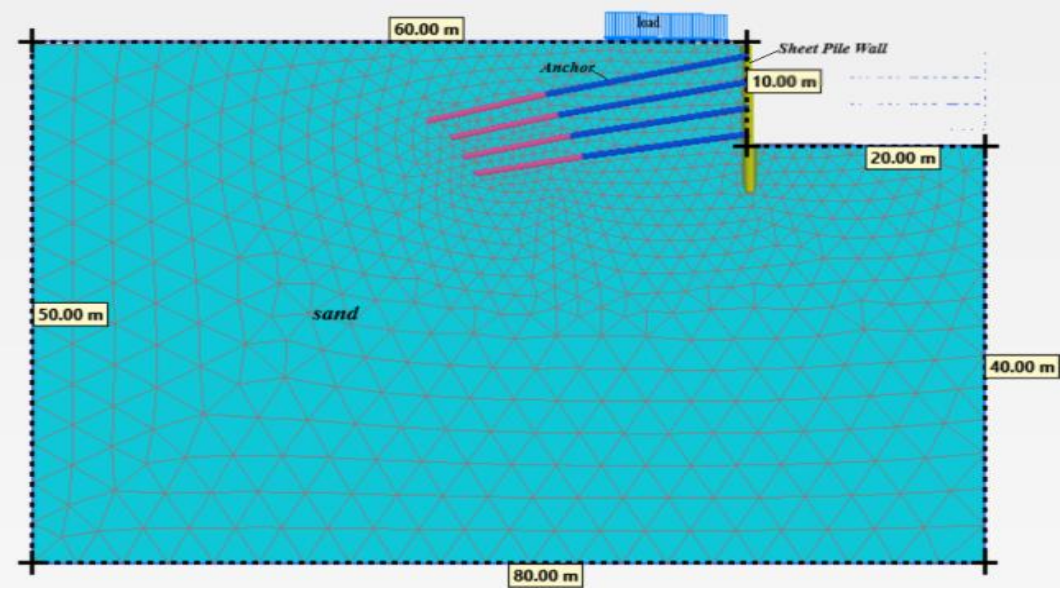

Fig. 5. An example of a framed prestressed anchor bar and sheet pile wall.

The SRM method has been used extensively in finite element geotechnical projects.

FoS solutions are integrated with SRM solutions and are a professional geotechnical specification. It was used in this study. Currently, the location of the failure surface is monitored using three standard methods, namely, joint displacement (Dafalias, 1986), plastic area (Griffiths and Marquez, 2007; Lim et al., 2015; Tschuchnigg et al., 2015) and shear stress region. As shown by Roscoe (1970) (Wu and Kolymbas, 1990), it is observed that the surface of the pores corresponds to the part of failure shear stress observed from the laboratory results.

In this study, the shear stress region is used to this monitor the position of the failure, and to compare the failure mechanisms for each of the expansion angles (ψ' = 0˚, 5˚, 10˚, 15˚, 35˚, 45˚).

4. Analysis and Results

The safety factor was checked using soil parameters and finite element method were applied to find results, a framed prestressed anchor bar and sheet pile wall for the reinforcement have been added. Fig. 1 shows an example of a framed prestressed anchor bar and sheet pile wall, and the main model parameters of an anchor framed by a wall of sheet pile are shown in Table 1, soil parameters are clarified in Table 2.

In this study, the plasticity theory was fully applied from the Mohr-Coulomb. In addition, a framed prestressed anchor bar and sheet pile wall are made in its plastic state, so that the material can be obtained and the study is done on the basis for an automatic stabilization of the slope, this modeling was done using PLAXIS 2D software.

4.1. Verification

The two-dimensional model used in this paper is the same as that used by (Tschuchnig et al., 2015). However, reinforcement with anchor was added, including slope geometry, soil characteristics element type and failure criteria (15 trigonometric node elements), as shown in Fig. 5. The network roughness, a difference in expansion angle, and failure mechanism were discussed in this paper.

SRM calculated *FoS* based on Tschuchnig et al. (2015) using five expansion angles (0°, 5°, 10°, 15°, 35° and 45°).

Moreover, ψ'=35' the compared with the prestressed frame anchor and sheet pile wall. The results in Fig. 2 show that the chances gained are 3.145 when ψ'=0°. The results (*FoS*=1.30-1.37) showed a greater trend than (Tschuchnig et al., 2015). When ψ'=45, the *FoS* affinity was irregular and low. This abnormal phenomenon is the result of destroying the uniqueness of the mechanism. The *FoS* obtained by ψ'=45˚ score 2.565 is far from

the result of Tschuchnig et al. (2015) (*FoS*=1.53). Fig. 6 shows the reason why *FoS* is greater than 45° at 35°. Possible causes of the numerical tolerances determine the content of the problem. In this research, the slope was reinforced with a framed prestressed anchor bar and sheet pile wall to reduce slips. To assess this problem, the expansion angle was studied to assess the *FoS*. If the *FoS* for ψ'=45° score between 2.565 it decreased as tolerance decreased. When tolerance decreased gradually, *FoS* increased for ψ'=35° degrees from 2.971 incidence of *FoS* at ψ'=45° was slightly lower than that at ψ'=35°.

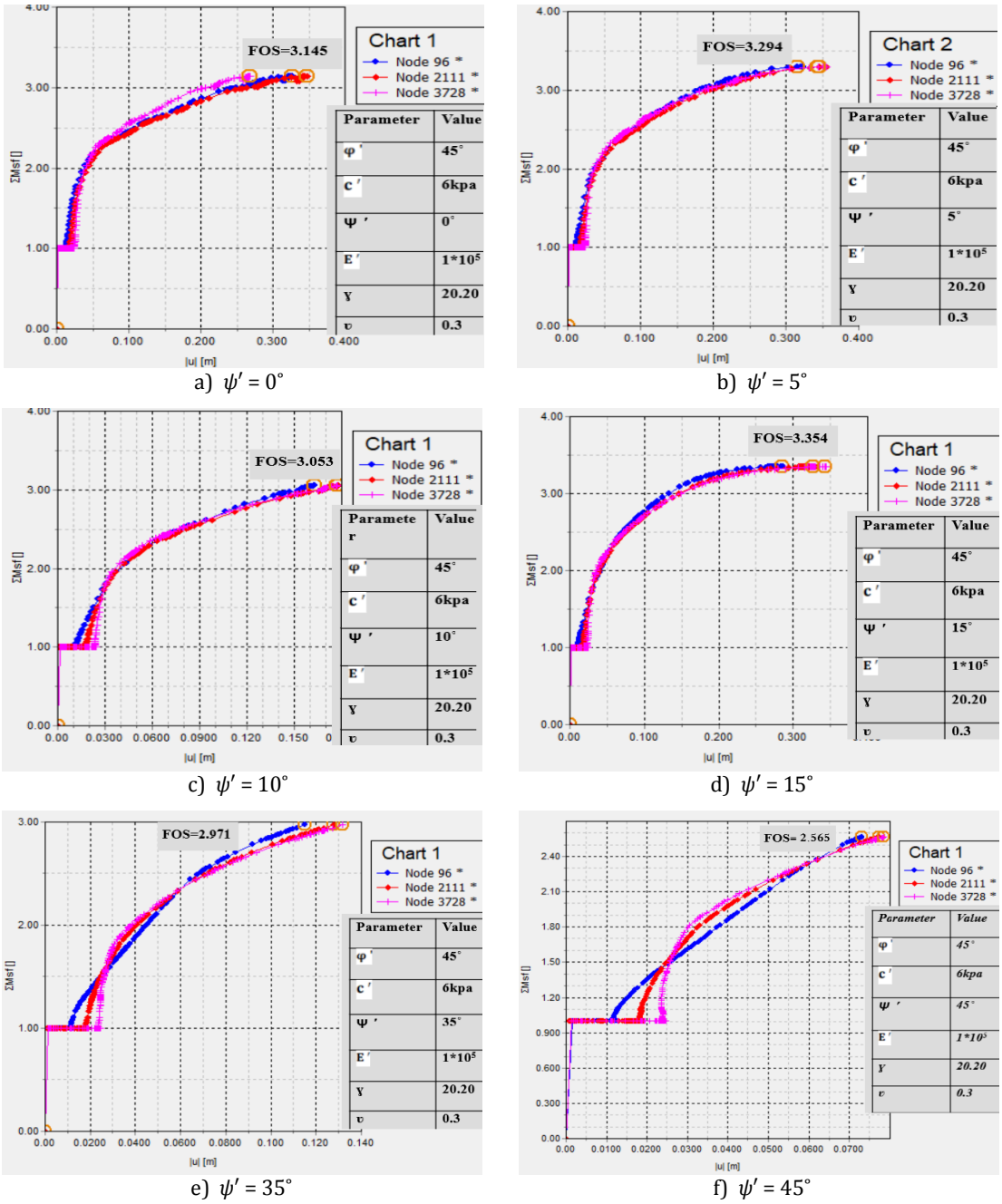

Fig. 6. Comparison of the *FoS* for framed prestressed anchor bar and sheet pile wall with different expansion angles.

Summarizing the above comparison from the two-dimensional model, Tschuchnigg and others believe that the model's trend is safe and stable. (Tschuchnig et al., 2015). When the expansion angle results, mesh roughness, and failure mechanism when compared, numerical values are different. Based on the two-dimensional model of (Tschuchnig et al., 2015) using PLAXIS 2D software, the slope model supported by frame prestressed anchor and sheet pile wall established, and the influence of expansion angle on slope stability is studied.

4.2. Deformation responses and effective stress

Deformation responses horizontal and vertical deformation responses were recorded at different locations of a framed prestressed anchor bar and sheet pile

wall. The values of horizontal distortion (0.08204) were found to be greater than the vertical distortion (0.03162) for all the cases considered. Hence, only vertical distortion differences are shown here. Fig. 7 displays the difference in vertical deformations of the framed prestressed anchor bar and sheet pile wall.

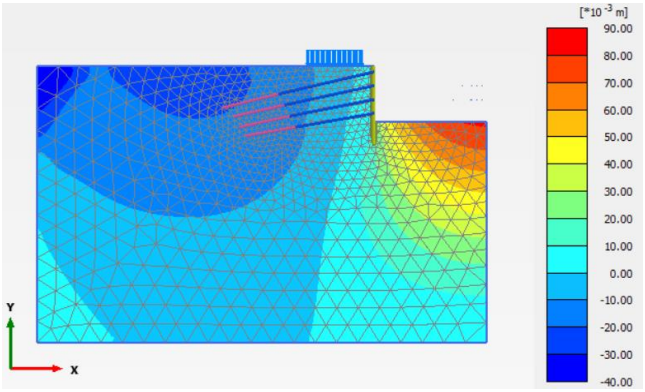

Fig. 7. Variation of vertical deformation of framed prestressed anchor bar and sheet pile wall.

Effective stress responses of effective stresses are recorded at a different location of framed prestressed anchor bar and sheet pile wall. The effective horizontal stress values are found to be more than that of effective vertical stress for all the considered cases. Typical variation of effective horizontal and vertical stresses of framed prestressed anchor bar and sheet pile wall presented in Figs. 8-10.

4.3. Discussion

4.3.1. Influence of expansion angle

The effects of expansion angles (ψ' = 0°, 5°, 10°, 15°, 35°, 45°) on the *FoS* affinity in the model were studied of a pre-framed anchor bar and two-dimensional laminate pile wall. The results showed that *FoS*=2.565 when ψ'=45° degrees, it shows higher instability than the two-dimensional model. The results show that *FoS* oscillations contract significantly (*FoS*=2.565) at 10°≤ ψ'≤ 35°, and the convergence is enhanced (almost no oscillation sign). For these cases, no significant difference in the destruction mechanism was more observed. When $\psi'=\varphi$, the *FoS* convergence and failure mechanism in the two-dimensional model are more evident than that in $\psi'\neq\varphi$ model. In the model, the results obtained in this study are different from those obtained by Tschuchnig et al. (2015). One they mean that the relevant flow-based (Davis, 1968) is not suitable for solving the slope stability problems in the pre-frame anchor bolt and two-dimensional laminate pile wall model. In the range of ψ'=35°-45°, the separation line events were observed in different affinity results of *FoS*. Therefore, the peak valley of ψ'=35° were analyzed to test the failure mechanism. When ψ'=35°, the failure surface is clear and developed; when ψ'= 45°, the failure surface is incomplete.

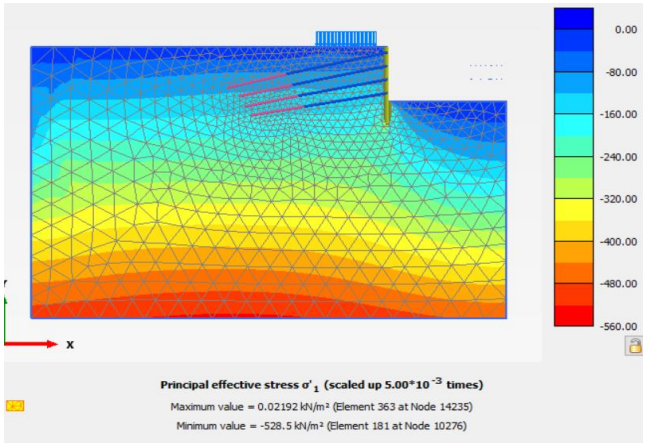

Fig. 8. Variation of effective stress of framed prestressed anchor bar and sheet pile wall (σ_1).

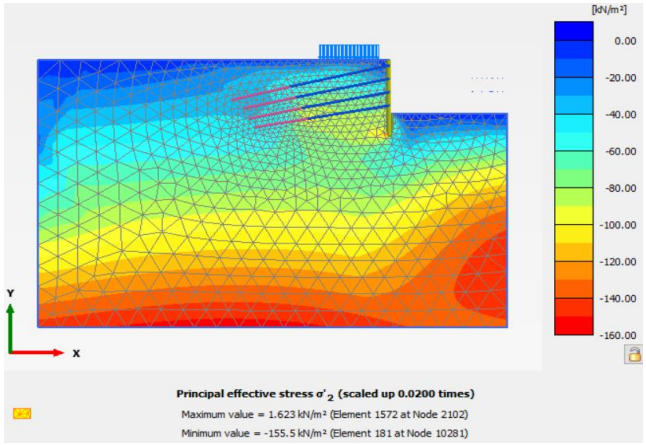

Fig. 9. Variation of effective stress of framed prestressed anchor bar and sheet pile wall (σ_2).

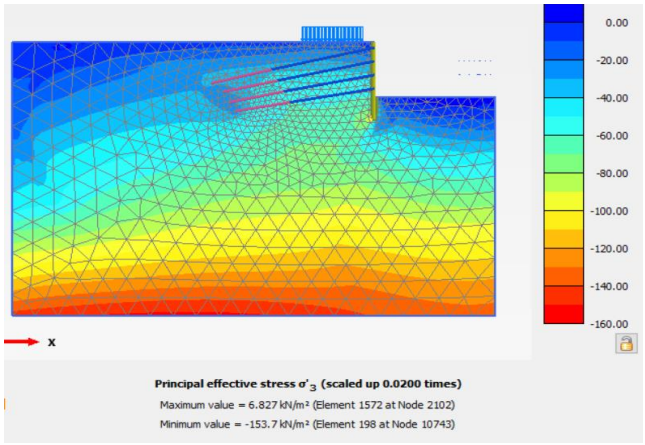

Fig. 10. Variation of effective stress of framed prestressed anchor bar and sheet pile wall (σ_3).

4.3.2. Effects of both pre-framed anchor tape and laminate pile wall and soil strength coefficients

The effect of the expansion angle on *FoS* affinity under different soil parameters was studied. For the friction

angle, since the numerical model must follow the balance rule (slope will not be a destroyed in its initial equilibrium state), a tilt angle (β=0°) is selected for inspection, and three different expansion angles (ψ'=0° and 15°) Degrees and ψ'=ψ. When the three-dimensional model was preparedness at β=0°, ψ'=0°, 15° and 45° are using to analyze various coherent quantities. When ψ'=0° or 15°, *FoS* affinity was relatively stable. According to the bound flow rule, the affinity at lower concentration is better than that at higher concentration-failure descent mechanism. Fig. 6 shows the effect of soil cohesion on *FoS* affinity; various c' convergence curves fluctuate slightly at low expansion angle (ψ'=0°). When ψ'=35°, most of the convergence curves are smooth except *c*'=20.02 kPa. For a high expansion angle (ψ'=45°), obvious oscillation with different *c* were observed. The trend observed in Fig. 6(d) and Fig. 6(e) is consistent, where converges smoothly when ψ'=15°-35°.

5. Conclusions

In this study, the influence of ψ' on *FoS* were analyzed by using frame prestressed anchor and sheet pile wall, and the PLAXIS 2D program was used to study the influence of ψ' on-grid roughness, inclination angle (β=0), and soil strength parameters (*c*' and ψ') through two-dimensional analysis of frame prestressed anchor and sheet pile wall. According to the results of this study, we can draw the following conclusions and suggestions.

- The results show that ψ' has a significant effect on *FoS* affinity, but this affinity may be unstable. However, the effects may vary depending on the inclination angle or soil strength parameters (*c*' and ψ').
- The expansion angle's influence on the slope model's convergence was supported by pre-frame anchor belts and laminated pile walls. On the other hand, various sliding surfaces. However, the two-dimensional model supported by pre-frame anchor tapes and laminated pile walls showed the opposite result-unstable at ϕ'=ψ'. Therefore, engineers must consider the influence of ψ' on *FoS* affinity.
- Declining soil strength parameters (*c*' and ϕ) compared with higher soil strength parameters, when ϕ'=ψ, the affinity of fiction *FoS* is relatively insensitive. Besides, when ψ'=ϕ'=45°, the tilt angle has little effect on the *FoS* affinity. However, when ψ'≠ϕ Depending on the value of ψ', the influence of the tilt angle ψ is different.

References

Baker R, Shukha R, Operstein V, Frydman S (2006). Stability charts for pseudo-static slope stability analysis. *Soil Dynamics and Earthquake Engineering*, 26(9), 813–823.

Bishop AW (1955). The use of slip circles in the stability analysis of earth slopes. *Geotechnique,* 5(1), 7–17.

Cai F, Ugai K, Hagiwara T (2002). Base stability of circular excavation in soft clay. *Journal of Geotechnical and Geoenvironmental Engineering,* 128(8), 702–706.

Cheng YM, Lansivaara T, Wei WB (2007). Two-dimensional slope stability analysis by limit equilibrium and strength reduction methods. Computers and Geotechnics, 34, 137–50.

Dafalias YF (1986). Bounding surface plasticity. I: Mathematical foundation and hypo- plasticity. *Journal of Engineering Mechanics*, 112 (9), 966–987.

Davis EH (1968). Theories of plasticity and failure of soil masses. In: *Lee IK, editor. Soil Mechanics: Selected Topics*. New York, NY, USA: Elsevier, 341–354.

Dawson EM, Roth WH, Drescher A (1999). Slope stability analysis by strength reduction. *Geotechnique*, 49(6), 835–840.

Griffiths DV (1999). Slope stability analysis by finite elements. *Geotechnique,* 49(3), 387-403.

Griffiths DV, Lane PA (2001). Slope stability analysis by finite elements. *Géotechnique,* 51(7), 653–654.

Griffiths DV, Marquez RM (2007). Three-dimensional slope stability analysis by elastic-plastic finite elements. *Geotechnique*, 57(6), 537–546.

Hang L, Ping C (2012). Influence of material dilation angle on stability of homogeneous with surcharge load. *International Journal of Geotechnical Engineering,* 17C, 329–340.

Ho IH (2014). Parametric studies of slope stability analyses using three-dimensional finite element technique: geometric effects. *Journal of GeoEngineering*, 9(1), 33–43.

Hwang J, Dewoolkar M, Ko HY (2002). Stability analysis of two-dimensional excavated slopes considering strength anisotropy. *Canadian Geotechnical Journal*, 39(5), 1026–1038.

Jerman J, Mašín D (2020). Hypoplastic and viscohypoplastic models for soft clays with strength anisotropy. *International Journal for Numerical and Analytical Methods in Geomechanics*, 44(10), 1396–1416.

Kolymbas D (2012). Barodesy: a new hypo plastic approach. *International Journal for Numerical and Analytical Methods in Geomechanics,* 36(9), 1220–1240.

Kumar J (2000). Slope stability calculations using limit analysis. In: *Proc. Slope Stability, ASCE Special Publication*, 101, 239–249.

Kumar J (2004). Stability factors for slopes with nonassociated flow rule using energy consideration. *International Journal of Geomechanics*, 264(4), 264–272.

Li AJ, Merifield RS, Lyamin AV (2010). Three-dimensional stability charts for slopes based on limit analysis methods. *Canadian Geotechnical Journal,* 47(12), 1316–1334.

Likitlersuang S, Pholkainuwatra P, Chompoorat T, Keawsawasvong S (2018). Numerical modelling of rail way embankment for high-speed train constructed on soft soil. *Journal of GeoEngineering*, 13(3), 149–159.

Lim K, Li AJ, Lyamin AV (2015). Three-dimensional slope stability assessment of two-layered untrained clay. *Computers and Geotechnics*, 70, 78–89.

Lim K, Lyamin AV, Cassidy MJ, Li AJ (2015). Three-dimensional slope stability charts for frictional fill materials placed on purely cohesive clay. *International Journal of Geomechanics*, 16(2), 04015042.

Lim K, Li AJ, Schmidt A, Lyamin AV (2017). Slope-stability assessments using finite-element limit-analysis methods. *International Journal of Geomechanics*, 17(2), 06016017.

Liu SY, Shao LT, Li HJ (2015). Slope stability analysis using the limit equilibrium method and two finite element methods. *Computers and Geotech*nics, 63, 291–298.

Lyamin A, Sloan S (2002b). Lower bound limit analysis using non-linear programming. *International Journal for Numerical Methods in Engineering*, 55(5), 573–611.

Lyamin AV, Sloan S (2002a). Upper bound limit analysis using linear finite elements and non-linear programming. *International Journal for Numerical and Analytical Methods in Geomechanics*, 26(2), 181–216.

Manzari MT, Nour MA (2000). Significance of soil dilatancy in slope stability analysis. *Journal of Geotechnical and Geoenvironmental Engineering*, 126(1), 75–80.

Matsui T, San KC (1992). Finite element slope stability analysis by shear strength reduction technique. *Soils Found*, 32(1), 59–70

Michalowski RL (2002). Stability charts for uniform slopes. *Journal of Geotechnical and Geoenvironmental Engineering*, 128(4), 351–355.

Morgenstern Nu, Price VE (1965). The analysis of the stability of general slip surfaces, *Geotechnique*, 15(1), 79–93.

Niemunis A, Herle I (1997). Hypoplastic model for cohesionless soils with elastic strain range. *Mechanics of Cohesive-frictional Materials: An International Journal on Experiments, Modelling and Computation of Materials and Structures*, 2(4), 279–299.

Roscoe KH (1970). The influence of strains in soil mechanics. *Geotechnique*, 20(2), 129–170.

Sulsky D, Zhou SJ, Schreyer HL (1995). Application of a particle-in-cell method to solid mechanics. *Computer Physics Communications*, 87(1–2), 236–252.

Tschuchnigg F, Schweiger HF, Sloan SW (2015). Slope stability analysis by means of finite element limit analysis and finite element strength reduction techniques. Part I: Numerical studies considering non-associated plasticity. *Computers and Geotechnics*, 70, 169–177.

Wu W, Kolymbas D (1990). Numerical testing of the stability criterion for hypo plastic constitutive equations. *Mechanics of Materials*, 9(3), 245–253.

Yu Y, Xie L, and Zhang B (2005). Stability of earth-rock fill dams: Influence of geometry on the three-dimensional effect. *Computers and Geotechnics*, 32(5), 326–339.

Zabala F, Alonso E (2011). Progressive failure of aznalcóllar dam using the material point method. *Géotechnique,* 61(9), 795–808.

Zienkiewicz OC, Humpheson C, Lewis RW (1975). Associated and non-associated visco-plasticity and plasticity in soil mechanics. *Geotechnique*, 25(4), 671–689.